UNIVERSITY OF CALIFORNIA SAN DIEGO

Fluorine-19 Magnetic Resonance Imaging platform to quantify T cell therapy biodistribution, persistence and efficacy

A dissertation submitted in partial satisfaction of the
requirements for the degree of
Doctor of Philosophy

in

Bioengineering

by

Fanny Chapelin

Committee in charge:

Professor Pedro Cabrales, Chair
Professor Eric T. Ahrens, Co-Chair
Professor David Dubowitz
Professor Stephen Schoenberger
Professor Yingxiao Wang

2019

The Dissertation of Fanny Chapelin is approved, and it is acceptable in quality and form for publication on microfilm and electronically:

Co-Chair

Chair

University of California San Diego

2019

EPIGRAPH

But blessed is the one who trusts in the Lord,
whose confidence is in him.
They will be like a tree planted by the water
that sends out its roots by the stream.
It does not fear when heat comes;
its leaves are always green.
It has no worries in a year of drought
and never fails to bear fruit.
Jeremiah 17:7-8

TABLE OF CONTENTS

LIST OF ABBREVIATIONS

ACT	Adoptive Cell Transfer/Therapy
ANOVA	Analysis of Variance
BLI	Bioluminescence Imaging
CAR	Chimeric Antigen Receptor
CFSE	5(6)-Carboxyluorescein N-hydroxySuccinimidyl Ester
CPP	Cell penetrating peptide
CO_2	Carbon Dioxide
D_2O	Deuterated water
DC	Dendritic cell
DLS	Dynamic Light Scattering
DMEM	Dulbecco's Modified Eagle Medium
EGFRvIII	Epidermal Growth Factor Receptor variant three
EYP	Egg Yolk Phospholipid
F68	Polyethylene-Polypropylene
FBS	Foetal Bovine Serum
FACS	Fluorescence-Activated Cell Sorting
FDA	Food and Drug Administration
FID	Free Induction Decay
FITC	Fluorescein Isothiocyanate
FOV	Field Of View
IACUC	Institutional Animal Care and Use Committee
IND	Investigational new drug
IL-2	Recombinant human Interleukin 2
IV	Intra-Venously
IT	Intra-Tumorally
LOD	Limit of Detection
MACS	Magnetic-Activated Cell Sorting
MHC	Major Histocompatibility Complex
MRI	Magnetic Resonance Imaging
NK	Natural Killer
NMR	Nuclear Magnetic Resonance
NOD/SCID	Non-Obese Diabetic/Severe Combined ImmunoDeficiency
OptiMEM	Optimized Minimal Essential Medium
PBMC	Peripheral Blood Mononuclear Cells
PBS	Phosphate Buffered Saline
PCE	Perfluoro-15-crown-5-ether
PdI	Polydispersity Index
PET	Positron Emission Tomography
PFC	Perfluorocarbon
PFPE	Perfluoropolyether
pO_2	Partial pressure of oxygen
PRESS	Point-RESolved Spectroscopy
PSI	Pounds per square inch
RARE	Rapid Acquisition with Relaxation Enhancement

RES	Reticulo-Endothelial System
ROI	Region Of Interest
RPMI	Roswell Park Memorial Institute medium
SC	Subcutaneously
scFv	single chain variable Fragment
SCID	Severe Combined Immunodeficiency
SNR	Signal to Noise Ratio
TAT	Trans-Activator of Transcription
TATA	Perfluoroheptyl TAT
TATP	PerfluoroPEG TAT
TCR	(engineered) T Cell Receptor
TE	Echo Time
TFA	Trifluoroacetic Acid/Sodium trifluoroacetate
TIL	Tumor Infiltrating Lymphocyte
TLC	Thin Layer Chromatography
TR	Repetition Time

LIST OF FIGURES

LIST OF TABLES

ACKOWLEDGEMENTS

The success of this thesis work emanated from an essential collaborative effort and would not have been possible without the support and discussions with individuals across disciplines and institutions. First and foremost, I would like to thank my advisor, Dr. Eric Ahrens, for his guidance and support over the years and the opportunities to present my work and learn from experts in their field.

I'd like to thank all the members, past and present, of the Ahrens lab for their help and friendship over the past four years. Special thanks to Emma, for your enthusiasm and positivity and for teaching me so much about emulsion making. Das, thank you for your career advice and tips in NMR. Shang, thank you for your patient instruction in plasmid and virus making. Wenlian, for teaching me most of the hands-on MR I know, and Deanne for being so flexible and always helping me on the animal experiments with a smile. Vivie, thank you for your friendship and outstanding help with admin/grant issues.

I'd also want to thank all members of my thesis committee, for their helpful feedback throughout my thesis. In particular, thank you Dr. Peter Wang, for the privilege of teaching with and for you, and for all your support and career advice, and for always having a positive and encouraging word when I needed it. Dr. Schoenberger, thank you for giving me the opportunity to learn more about immunology and flow cytometry. To Jan Lenington, thank you for steadfast admin support through my visas and other paperwork.

To our collaborator, Dr. Okada for providing the CAR construct used in all these experiments. To Jesus and Codi at the flow cytometry core, for their positive attitude and

always helping hand. To the staff at Invicro for keeping me company in the imaging facility and helping me figure some things out.

To my friends in the building and in the department, for reminding me there is a life outside the lab. Especially Alexandra, thank you for teaching me some mouse handling tips and histo protocols, but most importantly for your friendship through the hard times of this thesis, wedding planning, and marathon training in Torrey pines. Nikki, thanks for moral support and company during the late evenings in the lab.

To all my friends (Viola, Shari, Heidi, etc.) and family (Khuranas) near and far, thank you for all your love, prayers and positive reinforcement. Papa, Maman, thanks for always believing in me and supporting my ambitions, even if it meant going across the world away from you. Audrey, for being the sister I never had and loving and supporting me just the same. To my husband, Aman Khurana, thank you for being my biggest supporter and a shoulder I can always come and cry on or complain. But most importantly, thank you for being the best partner in life and in lab!

Chapter 1, in part, contains text as it appears in two manuscripts: Springer book chapter entitled "Magnetic resonance imaging of immune cell trafficking in response to chemical agents in experimental autoimmune encephalomyelitis", Chapelin F, Ahrens E.T from "Visualizing chemical communication among migratory cells *in vivo*" (2019), and review paper entitled "Fluorine-19 MRI for detection and quantification of immune cell therapy for cancer" Chapelin F, Capitini C, Ahrens E.T, JITC (2018) with revisions and

formatting changes for this dissertation. Besides this, the content of Chapter 1 is original. The dissertation author was the primary author of this book chapter and review paper.

Chapter 2, in part, contains text as it appears in two manuscripts. Springer book chapter entitled "Magnetic resonance imaging of immune cell trafficking in response to chemical agents in experimental autoimmune encephalomyelitis", Chapelin F, Ahrens E.T from "Visualizing chemical communication among migratory cells *in vivo*" (2019), and review paper entitled "Fluorine-19 MRI for detection and quantification of immune cell therapy for cancer" Chapelin F, Capitini C, Ahrens E.T. Chapter 2 also contains figures from supplemental material of published material in the journal Scientific Reports 2017, with revisions and formatting changes for this dissertation. The authors and title of the manuscript are as follows: Chapelin F, Gao S, Okada H, Weber T, Messer K, Ahrens E.T. Fluorine-19 nuclear magnetic resonance of chimeric antigen receptor T cell biodistribution in murine cancer model. Scientific Reports, (2017). Besides this, the content of Chapter 2 is original. The dissertation author was the primary author of these papers.

Chapter 3, in full, is a reprint of the material as it appears in the journal Scientific Reports 2017, with minor revisions and formatting changes for this dissertation. The authors and title of the manuscript are as follows: Chapelin F, Gao S, Okada H, Weber T, Messer K, Ahrens E.T. Fluorine-19 nuclear magnetic resonance of chimeric antigen receptor T cell biodistribution in murine cancer model. Scientific Reports, (2017). The authors acknowledge technical support from Ms Hongyan Xu. The dissertation author was the primary investigator and author of this paper.

Chapter 4, in full, contains text submitted for publication of the material. Hingorani D*, Chapelin F*, Stares E, Adams E, Okada H, Ahrens E.T. Cell Penetrating Peptide

Functionalized Perfluorocarbon Nanoemulsions for Targeted Cell labeling and Enhanced Fluorine-19 MRI Detection *Authors contributed equally. The authors acknowledge technical support from Ms Hongyan Xu. The dissertation author was the primary investigator and author of this paper.

Chapter 5, in full is currently being prepared for submission for publication of the material. Chapelin F, Zhu W, Chen R, Lister D, Stares E, Messer K, Okada H, Ahrens E.T. Magnetic resonance imaging monitoring of *in vivo* intracellular oximetry response to chimeric antigen receptor T cell immunotherapy against glioma. The dissertation author was the primary investigator and author of this paper.

Chapter 6, in part contains text as it appears in the Journal for ImmunoTherapy of Cancer 2018. “Fluorine-19 MRI for detection and quantification of immune cell therapy for cancer” Chapelin F, Capitini C, Ahrens E.T. The dissertation author was the primary investigator and author of this paper.

VITA

2009	Bachelor of Science in Biology, University of Paris V, France
2012	Master of Science in Biomedical Engineering, Biomaterials, University of Technology of Compiegne, France
2012-2014	Research Assistant, Stanford University
2015-2017	Teaching Assistant, Department of Bioengineering, University of California San Diego
2019	Doctor of Philosophy in Bioengineering, University of California San Diego

PUBLICATIONS

1. Hingorani D*, **Chapelin F***, Stares E, Adams E, Okada H, Ahrens E.T. Cell penetrating peptide functionalized perfluorocarbon nanoemulsions for targeted cell labeling and enhanced fluorine-19 MRI detection. Under review at MRM.

2. **Chapelin F**, Zhu W, Chen R, Lister D, Stares E, Messer K, Okada H, Ahrens E.T. Magnetic resonance imaging monitoring of *in vivo* intracellular oximetry response to chimeric antigen receptor T cell immunotherapy against glioma. In preparation.

3. **Chapelin F**, Capitini C, Ahrens E.T. Fluorine-19 MRI for detection and quantification of immune cell therapy for cancer. **JITC,** (2018).

4. **Chapelin F**, Khurana A, Moneeb M, Hazard F, Chan C, Nejadnik H, Gratzinger D, Messing S, Erdmann J, Gaur A, Daldrup-Link H.E. Tumor Formation of adult stem cell transplants in rodent arthritic joints. **MIBI**, (2018).

5. **Chapelin F,** Gao S, Okada H, Weber T, Messer K, Ahrens E.T. Fluorine-19 nuclear magnetic resonance of chimeric antigen receptor T cell biodistribution in murine cancer model. **Scientific Reports**, (2017).

6. Khurana A, **Chapelin F**, Xu H, Acevedo JR, Molinolo A, Nguyen Q, Ahrens E.T. Visualization of macrophage recruitment in head and neck carcinoma model using fluorine-19 magnetic resonance imaging. **MRM**, (2017).

7. **Chapelin F**, Ahrens E.T. Magnetic Resonance Imaging of immune cell trafficking in response to chemical agents in experimental autoimmune encephalomyelitis. Prescher, J, Contag, C.H's Visualizing chemical communication among migratory cells *in vivo*. **Springer Press**, (2019).

8. Daldrup-link H.E, Chan C, Lenkov O, Taghavigarmestani S, Nazekati T, Nejadnik H, **Chapelin F**, Khurana A, Tong X, Yang F, Pisani L, Longaker M, Gambhir S.S. Detection of Stem Cell Transplant Rejection with Ferumoxytol MR Imaging: Correlation of MR Imaging findings with Those at Intravital Microscopy. **Radiology**, (2017).

9. Nejadnik H, Diecke S, Lenkov O.D, **Chapelin F**, Donig J, Tong X, Derugin N, Chan R.C, Gaur A, Yang F, Wu J.C, Daldrup-Link H.E. Improved Approach for Chondrogenic Differentiation of Human Induced Pluripotent Stem Cells. **Stem Cell Rev**, (2015).

10. Khurana A, **Chapelin F**, Daldrup-link H.E. Mesenchymal Hamartoma and embryonal sarcoma of the liver. In: H Daldrup-Link, B Newman's Pearls and Pitfalls in Pediatric Radiology. Cambridge: **Cambridge University Press**. (2014).

11. **Chapelin F**, Beck G, Lenkov O.D, Daldrup-Link H.E. Laboratory Protocols, a Collection of Cell Tracking Protocols for Imaging and Stem Cell Researchers. Ebook on the **iBooks store**, Nov. 2013 (700 downloads as of 1/1/2018).

12. Khurana A, **Chapelin F**, Beck G, Lenkov O.D, Donig J, Nejadnik H, Messing S, Derugin N, Chan R.C, Gaur A, Sennino B, McDonald D.M, Kempen PJ, Tikhomirov G.A, Rao J, Daldrup-Link H.E. Iron Administration before Stem Cell Harvest Enables MR Imaging Tracking after Transplantation. **Radiology**, (2013).

13. Khurana A*, Nejadnik H*, **Chapelin F**, Lenkov OD, Gawande R, Lee S, Gupta SN, Aflakian N, Derugin N, Messing S, Lin G, Lue TF, Pisani L, Daldrup-Link HE. Ferumoxytol: A new, clinically applicable label for stem cell tracking in arthritic joints with MRI. **Nanomedicine**, (2013).

SELECTED POSTERS AND PRESENTATIONS

1. **Chapelin F**. Tracking immunotherapeutic T cells using MRI. ISMRM member-initiated symposium (Paris, France), 2018, Invited speaker.

2. **Chapelin F,** Zhu W, Okada H, Ahrens E. *In vivo* monitoring of intracellular pO_2 in response to CAR T cell immunotherapy against glioma. ISMRM conference (Paris, France), 2018, oral presentation.

3. **Chapelin F.** ^{19}F Magnetic Resonance Imaging platform to quantify T cell therapy biodistribution, persistence and efficacy, Sanford Consortium Seminar Series, UCSD (San Diego, USA), 2018, oral presentation.

4. **Chapelin F,** Zhu W, Okada H, Ahrens E. *In vivo* monitoring of intracellular pO_2 in response to CAR T cell immunotherapy against glioma. Bioengineering Day, UC San Diego, USA, 2018, poster.

5. **Chapelin F**, Zhu W, Okada H, Ahrens E. *In vivo* monitoring of intracellular pO_2 in response to CAR T cell immunotherapy against glioma, AACR Workshop on Immunobiology of primary and metastatic CNS cancer (San Diego, USA), 2018, poster.

6. **Chapelin F,** Gao S, Okada H, Ahrens E. Fluorine-19 nuclear magnetic resonance (NMR) cytometry to track human CAR T-cell biodistribution in murine studies of glioblastoma immunotherapy. Mechanisms and Models of Cancer Symposium, Salk Institute (San Diego, USA), 2017, poster.

7. **Chapelin F**, Okada H, Ahrens E. Fluorine-19 NMR cytometry to quantify human transgenic CAR T-cell biodistribution in murine studies of glioblastoma immunotherapy. ISMRM Conference (Hawaii, USA), 2017, oral presentation.

8. **Chapelin F**, Okada H, Ahrens E. Fluorine-19 nuclear magnetic resonance (NMR) cytometry to track human CAR T-cell biodistribution in murine studies of glioblastoma immunotherapy. SITC Conference (National Harbor, USA), 2016, poster.

9. **Chapelin F**, Okada H, Ahrens E. Fluorine-19 nuclear magnetic resonance (NMR) to track human transgenic T-cell biodistribution in murine studies of glioblastoma immunotherapy. Sanford Consortium Seminar Series, October, UCSD (San Diego, USA), 2016, oral presentation.

10. **Chapelin F**, Weber T, Xu H, Ahrens E. *In vivo* monitoring of intracellular pO_2 changes and cell apoptosis during CAR T-cell therapy against cancer. ISMRM Workshop (San Diego, USA) 2015, poster.

11. **Chapelin F**, Weber T, Xu H, Ahrens E. *In vivo* monitoring of intracellular pO2 changes and cell apoptosis during CAR T-cell therapy against cancer. Stem Cell Meeting on the Mesa (San Diego, USA) 2015, poster.

ABSTRACT OF THE DISSERTATION

Fluorine-19 Magnetic Resonance Imaging platform to quantify T cell therapy biodistribution, persistence and efficacy

by

Fanny Chapelin

Doctor of Philosophy in Bioengineering

University of California San Diego, 2019

Professor Pedro Cabrales, Chair

Professor Eric T. Ahrens, Co-Chair

Cancer is responsible for over 8 million deaths annually and the number of new cases is expected to increase by approximately 70% over the next 20 years. Surgery, chemotherapy and radiotherapy have been used for decades as primary strategies against cancer in patients;

however, cancer cell drug and radiation resistance development often leads to lower remission and higher relapse incidence. Cell therapies for cancer are emerging approaches to enhance tumor-specific killing and include expansion of patients' tumor-infiltrating lymphocytes or complex engineering of the T cell receptor or Chimeric Antigen Receptors (CAR). The latter have shown unprecedented progress towards treating incurable cancers and are currently being examined in over 200 clinical trials. Developing successful therapeutic strategies using live cells entails the ability to determine their *in vivo* biodistribution and persistence after systemic administration. Non-invasive imaging techniques such as Magnetic Resonance Imaging (MRI) and Positron Emission Tomography are the best candidates for real time, quantitative assessment of tumor response. Perfluorocarbon (PFC) probes are composed of numerous fluorine atoms, which are not naturally present in the body and allow for background free quantitation by MRI. This thesis describes fluorinated imaging probes and methods for labeled cell tracking by ^{19}F MR imaging and spectroscopy. Firstly, we show that, following transfer to the subject, ^{19}F nuclear magnetic resonance allows quantification of local and systemic accumulation PFC-labeled CAR T cells in a murine cancer model. As a second step, we report strategies to increase cell loading through cell penetrating peptides, enabling unbiased detection of lymphocytes *in vivo*. Finally, we exploit the property of PFC nanoemulsions to dissolve paramagnetic oxygen to measure tumor intracellular oxygenation changes in response to therapy. Overall, ^{19}F MR imaging is a versatile technique that can provide insights into the survival and modes of actions of cell therapy against cancer.

Chapter 1: Introduction

Considerable effort is being invested on the design of novel cellular based therapeutic strategies to treat individuals with genetic disorders, neurological disorders, and chronic conditions such as cancer and autoimmunity. Cancer immunotherapy is a relatively young field of research directing specific immune entities against cancer cells. Among those, adoptive T cell transfer has the potential to provide personalized less toxic and more efficacious treatment through the repair or activation of endogenous functions. Developing smarter, potent therapies could be accelerated by the ability to rapidly determine biodistribution and persistence *in vivo*. Cell labeling probes using perfluorocarbon nanoemulsions, paired with fluorine-19 (^{19}F) MRI detection, enables quantification of cell localization and survival. This thesis focuses on developing ^{19}F magnetic resonance imaging platforms to quantify T cell therapy biodistribution, persistence and efficacy in murine cancer model.

1.1. The immune landscape of human tumors

1.1.1. Mechanisms of immune escape in cancer

The central dogma of immunology has long been that when functioning correctly, the immune system is a powerful force actively preventing disease and neoplastic development through immunosurveillance[1, 2]. Immune cells such as T cells, natural killer (NK) cells, and dendritic cells (DCs) are critically involved in the elimination of foreign pathogens, recognition and removal of transformed cells, and repair of damaged tissue. The

innate immune system, including monocytes, macrophages, DCs and NK cells, provide front line protection through cancer cell recognition, lysis, and pro-inflammatory cytokine production[3]. T and B cells are the main effectors of the adaptive immune system and mediate antigen-specific responses and long term memory[4].

In the early 2000s, it was established that the immune system has a dual role in cancer. Not only is it involved in preventing tumor progression, it is also promoting its outgrowth[5, 6]. This refined hypothesis, coined as cancer immunoediting, describes the dynamic process in three phases: elimination, equilibrium, and escape. The elimination phase corresponds to the antitumor response by the immune system when detecting tissue damage engendered by neoplastic outgrowth. If the immunosurveillance effectors fail to eradicate all transformed cells, the surviving tumors cells enter the phase of equilibrium with the immune system[7]. The immune system continues to target highly immunogenic transformed cells while increasing the selection pressure placed on the remaining tumor cells. The latter accumulate mutations eventually leading to antigen loss or non-presentation and are therefore no longer recognized by immune cells[7]. A trait shared by 40-90% of human cancers is MHC downregulation, which plays a major role in future tumor escape[8]. Cytokine secretion by the tumor cells creates an immunopriviledged microenvironment[8], increasing resistance to immune cell attacks. The escape phase corresponds to the stage when tumor outgrowth is no longer hampered by the immune system. Tumor cells begin to recruit anti-inflammatory immune cells (tumor associated macrophages, regulatory T cells) that inhibit anti-tumor responses[9]. While the equilibrium phase can last several years, the escape phase usually correlates with rapid development of clinical symptoms. Mechanisms of tumor

editing continue to be heavily investigated as well as numerous strategies to regulate or counteract these effects.

1.1.2. Glioblastoma multiforme

Glioma is a type of tumor originating from the glial cells in the brain. The World Health Organization (WHO) categorizes glioma as grades I-IV based on histopathology findings. This classification indicates tumor aggressiveness, prognosis and survival. Glioblastoma multiforme (GBM) is a grade VI glioma, meaning the most aggressive and most common (~54%) brain cancer[10]. According to the Central Brain Tumor Registry of the United States (CBTRUS), GBM incidence rate is about 3 per 100,000 people[10]. GBMs can occur spontaneously and referred to as 'primary' GBM or transform from lower grade gliomas and therefore termed 'secondary' GBMs. The mean GBM incidence age is 62-65 years but still represents up to 8% of pediatric brain tumors[10-12]. Indicative symptoms include headaches, seizures and neurologic deficits. Diagnosis is then confirmed by abnormal findings on magnetic resonance images. In histopathology, GBM presents with irregular cell and nuclear shapes (atypia), high microvascular density and necrotic cores[13]. The median survival time is less than three months without treatment and 12-14 months with surgical resection and radiation therapy and/or chemotherapy[14].

1.1.3. Pillars of cancer therapy

Standard of care for primary GBMs involves surgical resection followed by radiotherapy and chemotherapy. This strategy has been used for decades against cancer in patients[15] Surgery is a necessary, albeit not sufficient, procedure due to ill-defined tumor

border. Aggressive radiotherapy prolongs survival but some tumor cells develop resistance, preventing full recovery. Chemotherapy, including temozolomide (TMZ) and O^6-methylguanine DNA methyltransferase (MGMT) treatment also showed increased median survival (14 and 22 months respectively)[16, 17]. Numerous chemotherapy candidates now target tumor metabolism, survival, proliferation, apoptosis and angiogenesis.

Despite combination of these therapies, prognosis of GBM remains dismal, in part due to its highly proliferative and heterogeneous nature and ability to evade the immune system. Overall, non-specific cell toxicities and side effects from chemotherapy and radiation, as well as drug and radiation cancer cell resistance, has motivated investigators to seek new treatment approaches to achieve greater incidence of curative outcomes and improved quality of life.

1.1.4. First strides in immunotherapy

In the 1990s, immunotherapy emerged as a means to engage the immune system in the fight against cancer. Antibodies specifically target tumor or immune cell receptors to block tumor function or recruit immune cells that will kill the target cancer cells. This strategy reduces off-site toxicities and side effects compared to traditional therapies. Immunotherapy proved successful in several solid tumors with the most notable examples being antibodies blocking immune-checkpoint proteins CTLA-4 and PD-1[18-20]. Most immunotherapy strategies are nonetheless ineffective in GBM. It is postulated that the immunopriviledged status of the brain and the immunosuppressive environment created by tumor cells contribute to the lack of positive outcomes.

GBM aside, one of the main disadvantages of this form of therapy is that tumor penetration is low, preventing full remission[21]. In addition, antibody clearance occurs rapidly, necessitating repeated treatments, leading to overall high therapy costs. In order to correct for this, the idea has been to use cells to continuously express these antibodies and therefore reduce the overall cost if curative.

1.2. Adoptive cell therapy for cancer

Adoptive cell therapy focuses on utilizing the body's natural immune defenses to treat cancer. The source of therapy is the patient himself and aims to counterbalance immune privilege by providing 'new' reactive cells to the body.

1.2.1. Tumor infiltrating lymphocytes (TIL)

Initial adoptive cell transfer therapy was developed by Rosenberg *et al.* in 1988 and comprised T-cells derived from the tumor-bearing host, referred to as tumor-infiltrating lymphocytes (TIL)[22]. The strategy is to obtain cancer biopsies from patients, cut them into pieces, and digest them, followed by culture in T cell medium containing large amounts of IL2 for a few weeks to stimulate T cell expansion. TILs were shown to confer improved prognosis in melanoma patients but remained unsuccessful in fully clearing the tumor due to immunosuppressive tumor microenvironment and lack of TIL persistence *in vivo*[23, 24]. Chemotherapy or radiotherapy lymphodepletion prior to TIL infusion was shown to improve efficacy[25]. Although TILs can effectively be expanded from most solid tumors, so far melanoma appears to be the only cancer for which TILs are capable of specific tumor cytotoxicity and durable responses in patients.

1.2.2. Engineered T cell receptors (TCR)

The earliest engineered T cell trials relied on *in vitro* gene transfer of synthetic T cell receptor (TCR) for improved antigen affinity. They consist of an α- and β- chain associated with the CD3 receptor on the cell surface. TCRs are either cloned from TILs and transduced into blood-derived T cells or generated by immunizing HLA-I/II transgenic mice with cancer antigens later transduced into human T cells[26]. These synthetic antigen receptors recognize intracellular or extracellular antigens presented by the major histocompatibility complex class I (MHC-I) at the surface of the cell the T cell binds to. An important limitation of this system is that many tumors downregulate MHC expression to evade recognition by TCR engineered T cells. In addition, lack of TCR affinity for cancer antigens is hypothesized to be a reason for lack of efficacy but high affinity increases chances of adverse events such as cross-reactivity in non-cancerous cells[27, 28].

1.2.3. Chimeric antigen receptors (CAR)

Chimeric antigen receptors consist of extracellular single-chain variable fragment (scFv) for antigen binding and intracellular costimulatory domains (CD28, 4-1BB, OX40, etc.)[29, 30]. Unlike TCRs, CARs are highly specific towards their antigen and can initiate the killing cascade in an MHC-independent fashion (Fig. 1.1). Chimeric antigen receptor design has been somewhat empiric in order to determine which elements of the CAR influence its signaling. The progress in design of CARs included first antigen specificity, then T cell activation mechanism, effector function and T cell persistence[31]. So far, CARs have only been able to target extracellular antigens, which limits the number of possible candidates. In

addition, antigen targets are rarely expressed throughout the tumor, which may explain the so far limited effectiveness in patients.

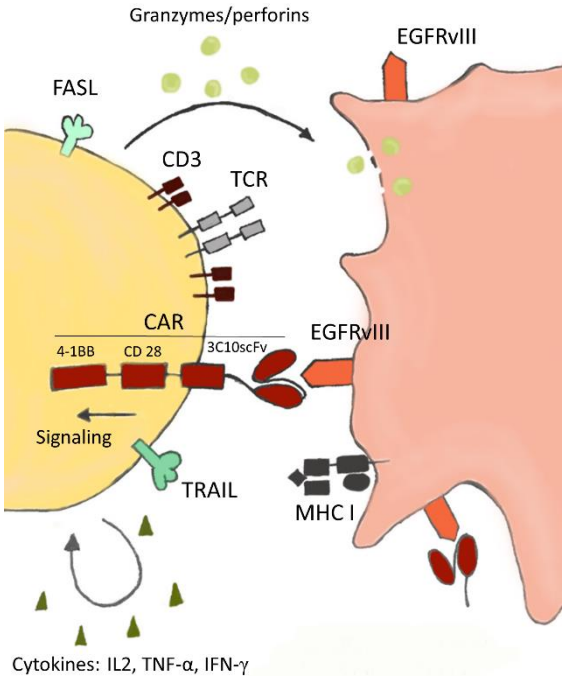

Figure 1.1: MHC-independent antitumor effects of CAR T cells against cancer cells. The antigen-specific scFv domain of the CAR recognizes its antigen on the target cancer cell. Using the co-stimulatory domains, the CAR receptor signals production of pro-inflammatory cytokines, granzyme and perforin release, and expression of FasL and tumor necrosis factor–related apoptosis inducing ligand (TRAIL). As a result of these processes, cancer cells are eradicated. Adapted from Cartellieri *et al.*[32]

Of interest for the treatment of glioblastoma multiforme is the Epidermal growth factor variant III (EGFRvIII). EGFRvIII originates from a mutation in EGFR resulting in a coding sequence deletion and expression of a surface neoantigen. EGFRvIII is only expressed on malignant tissue and occurs in about 24-60% of GBMs[33]. EGFRvIII-targeted CAR T cells have shown significant tumor reduction in preclinical models[34-36] and phase I clinical trials are currently underway to determine safety and efficacy in patients. Of note,

the CAR construct used throughout this thesis work targets EGFRvIII and was kindly provided by Dr. Okada at UCSF. Specifics of the construct are discussed in Chapter 2.

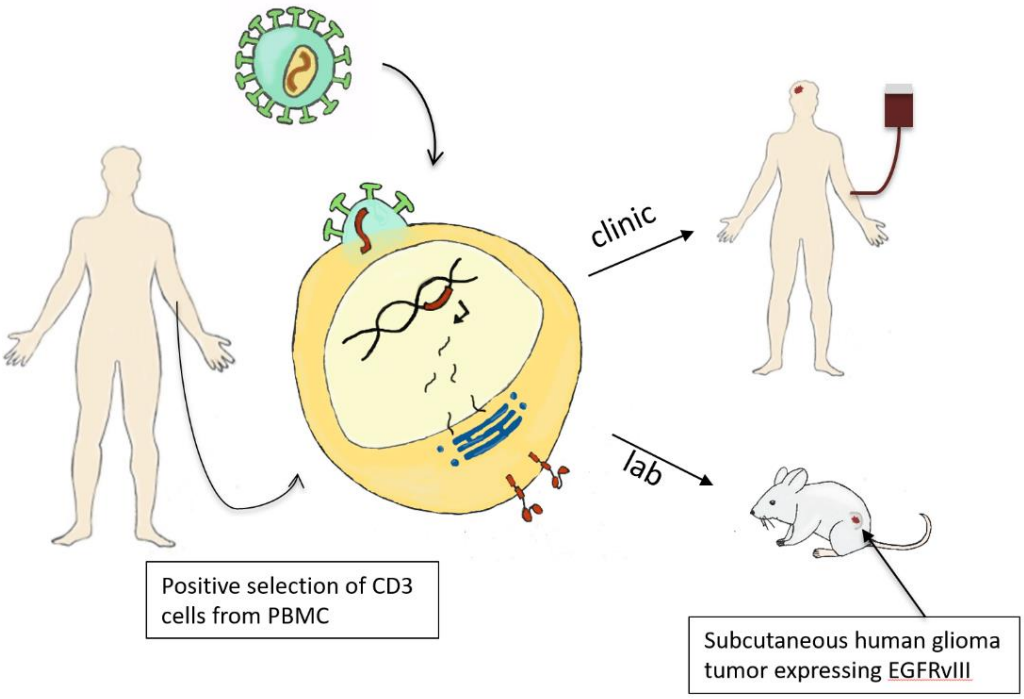

Figure 1.2: General approach for CAR T cell therapy. A blood sample is collected from the patient or a donor. CD3 positive T cells are isolated from the peripheral blood mononuclear cell suspension and expanded in culture. A lentiviral vector containing the CAR construct is added to the T cells and expression levels of the CAR receptor is confirmed by flow cytometry. The CAR T cells are then re-introduced to the patient in the clinic or used in pre-clinical models to determine their efficiency.

To produce CAR T cells, a blood sample is collected from either the patient or a donor and the T cells are isolated by gradient centrifugation and negative magnetic sorting (Fig. 1.2). The T cells are then exposed to a lentiviral vector carrying the CAR construct and expression at the surface of the cells is confirmed by flow cytometry. In the clinic, the produced CAR T cells would be re-infused into the patient for therapeutic effect. In pre-clinical testing, CAR T cells are infused to animal models. In this thesis, glioma tumors

(U87-EGFRvIII-Luc) expressing EGFRvIII and a luciferase reporter were injected subcutaneously in the flank of immune-compromized mice.

TCR and CAR T cell therapies are currently under investigation in over 300 clinical trials[37]. Combination of cell therapy with checkpoint blockade may enhance anti-tumor efficacy and remission rates[38]. All in all, immunotherapeutic strategies have emerged as the fourth pillar for cancer treatment which holds promise for fewer treatment side effects and more durable curative protections against residual primary cancers and metastases.

1.3. Rationale for *in vivo* cell tracking

1.3.1. Need for non-invasive tools to track cell therapy

A common assumption in preclinical and clinical research is that cell trafficking behavior *in vivo* may be predictive of therapeutic outcomes. For example, in CAR T cell trials against solid tumors[39], a reasonable assumption is that therapeutic cell survival and trafficking to the tumor sites is required for a putative therapeutic effect. However, clinicians are currently in the blind as to whether cells actually reach their desired tissue targets. Conventional methods to evaluate efficacy and survival of treatments include invasive biopsies followed by histopathology or flow cytometry. Histology is laborious and only semi-quantitative, and flow cytometry only provides partial information from tissue biopsy or peripheral blood sample. A surrogate biomarker capable of visualizing and quantifying sites harboring cells *in vivo* as well as survival of ACT at tumor and lymphoid organ regions would be invaluable for the assessment of putative therapeutic activity following systemic administration. In addition to diagnostic feedback, there is also a need to image off-target effects of therapies tested pre-clinically and clinically. All in all, non-invasive imaging

methods could help accelerate therapy development and improve patient management, while identifying key players in cancer response to therapy.

1.3.2. In vivo imaging modalities

There are multiple established methods to track cells *in vivo* non-invasively. These include optical imaging, tomography with radioactive tracers and magnetic resonance imaging. Optical imaging was the first non-invasive method developed using fluorescent moieties (Cydyes, DiO, DiD, etc.). Discovery of green fluorescent proteins (GFP) in the 1950s and bioluminescence from luciferases in the 1960s[40, 41] and engineering for imaging applications in the 1980s has made it the most used imaging method in preclinical research. Fluorescence and bioluminescence measurement accuracy is limited by depth attenuation; therefore, quantitative measurements should be limited to subcutaneous signals. Finally, optical imaging is not currently translatable to clinical practice or only for very limited applications such as lighting up cancer cells to guide surgeons during resection[42].

Magnetic Resonance Imaging (MRI) and PET are the best candidates for real time, quantitative assessment of tumor response[43-45]. PET and single-photon emission computed tomography (SPECT) provide functional information with modest spatial resolution and high sensitivity[46, 47], however, these modalities involve ionizing radiation shown to be detrimental to cells [48, 49] and label loss and decay limits longitudinal applications[50]. In addition, systemic injection of PET tracers such as ^{18}F-FDG may reveal false-positive hot spots at inflammatory sites as well as tumor sites which can confound image interpretation[51]. MRI allows anatomical and functional investigation as well as disease diagnosis and

progression assessment. Therefore, it is widely used in clinical practice and is often preferred over other diagnostic tools.

1.4. Magnetic resonance imaging

1.4.1. Metal-ion-based contrast agents for MR imaging

Due to its routine use in the clinics, conventional ^{1}H MRI contrast agents have long been the preferred probe choice for the development of contrasts agents highlighting cell sub-populations *in vivo*. The key constituents of ^{1}H MRI contrast agents are paramagnetic metals ions (e.g., Gd or Fe) that are conjugated to metal binding ligands or formulated as nanoparticles. Metal ions interact with surrounding mobile water molecules by through-space and contact magnetic interactions between the outer electrons and the water ^{1}H and/or by disruption of the local magnetic field in proximity to the probe [52]. The first generation of contrast agents consisted of gadolinium chelates, providing T1 contrast [53]. Many compounds received FDA approval and are widely used in the clinic. Nonetheless, the modest sensitivity of gadolinium chelates for cell tracking applications and the difficulty in labeling specific cell populations led to the use of super-paramagnetic iron oxide nanoparticles (SPIO). With a mean diameter of >5 nm, they can be taken up by cells, often with the aid of transfection procedures if cells are labeled *ex vivo*, and provide strong T_2 and T_2^* contrast enhancement. Ultrasmall superparamagnetic iron oxide nanoparticles (USPIO) have also been investigated, but one of the major limitation of these labeling agents remains sensitivity. Larger, micron-sized particles of iron oxide (MPIOs) provide greater contrast, but their large size restricts internalization in certain cells. USPIOs and MPIOs' large magnetic susceptibility can be exploited to create blooming artifacts and improve detection.

Gadolinium contrast media is routinely used in the clinic to improve image clarity but isn't suitable for *ex vivo* cell labeling. Gadolinium nanoparticles are not easily endocytosed by cells and is known to diffuse out of the cells. In addition, Gadolinium exhibits low magnetic susceptibility and therefore, signal enhancement by blooming artifact is impossible. In recent years there has been a large body of effort to design probes *de novo* that are optimized for the purpose of cell tracking using MRI [52]. Often these new materials are formulated as colloidal suspensions or nanoparticles that strive for improved cell deliverability, as well as image sensitivity and specificity.

1.4.2. Perfluorocarbon (PFC) probes for ^{19}F MR imaging

Shortly after the introduction of proton MRI, the feasibility of fluorine-19 (^{19}F) MRI was demonstrated by Holland *et al.*[54]. ^{19}F is a natural halogen, non-radioactive isotope of fluorine. ^{19}F has a relative sensitivity of 83% compared to ^{1}H and essentially devoid in biological tissues of interest[55], enabling background-free quantification of signals *in vivo*. One drawback of fluorine detection is the relative insensitivity of the signal, due to the low number of spins in the sample/animal. Perfluorocarbon (PFC) nanoemulsions containing large amounts of fluorine are specifically engineered to be endocytosed, even by non-phagocytic cells[56]. ^{19}F MRI signal intensity is linearly proportional to ^{19}F-atom concentration, enabling unbiased and specific measurements of cell numbers from the acquired images[57]. These materials are therefore referred to as 'tracer agents' rather than contrast agents. PFCs are generally biochemically inert and non-toxic *in vivo.* Their MRI sensitivity depends on their chemical structure. Cyclic PFCs such as perfluoro-15-crown-5-ether (PCE) and linear molecules such as perfluoropolyether (PFPE) are often used, with the

latter materials having desirable short T_1/T_2 ratios and endgroups that can be coupled with fluorescent dyes[58]. PFCs are formulated into small (<200 nm) nanoemulsions using surfactants. Key design considerations are discussed in Chapter 2.

1.4.3. Therapeutic cell labeling and tracking

Primary methods of probe delivery include labeling a cell population of interest *ex vivo* and delivering these cells intravenously or locally. The first application of ^{19}F MRI cell tracking was demonstrated by Ahrens *et al*. in 2005[59]. The alternative is *in vivo* labeling, which consists of direct intravenous (IV) injection of the agent that generally leads to labeling of the recipient's phagocytic cells in the reticulo-endothelial system. This enables imaging of inflammation in various disease models such as cancer, auto-immunity and graft rejection. Specifically, ^{19}F signal in foci of inflammation is linearly proportional to macrophage burden, which is an indicator of tumor aggressiveness or disease severity[60, 61].

Aside from inflammation imaging, a body of work exists detecting various types of stem and progenitor cells using ^{19}F MRI[62-67]. An early study used human hematopoietic stem cell (CD34+) to demonstrate that ^{19}F labeling does not impact the differentiation potential of the CD34+ cells to fully form the full repertoire of immune cell types in an irradiated mouse[68]. Others have shown the feasibility of mesenchymal stem cell imaging[62-64] with ^{19}F MRI. Similarly, Boehm-Sturm and coworkers as well as Bible *et al.* tracked PFC-labeled human neural stem cells after stroke induction in mice[65-67]

More recently, unprecedented efforts have been implemented to determine *in vivo* biodistribution, efficacy and persistence of immune cells using advanced MRI techniques.

Perfluorocarbon probes and ^{19}F MRI have enabled cell tracking in numerous preclinical and clinical studies for adoptive cell transfer employing T lymphocytes (TILs, TCRs, CARs)[56, 69-72], natural killer[73, 74], PBMC[75] and dendritic cell[43, 76, 77] therapies (Table 1.1). The recent first use of PFC MRI cell tracking in the clinic points to future developments of such compounds for numerous clinical applications[43].

Table 1.1: Overview of ^{19}F MRI applications in cell therapy for cancer. SC = subcutaneously, LN = lymph node, CNS = central nervous system, * = clinical trial

Cell type	Recipient species	Model	Tracer agent	Therapy delivery route	Imaging post-transfer (day)	Key findings	Reference
T-cell therapy							
Primary BALB/c mouse T cells	BALB/c mouse	N/A	BODIPy-TR PFPE	Intraperitoneal	2	T cell homing to the abdominal LN	Janjic (2008)
Human CAR T against EGFRvIII	SCID mouse	glioblastoma SC	CS-1000 ATM	Intravenously	2, 7, 14	CAR T cell homing to the tumors and spleen, reduced tumor growth	Chapelin (2017)
DO11.10 mouse T cells	BALB/c mouse	chicken ova SC	PFPE/PFPE -Alexa647	Intraperitoneal	4, 7, 11, 21	T cell homing to the draining inguinal LN and persistence over 3 weeks	Srinivas (2009)
Naïve T cells, OT-1 T cells	C57BL/6 mouse	melanoma expressing ova	CS-1000 ATM	Intravenously	1	No signal found in the tumor, but found in the chest (lungs), abdomen (liver) and left flank (spleen)	Gonzales (2016)
Pmel-1 cytotoxic T cells	C57BL/6 mouse	CNS glioma	PCE	Intravenously	3, 5, 7, 12	Significant pO2 increase in Pmel-1 treated mice at day 5 compared to controls	Zhong (2013)
NK cell therapy							
Human NK cells	NSG mouse	neuroblastoma SC	CS-1000 ATM	Subcutaneously or intratumorally	1, 3, 7/8, 10, 15	NK cell detection and persistence at injection sites, no evidence of migration	Bouchlaka (2016)
Human NK cells	NSG mouse	meduloblastoma CNS	CS-ATM DM Green	Intratumorally	0	*In vivo* visualization of NK cells after transfer	Somanchi (2016)
DC vaccines							
Mouse bone marrow-derived DC	C57BL/6 mouse	N/A	PCE	Intradermally in the limb	1	Migration of antigen-loaded DC from the footpad to the draining lymph node	Waiczies (2011)
In situ DC labeling	C57BL/6 mouse	CNS glioma	Rhodamine-PCE	Intravenously	1	Migration of *in situ* labeled DC to CNS tumors, reduced tumor growth	Ku (2016)
Mouse bone marrow-derived DC	C57BL/6 mouse	N/A	Rhodamine-PCE	Intradermally in the limb	0	Migration of Erk-/- DC to the draining popliteal lymph node	Ku (2016)
Autologous human DC vaccine*	Human	Metastatic colorectal cancer	CS-1000 (PFPE)	Intradermally in quadriceps	0, 1	Succesful first-in-man detection of DC vaccine in patients	Ahrens (2014)
PBMCs							
Human PBMC	Nude mouse, ham shank	N/A	CS-1000 ATM	Intradermally and intramuscularly	0, 2	Clinical protocol implementation for detection of PBMC in skin and muscle at 1.2 cm depth	Fink (2018)

Acknowledgements

Chapter 1, in part, contains text as it appears in two manuscripts: Springer book chapter entitled "Magnetic resonance imaging of immune cell trafficking in response to chemical agents in experimental autoimmune encephalomyelitis", Chapelin F, Ahrens E.T from "Visualizing chemical communication among migratory cells *in vivo*" (2018), and review paper entitled "Fluorine-19 MRI for detection and quantification of immune cell therapy for cancer" Chapelin F, Capitini C, Ahrens E.T, JITC 2018 with revisions and formatting changes for this dissertation. Besides this, the content of Chapter 1 is original. The dissertation author was the primary author of this book chapter and review paper.

References

1. Burnet, F.M. The concept of immunological surveillance. *Prog Exp Tumor Res* **13**, 1-27 (1970).

2. Thomas, L. On immunosurveillance in human cancer. *Yale J Biol Med* **55**, 329-333 (1982).

3. Liu, Y. & Zeng, G. Cancer and innate immune system interactions: translational potentials for cancer immunotherapy. *Journal of immunotherapy* **35**, 299-308 (2012).

4. Borghaei, H., Smith, M.R. & Campbell, K.S. Immunotherapy of cancer. *European journal of pharmacology* **625**, 41-54 (2009).

5. Dunn, G.P., Bruce, A.T., Ikeda, H., Old, L.J. & Schreiber, R.D. Cancer immunoediting: from immunosurveillance to tumor escape. *Nat Immunol* **3**, 991-998 (2002).

6. Shankaran, V., Ikeda, H., Bruce, A.T., White, J.M., Swanson, P.E., Old, L.J. & Schreiber, R.D. IFNgamma and lymphocytes prevent primary tumour development and shape tumour immunogenicity. *Nature* **410**, 1107-1111 (2001).

7. Schreiber, R.D., Old, L.J. & Smyth, M.J. Cancer immunoediting: integrating immunity's roles in cancer suppression and promotion. *Science* **331**, 1565-1570 (2011).

8. Bubenik, J. Tumour MHC class I downregulation and immunotherapy (Review). *Oncology reports* **10**, 2005-2008 (2003).

9. Dunn, G.P., Old, L.J. & Schreiber, R.D. The three Es of cancer immunoediting. *Annu Rev Immunol* **22**, 329-360 (2004).

10. Dolecek, T.A., Propp, J.M., Stroup, N.E. & Kruchko, C. CBTRUS statistical report: primary brain and central nervous system tumors diagnosed in the United States in 2005-2009. *Neuro Oncol* **14 Suppl 5**, v1-49 (2012).

11. Dohrmann, G.J., Farwell, J.R. & Flannery, J.T. Glioblastoma multiforme in children. *J Neurosurg* **44**, 442-448 (1976).

12. Ohgaki, H. Genetic pathways to glioblastomas. *Neuropathology* **25**, 1-7 (2005).

13. Louis, D.N., Perry, A., Reifenberger, G., von Deimling, A., Figarella-Branger, D., Cavenee, W.K., Ohgaki, H., Wiestler, O.D., Kleihues, P. & Ellison, D.W. The 2016 World Health Organization Classification of Tumors of the Central Nervous System: a summary. *Acta Neuropathol* **131**, 803-820 (2016).

14. Johnson, D.R. & O'Neill, B.P. Glioblastoma survival in the United States before and during the temozolomide era. *J Neurooncol* **107**, 359-364 (2012).

15. Fine, H.A., Dear, K.B., Loeffler, J.S., Black, P.M. & Canellos, G.P. Meta-analysis of radiation therapy with and without adjuvant chemotherapy for malignant gliomas in adults. *Cancer* **71**, 2585-2597 (1993).

16. Stupp, R., van den Bent, M.J. & Hegi, M.E. Optimal role of temozolomide in the treatment of malignant gliomas. *Curr Neurol Neurosci Rep* **5**, 198-206 (2005).

17. Hegi, M.E., Diserens, A.C., Gorlia, T., Hamou, M.F., de Tribolet, N., Weller, M., Kros, J.M., Hainfellner, J.A., Mason, W., Mariani, L., Bromberg, J.E., Hau, P., Mirimanoff, R.O., Cairncross, J.G., Janzer, R.C. & Stupp, R. MGMT gene silencing and benefit from temozolomide in glioblastoma. *N Engl J Med* **352**, 997-1003 (2005).

18. Lipson, E.J., Forde, P.M., Hammers, H.J., Emens, L.A., Taube, J.M. & Topalian, S.L. Antagonists of PD-1 and PD-L1 in Cancer Treatment. *Semin Oncol* **42**, 587-600 (2015).

19. Luke, J.J., Flaherty, K.T., Ribas, A. & Long, G.V. Targeted agents and immunotherapies: optimizing outcomes in melanoma. *Nat Rev Clin Oncol* **14**, 463-482 (2017).

20. Topalian, S.L., Taube, J.M., Anders, R.A. & Pardoll, D.M. Mechanism-driven biomarkers to guide immune checkpoint blockade in cancer therapy. *Nat Rev Cancer* **16**, 275-287 (2016).

21. Tabrizi, M., Bornstein, G.G. & Suria, H. Biodistribution mechanisms of therapeutic monoclonal antibodies in health and disease. *AAPS J* **12**, 33-43 (2010).

22. Rosenberg, S.A., Packard, B.S., Aebersold, P.M., Solomon, D., Topalian, S.L., Toy, S.T., Simon, P., Lotze, M.T., Yang, J.C., Seipp, C.A. & et al. Use of tumor-infiltrating lymphocytes and interleukin-2 in the immunotherapy of patients with metastatic melanoma. A preliminary report. *N Engl J Med* **319**, 1676-1680 (1988).

23. Disis, M.L., Wallace, D.R., Gooley, T.A., Dang, Y., Slota, M., Lu, H., Coveler, A.L., Childs, J.S., Higgins, D.M., Fintak, P.A., dela Rosa, C., Tietje, K., Link, J., Waisman, J. & Salazar, L.G. Concurrent trastuzumab and HER2/neu-specific vaccination in patients with metastatic breast cancer. *J Clin Oncol* **27**, 4685-4692 (2009).

24. Webb, J.R., Milne, K., Watson, P., Deleeuw, R.J. & Nelson, B.H. Tumor-infiltrating lymphocytes expressing the tissue resident memory marker CD103 are associated with increased survival in high-grade serous ovarian cancer. *Clin Cancer Res* **20**, 434-444 (2014).

25. Dudley, M.E., Wunderlich, J.R., Robbins, P.F., Yang, J.C., Hwu, P., Schwartzentruber, D.J., Topalian, S.L., Sherry, R., Restifo, N.P., Hubicki, A.M., Robinson, M.R., Raffeld, M., Duray, P., Seipp, C.A., Rogers-Freezer, L., Morton, K.E., Mavroukakis, S.A., White, D.E. & Rosenberg, S.A. Cancer regression and autoimmunity in patients after clonal repopulation with antitumor lymphocytes. *Science* **298**, 850-854 (2002).

26. Wang, M., Yin, B., Wang, H.Y. & Wang, R.F. Current advances in T-cell-based cancer immunotherapy. *Immunotherapy* **6**, 1265-1278 (2014).

27. Linette, G.P., Stadtmauer, E.A., Maus, M.V., Rapoport, A.P., Levine, B.L., Emery, L., Litzky, L., Bagg, A., Carreno, B.M., Cimino, P.J., Binder-Scholl, G.K., Smethurst, D.P., Gerry, A.B., Pumphrey, N.J., Bennett, A.D., Brewer, J.E., Dukes, J., Harper, J., Tayton-Martin, H.K., Jakobsen, B.K., Hassan, N.J., Kalos, M. & June, C.H. Cardiovascular toxicity and titin cross-reactivity of affinity-enhanced T cells in myeloma and melanoma. *Blood* **122**, 863-871 (2013).

28. Morgan, R.A., Chinnasamy, N., Abate-Daga, D., Gros, A., Robbins, P.F., Zheng, Z., Dudley, M.E., Feldman, S.A., Yang, J.C., Sherry, R.M., Phan, G.Q., Hughes, M.S., Kammula, U.S., Miller, A.D., Hessman, C.J., Stewart, A.A., Restifo, N.P., Quezado, M.M., Alimchandani, M., Rosenberg, A.Z., Nath, A., Wang, T., Bielekova, B., Wuest, S.C., Akula, N., McMahon, F.J., Wilde, S., Mosetter, B., Schendel, D.J., Laurencot, C.M. & Rosenberg, S.A. Cancer regression and neurological toxicity following anti-MAGE-A3 TCR gene therapy. *Journal of immunotherapy* **36**, 133-151 (2013).

29. Berry, L.J., Moeller, M. & Darcy, P.K. Adoptive immunotherapy for cancer: the next generation of gene-engineered immune cells. *Tissue antigens* **74**, 277-289 (2009).

30. Dotti, G., Savoldo, B. & Brenner, M. Fifteen years of gene therapy based on chimeric antigen receptors: "are we nearly there yet?". *Human gene therapy* **20**, 1229-1239 (2009).

31. Fesnak, A.D., June, C.H. & Levine, B.L. Engineered T cells: the promise and challenges of cancer immunotherapy. *Nat Rev Cancer* **16**, 566-581 (2016).

32. Cartellieri, M., Bachmann, M., Feldmann, A., Bippes, C., Stamova, S., Wehner, R., Temme, A. & Schmitz, M. Chimeric antigen receptor-engineered T cells for immunotherapy of cancer. *J Biomed Biotechnol* **2010**, 956304 (2010).

33. Heimberger, A.B., Suki, D., Yang, D., Shi, W. & Aldape, K. The natural history of EGFR and EGFRvIII in glioblastoma patients. *J Transl Med* **3**, 38 (2005).

34. Johnson, L.A., Scholler, J., Ohkuri, T., Kosaka, A., Patel, P.R., McGettigan, S.E., Nace, A.K., Dentchev, T., Thekkat, P., Loew, A., Boesteanu, A.C., Cogdill, A.P., Chen, T., Fraietta, J.A., Kloss, C.C., Posey, A.D., Jr., Engels, B., Singh, R., Ezell, T., Idamakanti, N., Ramones, M.H., Li, N., Zhou, L., Plesa, G., Seykora, J.T., Okada, H., June, C.H., Brogdon, J.L. & Maus, M.V. Rational development and characterization of humanized anti-EGFR variant III chimeric antigen receptor T cells for glioblastoma. *Sci Transl Med* **7**, 275ra222 (2015).

35. Miao, H., Choi, B.D., Suryadevara, C.M., Sanchez-Perez, L., Yang, S., De Leon, G., Sayour, E.J., McLendon, R., Herndon, J.E., 2nd, Healy, P., Archer, G.E., Bigner, D.D., Johnson, L.A. & Sampson, J.H. EGFRvIII-specific chimeric antigen receptor T cells migrate to and kill tumor deposits infiltrating the brain parenchyma in an invasive xenograft model of glioblastoma. *PLoS One* **9**, e94281 (2014).

36. Sampson, J.H., Choi, B.D., Sanchez-Perez, L., Suryadevara, C.M., Snyder, D.J., Flores, C.T., Schmittling, R.J., Nair, S.K., Reap, E.A., Norberg, P.K., Herndon, J.E., 2nd, Kuan, C.T., Morgan, R.A., Rosenberg, S.A. & Johnson, L.A. EGFRvIII mCAR-modified T-cell therapy cures mice with established intracerebral glioma and generates host immunity against tumor-antigen loss. *Clin Cancer Res* **20**, 972-984 (2014).

37. Sotak, C.H., Hees, P.S., Huang, H.N., Hung, M.H., Krespan, C.G. & Raynolds, S. A new perfluorocarbon for use in fluorine-19 magnetic resonance imaging and spectroscopy. *Magnetic Resonance in Medicine* **29**, 188-195 (1993).

38. John, L.B., Kershaw, M.H. & Darcy, P.K. Blockade of PD-1 immunosuppression boosts CAR T-cell therapy. *Oncoimmunology* **2**, e26286 (2013).

39. O'Rourke, D.M., Nasrallah, M.P., Desai, A., Melenhorst, J.J., Mansfield, K., Morrissette, J.J.D., Martinez-Lage, M., Brem, S., Maloney, E., Shen, A., Isaacs, R., Mohan, S., Plesa, G., Lacey, S.F., Navenot, J.M., Zheng, Z., Levine, B.L., Okada, H., June, C.H., Brogdon, J.L. & Maus, M.V. A single dose of peripherally infused EGFRvIII-directed CAR T cells mediates antigen loss and induces adaptive resistance in patients with recurrent glioblastoma. *Sci Transl Med* **9** (2017).

40. Greer, L.F., 3rd & Szalay, A.A. Imaging of light emission from the expression of luciferases in living cells and organisms: a review. *Luminescence* **17**, 43-74 (2002).

41. Shimomura, O. Discovery of green fluorescent protein (GFP) (Nobel Lecture). *Angew Chem Int Ed Engl* **48**, 5590-5602 (2009).

42. van Dam, G.M., Themelis, G., Crane, L.M., Harlaar, N.J., Pleijhuis, R.G., Kelder, W., Sarantopoulos, A., de Jong, J.S., Arts, H.J., van der Zee, A.G., Bart, J., Low, P.S. & Ntziachristos, V. Intraoperative tumor-specific fluorescence imaging in ovarian cancer by folate receptor-alpha targeting: first in-human results. *Nat Med* **17**, 1315-1319 (2011).

43. Ahrens, E.T., Helfer, B.M., O'Hanlon, C.F. & Schirda, C. Clinical cell therapy imaging using a perfluorocarbon tracer and fluorine-19 MRI. *Magn Reson Med* **72**, 1696-1701 (2014).

44. Kircher, M.F., Gambhir, S.S. & Grimm, J. Noninvasive cell-tracking methods. *Nat Rev Clin Oncol* **8**, 677-688 (2011).

45. Meller, B., Frohn, C., Brand, J.M., Lauer, I., Schelper, L.F., von Hof, K., Kirchner, H., Richter, E. & Baehre, M. Monitoring of a new approach of immunotherapy with allogenic (111)In-labelled NK cells in patients with renal cell carcinoma. *European journal of nuclear medicine and molecular imaging* **31**, 403-407 (2004).

46. Palestro, C.J., Love, C. & Bhargava, K.K. Labeled leukocyte imaging: current status and future directions. *The quarterly journal of nuclear medicine and molecular imaging : official publication of the Italian Association of Nuclear Medicine* **53**, 105-123 (2009).

47. Zhang, Y., Ruel, M., Beanlands, R.S., deKemp, R.A., Suuronen, E.J. & DaSilva, J.N. Tracking stem cell therapy in the myocardium: applications of positron emission tomography. *Current pharmaceutical design* **14**, 3835-3853 (2008).

48. Klenk, C., Gawande, R., Uslu, L., Khurana, A., Qiu, D., Quon, A., Donig, J., Rosenberg, J., Luna-Fineman, S., Moseley, M. & Daldrup-Link, H.E. Ionising radiation-free whole-body MRI versus (18)F-fluorodeoxyglucose PET/CT scans for children and young adults with cancer: a prospective, non-randomised, single-centre study. *The Lancet. Oncology* **15**, 275-285 (2014).

49. Brenner, W., Aicher, A., Eckey, T., Massoudi, S., Zuhayra, M., Koehl, U., Heeschen, C., Kampen, W.U., Zeiher, A.M., Dimmeler, S. & Henze, E. 111In-labeled CD34+ hematopoietic progenitor cells in a rat myocardial infarction model. *Journal of nuclear medicine : official publication, Society of Nuclear Medicine* **45**, 512-518 (2004).

50. Melder, R.J., Elmaleh, D., Brownell, A.L., Brownell, G.L. & Jain, R.K. A method for labeling cells for positron emission tomography (PET) studies. *Journal of immunological methods* **175**, 79-87 (1994).

51. Juweid, M.E. & Cheson, B.D. Positron-emission tomography and assessment of cancer therapy. *N Engl J Med* **354**, 496-507 (2006).

52. Ahrens, E.T. & Bulte, J.W. Tracking immune cells in vivo using magnetic resonance imaging. *Nature reviews. Immunology* **13**, 755-763 (2013).

53. Caravan, P., Ellison, J.J., McMurry, T.J. & Lauffer, R.B. Gadolinium(III) Chelates as MRI Contrast Agents: Structure, Dynamics, and Applications. *Chemical reviews* **99**, 2293-2352 (1999).

54. Holland G.N, B.P.A., Hinshaw W.S 19F magnetic resonance imaging *Journal of Magnetic Resonance* **28**, 133-136 (1977).

55. P., B. Pharmacokinetics using fluorine NMR in vivo. *Progress in Nuclear Magnetic Resonance Spectroscopy* **33**, 1-5 (1998).

56. Janjic, J.M., Srinivas, M., Kadayakkara, D.K. & Ahrens, E.T. Self-delivering nanoemulsions for dual fluorine-19 MRI and fluorescence detection. *Journal of the American Chemical Society* **130**, 2832-2841 (2008).

57. Srinivas, M., Morel, P.A., Ernst, L.A., Laidlaw, D.H. & Ahrens, E.T. Fluorine-19 MRI for visualization and quantification of cell migration in a diabetes model. *Magn Reson Med* **58**, 725-734 (2007).

58. Ahrens, E.T. & Zhong, J. In vivo MRI cell tracking using perfluorocarbon probes and fluorine-19 detection. *NMR in biomedicine* **26**, 860-871 (2013).

59. Ahrens, E.T., Flores, R., Xu, H. & Morel, P.A. In vivo imaging platform for tracking immunotherapeutic cells. *Nature biotechnology* **23**, 983-987 (2005).

60. Ahrens, E.T., Young, W.B., Xu, H. & Pusateri, L.K. Rapid quantification of inflammation in tissue samples using perfluorocarbon emulsion and fluorine-19 nuclear magnetic resonance. *Biotechniques* **50**, 229-234 (2011).

61. Khurana, A., Chapelin, F., Xu, H., Acevedo, J.R., Molinolo, A., Nguyen, Q. & Ahrens, E.T. Visualization of macrophage recruitment in head and neck carcinoma model using fluorine-19 magnetic resonance imaging. *Magn Reson Med* **79**, 1972-1980 (2018).

62. Gaudet, J.M., Ribot, E.J., Chen, Y., Gilbert, K.M. & Foster, P.J. Tracking the fate of stem cell implants with fluorine-19 MRI. *PLoS One* **10**, e0118544 (2015).

63. Ribot, E.J., Gaudet, J.M., Chen, Y., Gilbert, K.M. & Foster, P.J. In vivo MR detection of fluorine-labeled human MSC using the bSSFP sequence. *International journal of nanomedicine* **9**, 1731-1739 (2014).

64. Rizzo, S., Petrella, F., Zucca, I., Rinaldi, E., Barbaglia, A., Padelli, F., Baggi, F., Spaggiari, L., Bellomi, M. & Bruzzone, M.G. In vitro labelling and detection of

mesenchymal stromal cells: a comparison between magnetic resonance imaging of iron-labelled cells and magnetic resonance spectroscopy of fluorine-labelled cells. *Eur Radiol Exp* **1**, 6 (2017).

65. Bible, E., Dell'Acqua, F., Solanky, B., Balducci, A., Crapo, P.M., Badylak, S.F., Ahrens, E.T. & Modo, M. Non-invasive imaging of transplanted human neural stem cells and ECM scaffold remodeling in the stroke-damaged rat brain by (19)F- and diffusion-MRI. *Biomaterials* **33**, 2858-2871 (2012).

66. Boehm-Sturm, P., Aswendt, M., Minassian, A., Michalk, S., Mengler, L., Adamczak, J., Mezzanotte, L., Lowik, C. & Hoehn, M. A multi-modality platform to image stem cell graft survival in the naive and stroke-damaged mouse brain. *Biomaterials* **35**, 2218-2226 (2014).

67. Boehm-Sturm, P., Mengler, L., Wecker, S., Hoehn, M. & Kallur, T. In vivo tracking of human neural stem cells with 19F magnetic resonance imaging. *PLoS One* **6**, e29040 (2011).

68. van der Kolk, A.G., Hendrikse, J., Zwanenburg, J.J., Visser, F. & Luijten, P.R. Clinical applications of 7 T MRI in the brain. *Eur J Radiol* **82**, 708-718 (2013).

69. Chapelin, F., Gao, S., Okada, H., Weber, T.G., Messer, K. & Ahrens, E.T. Fluorine-19 nuclear magnetic resonance of chimeric antigen receptor T cell biodistribution in murine cancer model. *Scientific Reports* **7** (2017).

70. Gonzales, C., Yoshihara, H.A., Dilek, N., Leignadier, J., Irving, M., Mieville, P., Helm, L., Michielin, O. & Schwitter, J. In-Vivo Detection and Tracking of T Cells in Various Organs in a Melanoma Tumor Model by 19F-Fluorine MRS/MRI. *PLoS One* **11**, e0164557 (2016).

71. Srinivas, M., Turner, M.S., Janjic, J.M., Morel, P.A., Laidlaw, D.H. & Ahrens, E.T. In vivo cytometry of antigen-specific t cells using 19F MRI. *Magn Reson Med* **62**, 747-753 (2009).

72. Zhong, J., Sakaki, M., Okada, H. & Ahrens, E.T. In vivo intracellular oxygen dynamics in murine brain glioma and immunotherapeutic response of cytotoxic T cells observed by fluorine-19 magnetic resonance imaging. *PLoS One* **8**, e59479 (2013).

73. Bouchlaka, M.N., Ludwig, K.D., Gordon, J.W., Kutz, M.P., Bednarz, B.P., Fain, S.B. & Capitini, C.M. (19)F-MRI for monitoring human NK cells in vivo. *Oncoimmunology* **5**, e1143996 (2016).

74. Somanchi, S.S., Kennis, B.A., Gopalakrishnan, V., Lee, D.A. & Bankson, J.A. In Vivo (19)F-Magnetic Resonance Imaging of Adoptively Transferred NK Cells. *Methods in molecular biology* **1441**, 317-332 (2016).

75. Fink, C., Gaudet, J.M., Fox, M.S., Bhatt, S., Viswanathan, S., Smith, M., Chin, J., Foster, P.J. & Dekaban, G.A. (19)F-perfluorocarbon-labeled human peripheral blood mononuclear cells can be detected in vivo using clinical MRI parameters in a therapeutic cell setting. *Sci Rep* **8**, 590 (2018).

76. Ku, M.C., Edes, I., Bendix, I., Pohlmann, A., Waiczies, H., Prozorovski, T., Gunther, M., Martin, C., Pages, G., Wolf, S.A., Kettenmann, H., Uckert, W., Niendorf, T. & Waiczies, S. ERK1 as a Therapeutic Target for Dendritic Cell Vaccination against High-Grade Gliomas. *Molecular cancer therapeutics* **15**, 1975-1987 (2016).

77. Waiczies, H., Lepore, S., Janitzek, N., Hagen, U., Seifert, F., Ittermann, B., Purfurst, B., Pezzutto, A., Paul, F., Niendorf, T. & Waiczies, S. Perfluorocarbon Particle Size Influences Magnetic Resonance Signal and Immunological Properties of Dendritic Cells. *PLoS ONE* **6** (2011).

Chapter 2: Experimental methods focus

2.1. CAR T cell engineering

2.1.1. Construct

In order to optimize efficiency and cost, viral vector-based protocols are the most commonly employed for T cell transduction[1]. Lentiviral vectors can integrate large CAR constructs and continuously express the receptor after integration in the host cell DNA. CAR receptors are generally composed of (1) an extracellular antibody single chain variable fragment (scFv) specific to a given cancer antigen, (2) a CD3z domain to mimic the TCR intracellular signal-transduction pathway, (3) and a couple intracellular co-stimulatory domains such as CD28, 4-1BB, etc. We employed a vector for CAR consisting of a side chain fragment variable (scFv) specific to EGFRvIII fused to a CD8α hinge with 4-1BB, CD28 and CD3z intracellular domains (Fig. 2.1) as described by Ohno *et al*.[2].

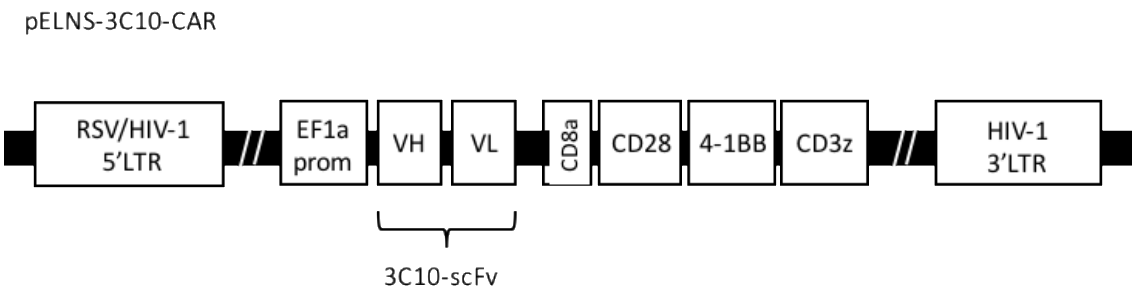

Figure 2.1: Schematic diagram of lentiviral pELNS-3C10-CAR vector. The EF1α promoter drives the CAR construct containing the 3C10 scFv for targeting of EGFRvIII. The CAR also incorporates CD28 as well as 4-1BB and CD3ζ domains. Abbreviations: RSV/HIV-1 5'LTR = Hybrid RSV promoter-R/U5 long terminal repeat; EF1α = Human elongation factor 1α-subunit promoter; VH = Variable region in the heavy chain of the 3C10 immunoglobulin; VL = Variable region in the light chain of the 3C10 immunoglobulin; HIV-1 Δ-3′LTR = Self-inactivating 3′ long terminal repeat with deletion in U3 region. Schematic is adapted from Ohno *et al*.[2].

pELNS-3C10-CAR bacterial streak was kindly provided by Dr. Okada at UCSF. A single colony is harvested with a pipette tip and expanded overnight in 3 ml of Luria Bertani media (BD, Sparks, MD) with 100 mg/ml Carbenicillin (Sigma Aldrich, St Louis, MO) in a shaking incubator at 37 °C. Transformed E-Coli are further expanded in 250 ml of Luria Bertani media overnight to obtain sufficient yield. Plasmid is then purified by Midiprep using the Nucleobond Xtra Midi kit (#740410.10, Macherey Nagel, Bethlehem, PA). Plasmid is reconstituted in 350 μl autoclaved water and kept at -20 °C before use. A 2 μl aliquot is used to determine yield on a Nanodrop 2000 spectrophotometer (Thermofisher, Waltham, MA). Packaging and envelope plasmids psPAX2 and pMD2.G are produced using the same protocol.

2.1.2. Virus production

The standard cell line for virus production is human embryonic kidney 293 cells (ATCC, Manassas, VA), referred to as 293T. They are renowned for transfection efficacy and high viral yields. For viral production, ten million 293T cells are plated in a T175 flask to establish ~ 70% confluence. Two transfection solutions are then prepared: (A) 4.5 ml of OptiMEM media (Gibco, Waltham, MA) with 180 μl of Lipofectamine 2000 (Invitrogen, Carlsbas, CA) and (B) 4.5 ml of OptiMEM media with 2.03 μg of pELNS-3C10-CAR, 1.57 μg psPAX2 and 0.41 μg pMD2.G. After a few minutes, (A) and (B) are combined and incubated for 20 minutes at room temperature. Media is then removed from the 293T cells and replaced with the transfection cocktail. Five hours later, transfection cocktail is aspirated and replaced by full Dulbecco's Modified Eagle's Medium (DMEM, Gibco) media. At 24 and 48 hours, 293T viral supernatant is harvested and filtered through a 0.22 μm filter.

Supernatant is then transferred to ultracentrifuge tubes and centrifuged at 16,000 rpm for 2 hours at 4°C. Tube supernatant is aspirated without disturbing the viral pellet. Pellet is resuspended in 150 μl Phosphate-Buffered Saline (PBS, Gibco) and used immediately. Transduction efficiency was first tested on Jurkat cells and then on primary human T cells. The optimal efficiency/viability was determined to correspond to 30 μl of virus per 1 million cells.

2.1.3. Human T cell isolation

Human T cells for CAR transduction are usually isolated from peripheral blood mononuclear cell (PBMC) preps for preclinical and clinical studies. In the lab, T cells are usually purified via gradient density centrifugation followed by negative magnetic sorting.

Gradient density centrifugation:

One unit of leuko-reduction system-white blood cell (LRS-WBC) blood is obtained from the San Diego Blood Bank. This blood sample is enriched in white blood cells (average $1.3x10^9$ per unit). In the biosafety cabinet, LRS-WBC blood is resuspended in sterile PBS without calcium and magnesium at 1:4 ratio. A 50 ml conical tube containing 16 ml of Ficoll (HiSep # LS001, Sigma Aldrich) is prepared and the diluted blood sample is gently added on the Ficoll layer to avoid mixing. The tube is centrifuged for 30 min at 300 g at room temperature without brakes. After centrifugation, the plasma layer sits on top of the tube, followed by the lymphocyte and monocyte layer, and finally the Ficoll with erythrocytes. The plasma layer is aspirated and the buffy coat (mononuclear cells) is gently collected. The layer gathered is rinsed with washing buffer (PBS + 0.5% bovine serum albumin + 2mM

EDTA) and centrifuged at 300 g for 10 minutes with regular brakes. The pellet is resuspended in 5 ml washing buffer and ready for magnetic sorting.

Magnetic-activated cell sorting (MACS)

For this step, the Miltenyi Pan T Cell Isolation kit (#130-096-535, MiltenyiBiotech Inc., Auburn, CA) is used, following the protocol provided by the supplier. Briefly, the cell suspension is filtered through a 40 μm filter to obtain a single cell suspension and counted. The cell suspension is resuspended in T Cell Biotin-Antibody Cocktail. This cocktail captures all CD3-negative cells. The Microbead Cocktail is then added and incubated to affix a magnetic bead to the antibodies that bound to cells. The cell suspension is then passed on a ferromagnetic column affixed to a magnet (MidiMACS Separator # 130-042-302). The flow through consists of the non-magnetically labeled T-cells. Isolated T-cells are counted and are expected to be about half of the initial cell count.

T cell culture conditions

T-cells need to be stimulated with IL2, CD3 and CD28 to maintain activity and grow in culture. Dynabeads Human T-activator CD3/CD28 (Gibco # 11131D) are used for this purpose. For fresh/thawed T cells, experience has shown that a concentration of 1-2 million T cells per ml of culture media is required for further expansion. Usually, 5-10 million cells are resuspended in 5 ml of full media (Roswell Park Memorial Institute (RPMI), 10% fetal bovine serum (FBS), 1% Penicillin/Streptomycin (Gibco) and 100 units/ml of human recombinant interleukin 2 (IL2, Peprotech, Rocky Hill, NJ). CD3/CD28 dynabeads (10 μl) are also added to the media for initial stimulation but not in subsequent media changes, unless T cell growth slows. Manufacturer recommends re-stimulation every 7-10 days. After

overnight culture, cells should appear as multi-cellular clumps or grapes around the dynabeads (Fig. 2.2). This is an indication of healthy culture conditions. Media is changed every other day to renew IL-2 until cells are used or frozen down.

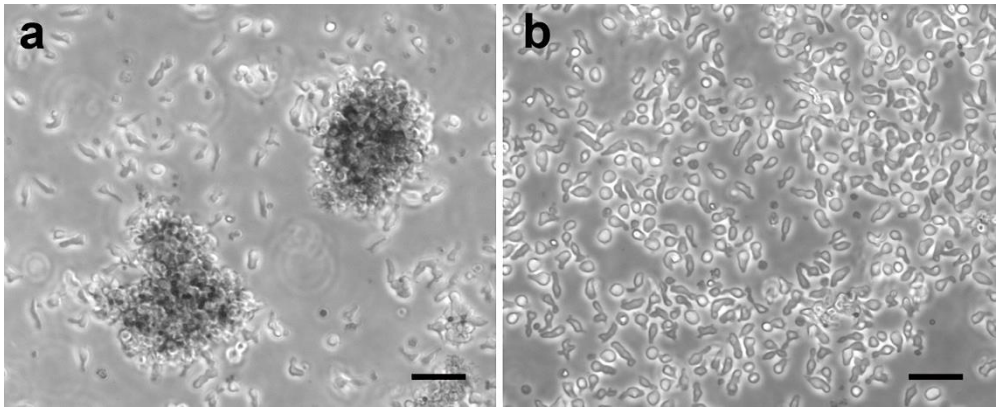

Figure 2.2: CAR T cell appearance in culture. (**a**) After initial stimulation, CAR T cells form clumps/grapes around the dynabeads. (**b**) After a couple weeks in culture, CAR T cells detached from dynabeads and appear as individual cells.

The dynabeads used for T cell activation are composed for superparamagnetic paramagnetic iron oxides and therefore create image artifacts on MR images. To remove dynabeads prior to *in vivo* use of T cells, cell suspension is transferred to a 15 ml conical tube and placed in a DynaMag-15 magnet for one minute. The magnet is tipped over a clean conical tube to collect cell suspension devoid of dynabeads. This step is repeated three times to guaranty removal of virtually all dynabeads.

2.1.4. Human T cell transduction

While in exponential growth phase and at the earliest passage possible (P1), human T cells are transduced with the CAR virus freshly produced. T cells are seeded in 6 well plates at a density of 1 million cells in 2 ml of full media (as above) and 3 μg/ml Polybrene (Polybrene Transfection Reagent, Millipore, Billerica, MA). 30 μl of CAR virus is added to each well and the 6-well plate is spinoculated for 1 hour at 1000 g at room temperature. The plate is then placed back in the incubator overnight. The next day, cells are centrifuged to remove the viral supernatant and resuspended in full media. Transduction efficacy is assessed after 5 days.

2.1.5. Expression of CAR

To obtain significant anti-tumor results, a population of T cells comprising at least 70%+ CAR T cells is desirable. Two flow cytometry methods enable CAR expression assessment on the surface of T cells. The first strategy is to co-incubate the transduced cells with a biotinylated EGFRvIII protein and detect bound cells with a fluorescent streptavidin secondary. The second strategy is to consider the mouse backbone of the CAR receptor and target it with an anti-mouse F(ab') antibody fragment. The latter is very specific and ~ 100 times cheaper than the modified EGFRvIII protein.

For flow analyses, newly generated CAR T cells and untransduced human T cells (negative control) are needed. Compensation beads are also used to minimize fluorescence spillover.

Flow markers used:

- hCD3- APC-Cy7 (Biolegend, San Diego, CA)
- hCD4-BV421 (Biolegend)
- hCD8-FITC (Biolegend)
- 'CAR'-PE

  Incubation with primary antibody Biotin-SP-conjugated Affinipure F(ab')2 Fragment Goat Anti-Mouse IgG, F(ab')2 fragment (dilution 1:200, 30 min at RT, Jackson Laboratories, Cat n. 115-066-006) followed by wash and secondary antibody Streptavidin-PE (dilution of 1:200, 15 min at 4 degrees, BD Pharmingen, Cat n. 554061).

- 7-AAD (viability, PerCP-Cy5.5): added just prior to FACS acquisition (Biolegend)

Conditions tested:

- CAR T cell sample: Unstained/Single color CD3/Single color CD4/Single color CD8/Single color 'CAR'/All colors
- Untransduced T cell sample: Unstained/All colors
- The viability marker 7-AAD can be added later on to the unstained sample for single color 7-AAD control as well as to 'All colors' sample.

Cell samples are resuspend cells to final concentration of 5×10^5 cells in 200 µl FACS buffer (# 4222-26, Invitrogen) + 1:100 heat inactivated human serum (Corning, NY) +1:100 FC Block (CD16/32 mouse, Biolegend) optional since cells are human) per tube. Tubes are

kept on ice 10 min in the dark. ‘CAR’ primary antibody is added to ‘single color ‘CAR’’ and ‘all colors’ tubes. Tubes are incubated 30 min at RT, rinsed with FACS buffer and spun 5 min at 1,000 rpm. Cells are resuspended in 200 µl FACS buffer + 1:100 heat inactivated human serum. Antibody cocktails are added to each tube at 1:200 dilution and incubated 15 min in dark on ice. Samples are rinsed twice with FACS buffer and spun 5 min at 1,000 rpm. Cells are resuspended in 600 µl of FACS buffer and transfered to clear FACS tubes with cell-strainer cap. Cell are kept in dark and on ice and resuspend gently before analysis on the Fortessa FACS machine (BD Biosciences, San Diego, CA). 5,000 events are recorded for the compensation samples and 10,000 events are acquired for all other samples. 7-AAD viability marker is added to the samples minutes before recording viability data.

Gates are established based on the unstained and untransduced T cell control (Fig. 2.3 and 2.4) and the fraction of PE-positive events (CAR-T cells) is then determined. For each batch of CAR T cells produced, initial transduction efficacy was measured ~5 days after addition of the virus and at regular intervals until administration to the mouse.

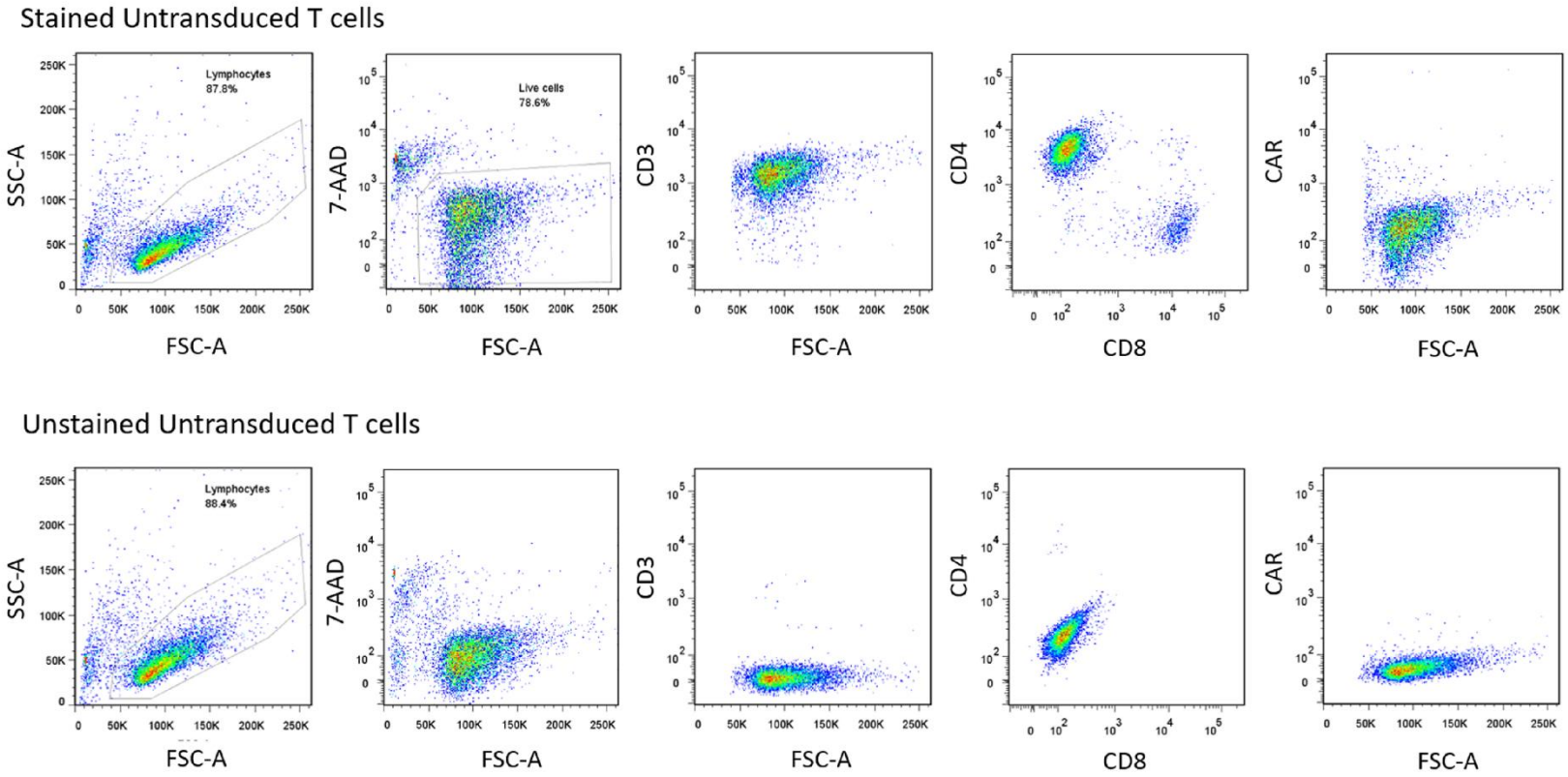

Figure 2.3: Flow characterization of untransduced human T cells. The panels displayed correspond to human T cells after 4 passages in culture. The top panel shows stained T cells and the bottom panel shows corresponding unstained control. Untransduced T cells are 99 % CD3 +, 89 % CD4+ and 9 % CD8+ and CAR negative.

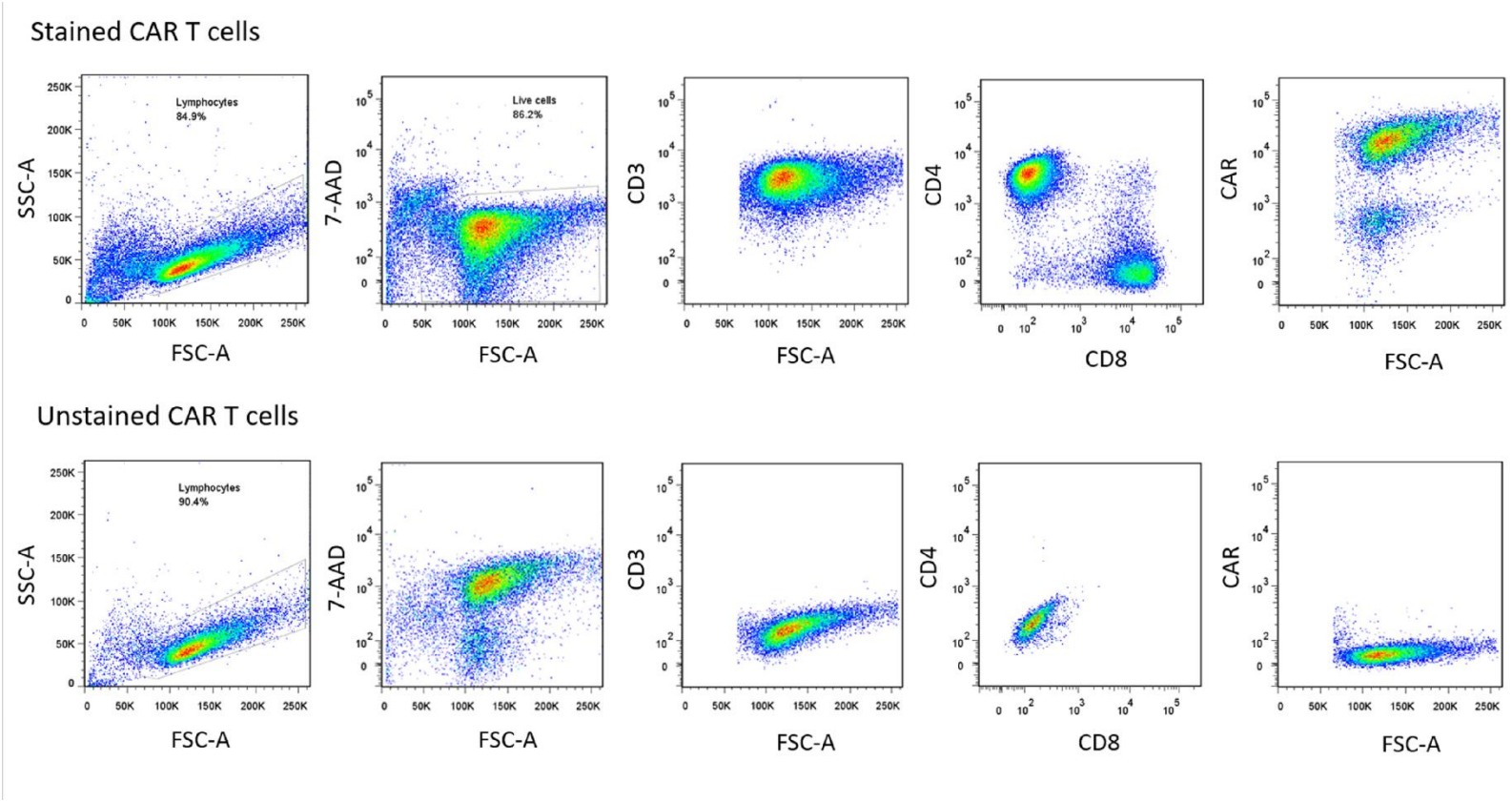

Figure 2.4: Flow characterization of CAR T cells. The panels displayed correspond to T cells 4 passages after transduction with CAR. The top panel shows stained CAR T cells and the bottom panel shows corresponding unstained control. CAR T cells are 99 % CD3 +, 74% CD4+, 22 % CD8+ and 85 % CAR +.

2.2. Perfluorocarbon emulsion formulation

2.2.1. Perfluorocarbons- basic properties

PFCS are hydrocarbons in which hydrogen atoms are replaced by fluorine atoms. PFC molecules have properties that are attractive for cell labeling and ^{19}F MRI tracking applications[3]. Their strong C-F covalent bonds render them chemically inert and are not metabolized *in vivo*[4]. Moreover, PFCs often display simultaneous lipo- and hydro-phobic properties[5] and do not dissolve in cell membranes. PFCs commonly used for ^{19}F MRI imaging include perfluoropolyether (PFPE), perfluoro-15-crown-5-ether (PCE) and perfluorooctyl bromide (PFOB)[3] (Fig. 2.5). PFPE and PCE are linear and cyclic polymers, respectively, each with numerous chemically-equivalent fluorine yielding high MRI sensitivity. PFOB has less MRI sensitivity overall due to chemically inequivalent F-sites[6], but is slightly lipophobic due to its single Br atom, which accelerates body clearance of the agent.

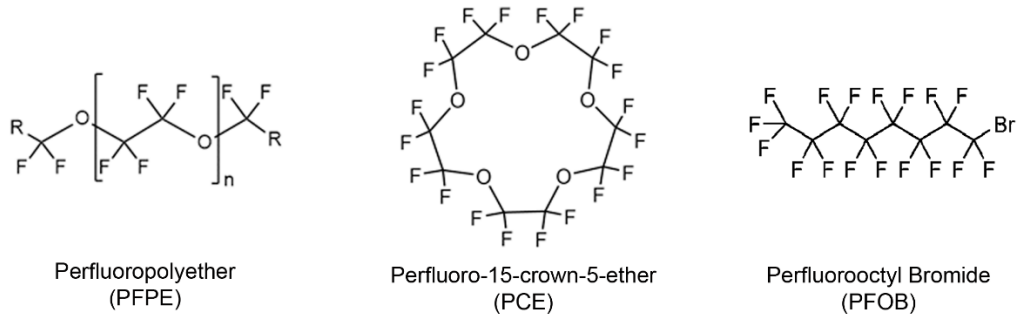

Figure 2.5: Molecular structure of PFPE, PCE and PFOB. PFPE possesses over 40 equivalent fluorine atoms in the main chain with a resonance at -91.3 ppm on ^{19}F NMR spectra and 4 in the end groups (resonance at -80.2 ppm). PCE is a macrocycle with 20 equivalent fluorine atoms resulting in a single resonance at -92.5 ppm. PFOB is a linear perfluorocarbon with a bromide atom resulting in 8 resonances on ^{19}F NMR spectra.

An interesting intrinsic property of PFCs is that they display weak molecular cohesion, enabling gas dissolution [5]. In fact, extensive work was conducted in the late 1990's [7, 8] to emulsify PFCs into biocompatible, excretable, and readily injectable blood substitutes to address hospital blood shortages [9]. Building on *in vivo* cytometry technology, a logical extension is to exploit known bio-sensing properties of the PFC molecules inside the cell. Specifically, certain PFC molecules readily coordinate paramagnetic oxygen, which shortens the ^{19}F spin-lattice relaxation time (T_1), where T_1 varies linearly with the absolute partial pressure of oxygen (pO_2) [10]. (T_1 is the characteristic time constant for the ^{19}F nuclei to align along the MRI's magnetic field, on the order of 0.5 to 2 s.) PFC emulsions have previously been used to measure pO_2 *in vivo* using MR techniques [11-14]. However, a novel use of ^{19}F-based cell tracking is to use ^{19}F T_1 measurements to monitor intracellular oximetry. This will be the subject of Chapter 4.

2.2.2. Key engineering properties of nanoemulsions for cell labeling

Key design considerations in nanoemulsion formulation include a small droplet size (typically 50-200 nm), a narrow size range (e.g., polydispersity index <0.2) and a high fluorine concentration (~20-30% w/v) to minimize volume added to culture. Nanoemulsion formulations may also be complexed with fluorophores, for example near infrared dyes, to create 'dual-mode' agents [3, 15, 16]. Recent reviews exhaustively cover PFC nanoemulsion design [3, 17].

Different published studies use a range of emulsion particle sizes [16, 18]. The resulting mean emulsion droplet size can impact the cell labeling process. Larger oil droplets (>200

nm) experience a larger centrifugal force during washing, and this force can potentially pellet the labeling agent along with the cells thereby confounding the wash process [19]. Larger particle sizes are effective in labeling flask-adherent cells, such as DCs, where successful wash steps can be implemented. A smaller droplet size (<180 nm) allows excess agent not taken up by cells to be discarded with the supernatant during wash. Emulsion production ideally yields a homogenous size distribution, which is easier to achieve with smaller droplet sizes. Unintended, outlying large droplets ('stability demons') may evade detection in dynamic light scattering particle size measurements of the batches. These demons can lead to emulsion instability over time [20] and may spin-down with the cells. Overall, in properly designed experiments, any free residual emulsion in the cell inoculant is de minimis and inconsequential in view of detection limits of the MRI technique.

2.2.3. Surfactants

Neat PFC materials are dense oils. Emulsification is used to make a colloidal suspension of the PFC oil that is stabilized using a surfactant. Surfactants reduce the interfacial tension between water and PFC oils, thereby stabilizing the oil droplets. The surfactant coat can also impart desirable surface properties that promote cell uptake in culture [21, 22]. The most commonly used classes of surfactants are pluronics and phospholipids [23]. Pluronics are commercially available block co-polymers that come in different chain lengths and hydrophilic/hydrophobic properties. F68 is a common pluronic (Fig. 2.6) for emulsion formulation and was used in the experiments of Chapters 4 and 5.

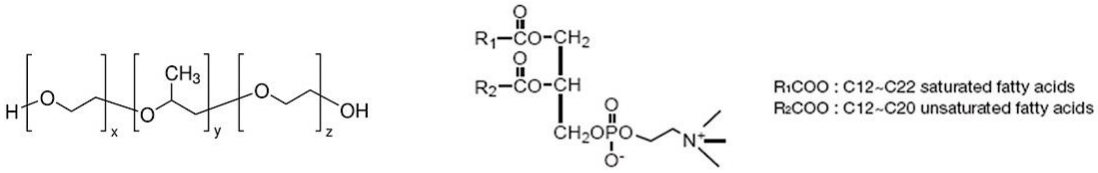

Pluronic block co-polymer F68 Egg yolk phospholipid (EYP)

Figure 2.6: Molecular structure of pluronic F68 and egg yolk phospholipid (EYP). F68 consists of hydrophilic ethylene oxide (x and z) and hydrophobic propylene oxide (y) repeats conferring optimal surfactant properties. EYP is an amphipathic structure comprising a hydrophilic polar head followed by saturated and unsaturated lipophilic fatty acid chains.

Egg yolk phospholipid is a common amphipathic lipid surfactant (Fig. 2.6). It is purified from egg yolks by column chromatography to remove neutral lipids and cholesterol. These are already used clinically in injectables as they enable long circulation in plasma.[24]. Nonetheless, our experience has shown that EYP is not an ideal candidate for cell labeling *in vitro* with occurrences of coalescence on the cell membrane instead of internalization. Another limitation that will be further discussed in Chapter 4 is that the unsaturated fatty acid tails oxidize in the presence of metals, creating toxic products.

2.2.4. Emulsion formulation and characterization

Sonication is a routine technique to formulate emulsions. Ultrasonic waves break intermolecular bonds and disperse the molecules in solution. Nonetheless, sonication engenders significant heat release, which may be detrimental for certain surfactants. In addition, sonication is uniform only for small volumes, which limits the scale up and reproducibility. Finally, sonication alone usually yields emulsions with wide size distributions[25, 26], which is detrimental for cell labeling applications. Microfluidization, a

high shear homogeneization technique, is another common method for emulsion formulation. A pre-mix of PFC, surfactant, and water is pushed through an inlet reservoir and forced into a fixed-geometry chamber by a high pressure pump. Microfluidization produces smaller size nanoemulsions with narrow size distributions, which are better suited for cell labeling applications. For the experiments in chapters 4 and 5, two-minute sonication followed by 4 passes on the microfluidizer (LV1, Microfluidics, Westwood, MA) were used to formulate the crown-ether emulsions. Microfluidizer stroke was 6 ml, piston diameter was 11 mm, pump pressure was set at 20,000 PSI and the interaction chamber and cooling coil were kept on ice to avoid heating of the emulsion.

Emulsion size and polydispersity index (PdI) are measured by dynamic light scattering (DLS, Zetasizer, Malvern, Northhampton, MA). These are acquired at different time intervals and in different conditions (storage temperature, serum vs plain emulsion, etc.) to evaluate stability. In the lab, emulsions with a ratio of surfactant (F68) between 5-10% yielded emulsion sizes of 170-190 nm and a PdI of 0.08-0.12. PCE-F68 emulsions were stable for >3 weeks at 4°C and at room temperature.

Eventually, nanoemulsions degrade via coalescence and Ostwald ripening[27]. Nanodroplets spontaneously attempt to reduce the interfacial surface area by coalescence, thereby increasing the mean droplet size. Ostwald ripening consists of smaller droplets being more soluble in the bulk phase and diffusing to larger droplets, raising their diameter. These are major challenges in emulsion formulation and engineering strategies to delay this process are heavily investigated to enable long shelf life of future clinical products.

2.2.5. Enhanced nanoemulsions

The principle bottleneck that remains for longitudinal tracking of transferred immune cells is ^{19}F MRI sensitivity. Strategies to increase cell loading include but are not limited to the use of transfection agents, electroporation, metalation, and coating of the nanoemulsions with cell penetrating peptides. Transfection agents and electroporation have not been shown to drastically improve fluorine uptake in conditions that preserve cell viability and function. Cell penetrating peptides such as the transactivator of transcription (TAT) from human immunodeficiency virus can be employed to enhance PFC cell loading. TAT peptides have been heavily studied and are known to facilitate cell loading of a range of cargo, including micelles and polymersomes[28, 29]. Incorporation of TAT peptide into nanoemulsions formulated with either lipid or pluronic (block co-polymer) surfactants is explored in Chapter 4 (Figure 2.7).

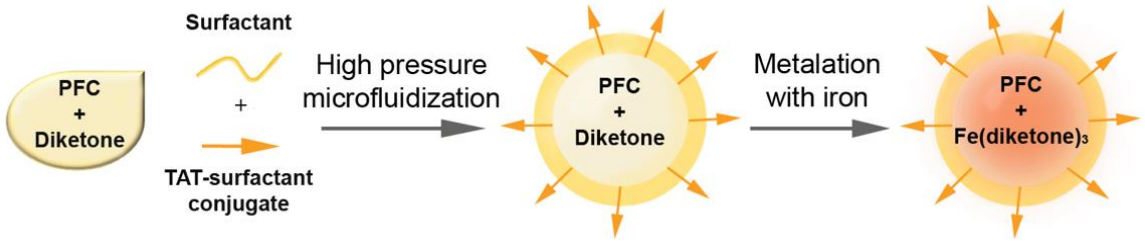

Figure 2.7: Nanoemulsion design for MR sensitivity enhancement. Diketone chelator is blended with the fluorous phase of the emulsion. The resulting blend is formulated into a nanoemulsion incorporating TAT-surfactant moieties, and subsequently metalated with iron.

Iron(III)-bound fluorinated chelates, localized within the fluorous phase of a PFC nanoemulsion, have been shown to be relatively stable and induce strong spin-lattice relaxation time (T_1) reduction, thereby increasing cell detection sensitivity[30].

2.3 Immune cell labeling

2.3.1. Determinants of cell uptake

Cell labeling in culture is generally performed by simple co-incubation with contrast/tracer agent as another factor in the media, followed by a wash step. Physical techniques such as hypotonic swelling or electroporation have been used[31], but chemical transfection techniques are most common. In the case of superparamagnetic iron oxide nanoparticles for proton imaging, the idea is to balance the negative charge of the particle surface with cationic transfection agents such as protamine sulfate or Fugene[32] to improve cell loading. Though necessary, these labeling techniques remain controversial since the use of transfection agents or other physical manipulations increase the risk of diminished cellular viability and phenotype alterations. In the case of PFC cell labeling, generally the same labeling methodology considerations apply. However, we note that 'self-delivering'[16] PFC cell labeling agents have been devised that do not require any extra transfection agents or mechanical cell perturbations.

Labeling periods range from several hours [33-36] to a day or more [37-39] to allow for endocytic uptake to occur. Determinants of obtainable PFC cell uptake include (i) dose of PFC in media, (ii) cell cytoplasmic volume and (iii) phagocytic properties of cells. Typically, several concentrations and incubation times are tested to optimize uptake while minimizing potential cell viability and phenotype alterations [16].

2.3.2. Specific case of lymphocytes

Phagocytic cells such as macrophages and DCs possess a large cytoplasmic volume [40] and thus are readily labeled to high levels of PFC. In contrast, lymphocyte labeling can be challenging due to their small cellular and cytoplasmic size that limits the number of probe droplets it can hold. In addition, lymphocytes are not naturally phagocytic. Optimal labeling efficiency is attained when cells are in log phase of division. PFC uptake will follow a dose response in the shape of a sigmoidal curve (Fig. 2.8) [39]. A critical factor for strong labeling of lymphocytes is that the culture must be viable and actively expanding, typically aided by aggressive cytokine and co-stimulatory molecule engagement (*e.g.*, irradiated 4-1BBL/IL-15 expressing feeder cells, CD3/CD28 beads, etc.) as discussed elsewhere [37, 41]. Engineered PFC probes enable labeling of lymphocytes for *in vivo* tracking without the use of transfection agents [16], as shown in preclinical studies [3, 42].

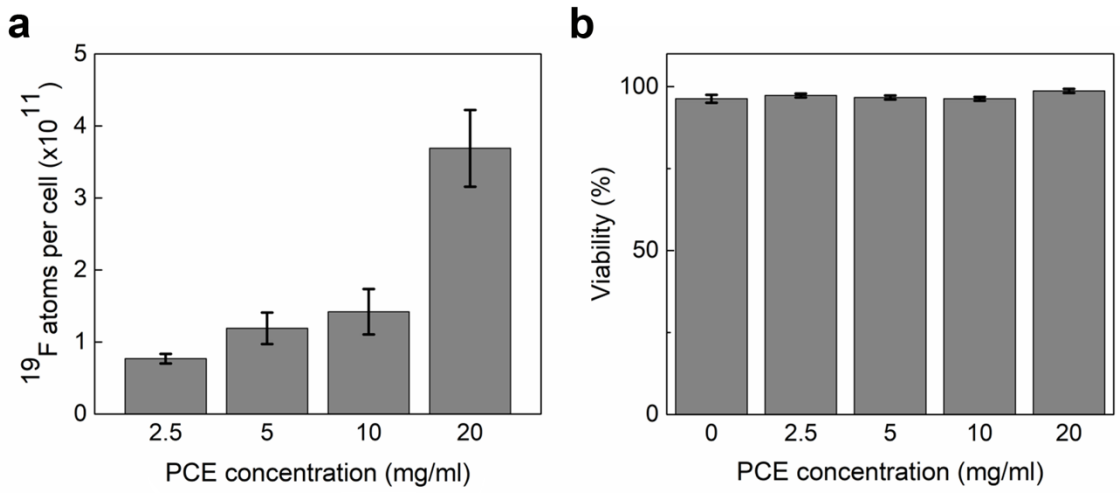

Figure 2.8: CAR T cell labeling with PFC nanoemulsion. (**a**) CAR T cell sigmoidal uptake of a PCE-F68 emulsion as measured by ^{19}F NMR and (**b**) corresponding cell viability.

2.3.3. Confirmation of intracellular uptake

After washes, cell labeling levels can be measured in a pellet sample using conventional ^{19}F NMR spectroscopy to yield the mean ^{19}F/cell. Various cell microscopy methods have been used to validate intracellular compartmentalization of PFC droplets. Using transmission electron microscopy, the emulsion droplets appear as electron-sparse ovoids against counterstain [18, 43, 44]. Emulsion droplets often coalesce into encapsulated vesicles consistent with lysosomal storage in lymphoid-type and stem cells [45].

Dual-mode, PFC-fluorescence emulsions [16] containing bright fluorescent dyes enable flow cytometry of labeled cells, as well as optical microscopy in histology tissues. Confocal microscopy images of labeled immune cells clearly show intracellular localization (Fig. 2.9a). PFC localization is inconsistent with dominate cell surface labeling, which has been confirmed by explicit cell membrane staining using a second fluorescent dye targeting cell surface markers (Fig. 2.9a), or cellular proliferation dyes such as 5(6)-Carboxyfluorescein N-hydroxysuccinimidyl ester (CFSE)[37]. Detailed fluorescent microscopy studies using a dual-mode emulsion with a pH sensitive dye confirm that the PFC emulsion traffics into low-pH (lysosomal) vesicles over time [45]. This intracellular compartmentalization is the steady-state in living cells, as the PFC is not degraded in the cell and there is no evidence for active exocytosis [45]. Thus, verification of PFC nanoemulsion location within a cell is not typically necessary given its aggregation tendency and it is compartmentalized in a manner consistent with other nanostructures of similar size.

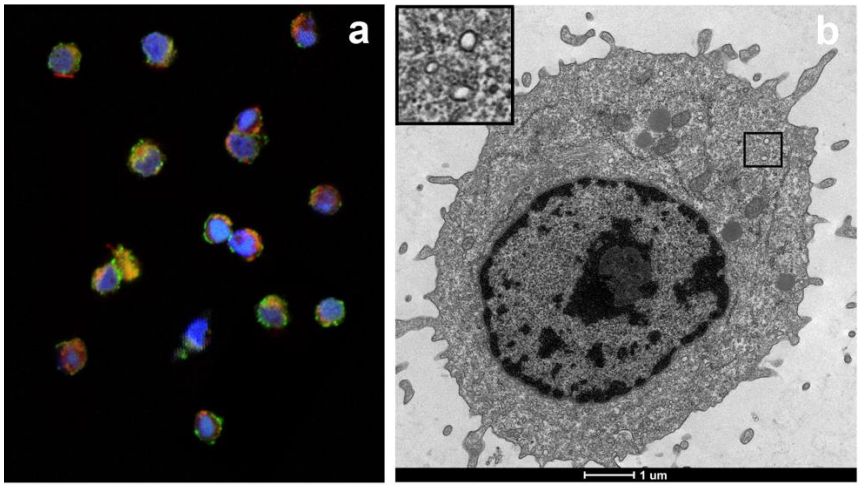

Figure 2.9: Confirmation of intracellular localization of PFC nanoemulsion in CAR T cells. Panel (**a**) is a confocal microscopy image depicting CAR T cells with internalized dual mode PFC-Red agent. The nuclei are labeled with Hoeschst Nuclear stain and the membrane with CD3-FITC.

2.3.4. Viability and phenotype testing

Cell labeling should not alter cell viability, proliferation, phenotypic markers, or function, as described in several reports [46, 47]. PFCs have not been shown to change any of these characteristics in the multiple cell lines tested. The most detailed *in vitro* study to date involved PFC labeled primary human DCs [39]; cells were assayed for viability, maturation phenotype, cytokine production, T cell stimulatory capacity, and chemotaxis [39], and no differences in these parameters were observed between labeled and unlabeled cells [39].

In the study described in Chapter 3, potential impact of PFC labeling was evaluated by measuring CD4, CD8, and 7-AAD viability marker by flow cytometry, as well as CAR T cell proliferation rate, at day 2, 7 and 14 post-labeling and compared to unlabeled control. Labeling experiments with PFC nanoemulsions at 10 mg/ml over a period of 12-hour co-incubation displayed minimal viability impairment as assessed by Trypan blue exclusion test

(Average 95±1%, N=3 replicates) and flow cytometry viability measurements (Table 2.1, $p>0.05$). Moreover, PFC labeling does not appear to alter T cell phenotype as defined by CD4+ and CD8+ expression (Table 2.1, $p>0.05$).

Table 2.1. Longitudinal characterization of PFC-labeled CAR T cells. Table displays average doubling time, CD4/CD8 ratio and viability as measured by flow cytometry of PFC labeled CAR T cells and control unlabeled CAR T cells at days 2, 7 and 14 after PFC labeling (N=3 replicates). No significant differences were seen between labeled and unlabeled CAR T cells for all criteria.

CAR T cells	Time point	day 2	day 7	day 14
Labeled	Doubling time (h)	35	41	40
	CD4:CD8 ratio	91:7	94:4	91:7
	Viability (flow) (%)	57	79	83
Unlabeled	Doubling time (h)	34	39	41
	CD4:CD8 ratio	94:6	95:1	94:5
	Viability (flow) (%)	64	74	83

2.4. Fluorine imaging methods

2.4.1. Quantification of emulsion concentration and cell uptake by NMR

^{19}F NMR measurements were gathered using a 400 MHz Bruker Advance NMR spectrometer. The ^{19}F NMR spectra were acquired using: 17 μs pulse, 32,000 points acquired for free induction decay (FID), 100 ppm spectral width, 32 averages, and a recycle delay of 15 s. For emulsion concentration calculation, 30 μl PFC nanoemulsion was added to 270 μl 0.1% (w/v) Sodium Trifluoroacetate (TFA) in D_2O. Perfluorocarbon concentration (C_{PFC}, mg/mL) was determined by using the relative integrals of the TFA signal (I_{TFA} = 1, -76.6 ppm) and the perfluorocarbon signal (I_{PFC}). As per the following equation:

$$C_{PFC} = \frac{A\, I_{PFC}\, C_{TFA} V_{TFA}}{B V_{PFC}}$$

C_{PFC} and C_{TFA} represent the concentration of perfluorocarbon emulsion and TFA respectively in mg/ml in the NMR sample, V_{PFC} and V_{TFA} indicate the respective volumes of nanoemulsion and TFA solution in ml in the NMR sample, A and B are constants to account for the percentage of fluorine by mass in TFA and PFC respectively (A = 42, B = 65.5 for PCE and 58 for PFPE).

For uptake experiments, 1 million cells were plated in 1 ml full media in 24 well plates (n=3 wells per condition). PCE emulsions were added to each well and incubated overnight (16 h) at 37 ºC, 5% CO_2. The cells were then washed three times with phosphate buffered saline (PBS) to rinse free emulsion. Cells were counted and viability was assessed by trypan blue staining. Thereafter, the cells were spun down, resuspended in 150 μl lysis buffer (1% Triton X in PBS) and transferred to a 5mm NMR tube. Fifty microliter 0.1% TFA was added to each tube and ^{19}F NMR spectra were acquired (Fig. 2.10). Number of ^{19}F atoms per cell was determined with the same equation as above and divided by the number of cells in each NMR tube.

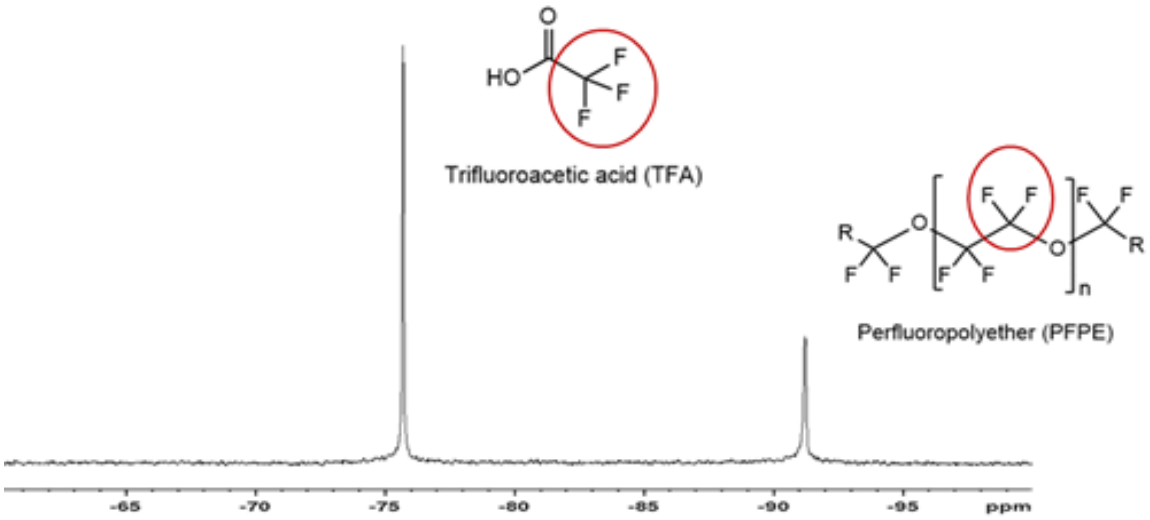

Figure 2.10: Representative ^{19}F NMR spectrum (9.4T) of CAR T cell pellet labeled with PFPE emulsion. The TFA reference registers at -76 ppm and the labeled cell pellet at -91.3 ppm. The ratio of integrals multiplied by the number of TFA atoms and divided by the number of cells in the NMR tube yields the average uptake per cell.

2.4.2. NMR cytometry limits of detection (LOD)

Limits of detection were also assessed on the 400 MHz NMR spectrometer. Exchangeable 5 mm and 10 mm sample-NMR probes (Bruker models BBFO and BBO, respectively) were evaluated. Sample standards with varying ^{19}F content were prepared from serial dilutions of 0.05 to 0.5% TFA/D_2O in volumes of 250 or 1,500 µl for 5 or 10 mm probes, respectively. All sample spins were contained within the receptive field of the NMR probe. The ^{19}F NMR spectra were acquired using: 17 µs pulse, 32,000 points acquired for free induction decay (FID), 100 ppm spectral width, 128 averages, 20 min acquisition time, and a recycle delay of 10 s. The signal-to-noise ratio (SNR) of the TFA spectra were calculated using TopSpin software (Bruker, Billerica, MA). The results were plotted as the SNR versus ^{19}F content measured for each NMR sample probe (5 or 10 mm), and LOD was defined as the ^{19}F atom count where the extrapolated SNR=2 (Fig. 2.11). LOD were

approximately ~ 10^{14} and ~10^{15} ^{19}F atoms for the 5 and 10 mm probe respectively, corresponding to ~7×10^3 and ~4×10^4 cells assuming typical ^{19}F labeling levels in T cells.

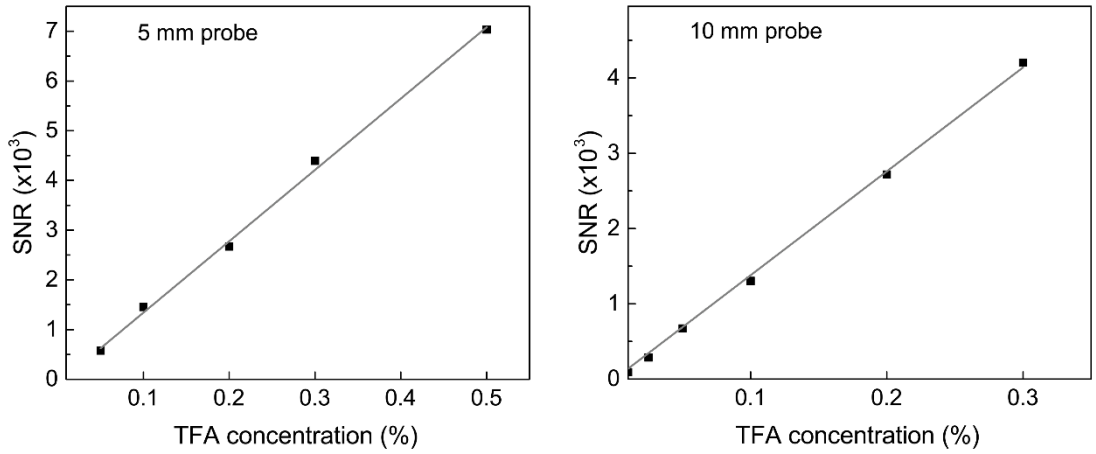

Figure 2.11: Fluorine-19 NMR limit of detection (LOD) estimation. Panels display the signal to noise ratio (SNR) as a function of fluorine concentration in TFA reference for a standard 5 and 10 mm probe (left and right, respectively). After a linear fit, the LOD is defined as the ^{19}F atom count where the extrapolated SNR=2. The results yield a LOD of approximately ~ 10^{14} and ~10^{15} ^{19}F atoms for the 5 and 10 mm probe respectively, corresponding to ~7×10^3 and ~4×10^4 cells assuming typical ^{19}F labeling levels in T cells. All ^{19}F NMR data were acquired on at 376.3 MHz with a 20 min acquisition time and using a 17 μs pulse, 32,000 points of free induction decay (FID), 100 ppm spectral width, 128 averages, and recycle delay of 10 s.

2.4.3. Quantification of apparent cell numbers by NMR

Following the same principle as emulsion concentration and cell uptake determination by ^{19}F NMR, tissue panel necropsies can be harvested from animals receiving labeled CAR T cells and fluorine content determined by NMR. Each tissue is placed in a 5 or 10 mm NMR tube depending on organ size. Blood collected by cardiac puncture can also be measured by NMR. A sealed glass reference capillary containing a mixture of 0.1% (w/v) TFA as well as 0.325 mM $MnCl_2$ is placed beside the organ sample in the NMR tube. $MnCl_2$

enables shortening of the TFA's T_1 relaxation to match that of PFC nanoemulsion (T_1 = 470 ms at 9.4 Tesla) according to the following equation[48]:

$$\frac{1}{T_1} = \frac{1}{T_{1o}} + r_1[MnCl_2]$$

T_1 is the target we want to reduce the spin-lattice relaxation time of TFA to (470 ms at 9,4 Tesla), T_{1o} is the TFA spin-lattice relaxation time at baseline, r_1 is the manganese chloride relaxivity, [$MnCl_2$] is the concentration needed to shorten the T1 to expected value.

After shimming, the ^{19}F NMR spectra were acquired with a 17 μs pulse, 32,000 FID points, 100 ppm spectral width, 32 to 1024 averages(depending on SNR) and a recycle delay of 1.5 s. Phase and baseline corrections were performed to improve measurement accuracy. ^{19}F content of each tissue was determined by calculating the ratio of the PFC peak integrated area to the TFA reference integral and multiplied by the number of fluorine atoms in the reference. The apparent cell number per organ was calculated by dividing the number obtained by the mean ^{19}F/cell of T cells measured after labeling.

2.4.4. In vivo MRI methods

The Molecular Imaging Center at the Sanford consortium (MICS) is equipped with an 11.7 T horizontal (16 cm bore) Bruker Biospec preclinical scanner (Fig.2.12a). All *in vivo* experiments were conducted on that system. Scans were acquired using a 40 mm dual-tuned $^{1}H/^{19}F$ birdcage transmit-receive volume coil (Bruker #T12800V3, Fig 2.12b) or a 20 mm custom-built transmit-receive surface coil (Fig. 2.12c)

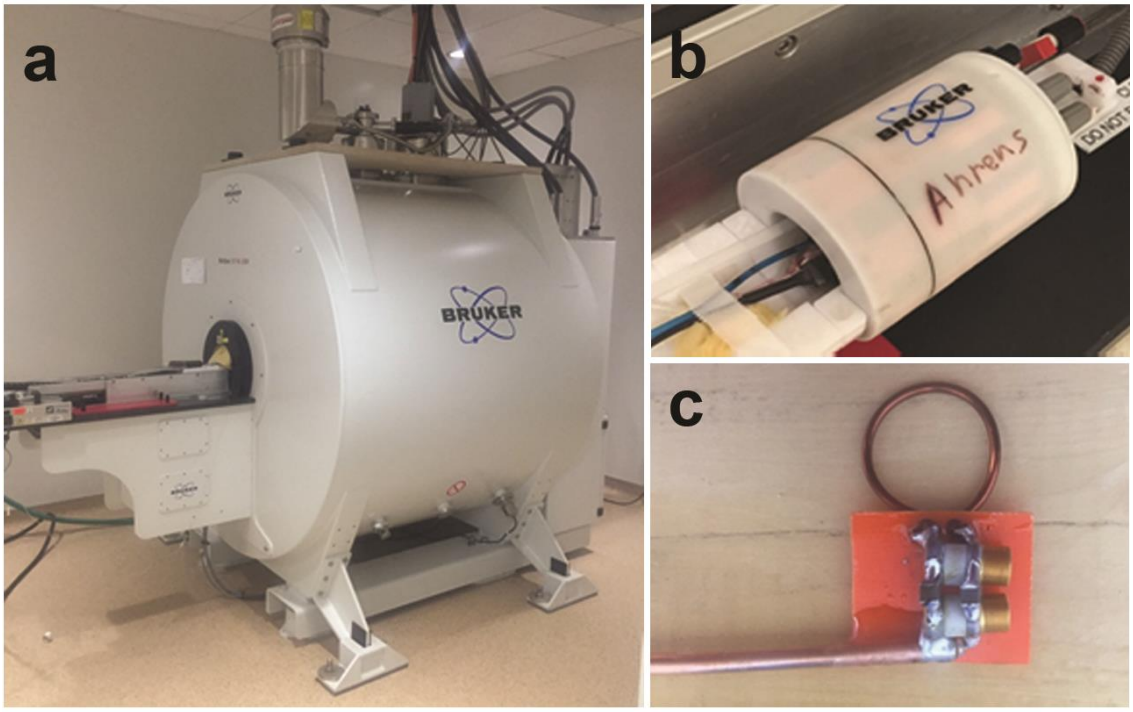

Figure 2.12: MRI system and coils for *in vivo* imaging. (**a**) 11.7 T horizontal (16 cm bore) Bruker Biospec preclinical scanner. (**b**) 40 mm dual-tuned $^{1}H/^{19}F$ birdcage transmit-receive volume coil used for tumor pO2 measurements. (**c**) 20 mm custom-built transmit-receive surface coil used for CAR T cell pO_2 measurements.

When imaging with the volume coil, mice were anesthetized with 2% isoflurane in pure oxygen for no longer than 90 minutes per imaging session. For the surface coil, isoflurane signal impeded accurate image acquisition and R_1 measurements (Fig. 2.13). Therefore, we pursued with injectable anesthesia, first via ketamine/xylazine and metedomidine (0.2mg/ml, 0.01 ml/g) bolus intraperitoneal (IP) injection and maintained by an IP catheter of metedomidine (0.4mg/ml, 0.2ml/h).

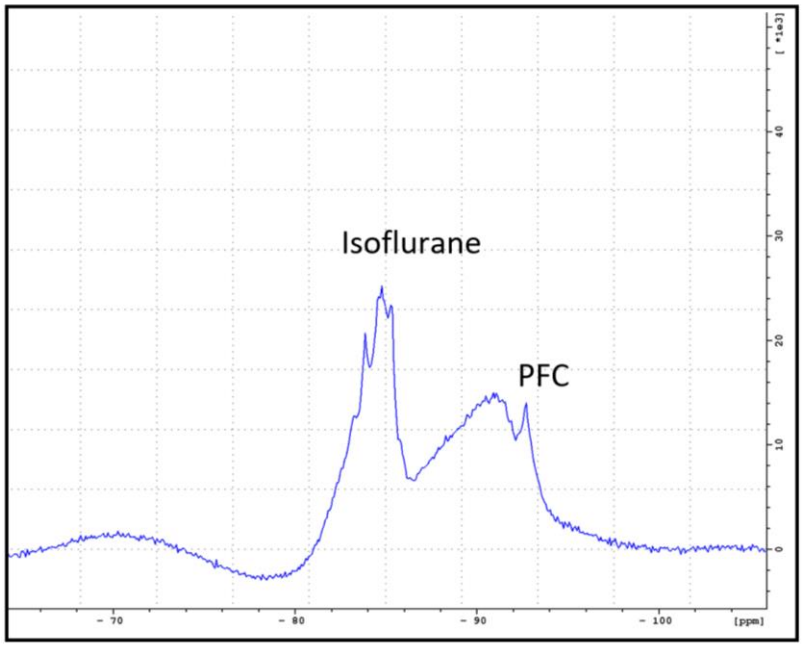

Figure 2.13: Representative spectrum of isoflurane contamination with surface coil. The PFC peak can be seen at -92 ppm but the linewidth of isoflurane (-84 ppm) prevents peak separation.

In the magnet, the animals were placed prone and respiration rate was monitored with a pressure sensor placed below the animal's chest (Fig. 2.14, blue line). Temperature was examined with a rectal probe (Fig. 2.14, black and white cable) and animal core temperature was maintained at 37 °C using a small animal heater reaching inside the bore of the magnet. Acceptable pulse oximetry was confirmed with a mouse paw oximeter sensor (Fig. 2.14, image on the right) when 0.6 l/min continuous oxygen flow was delivered to the animals. Surface coil was tightly screwed right on top of the tumor (Fig. 2.14).

Figure 2.14: Mouse monitoring setup. Mouse is placed prone on a pressure pad (blue line) to monitor respiration. The black and white cable monitors animal temperature. On the right, a sensor is placed on the mouse paw to monitor blood oxygenation. The surface coil is tightly screwed right above the tumor to obtain optimal signal.

RARE (Rapid Acquisition with Relaxation Enhancement) is an enhanced spin echo MR sequence where multiple echoes (number of echoes = rare factor) are used to contribute to the same image. This reduces the imaging time compared to traditional spin echo sequences. Rare factor, repetition time (TR) and number of averages (NA) was optimized to yield highest signal to noise ratio per unit time (SNR/t). Excitation time (TE) was set at the minimum. TR is usually chosen between 1.2 and 3 times the PFC T_1 to maximize signal in minimal time.

PRESS (Point-RESolved Spectroscopy) is a localized (single voxel) spectroscopy method consisting of three slice selective pulses in orthogonal planes. Signal comes from the intersection of the three planes. PRESS provides the highest SNR amongst localized spectroscopy sequences, but results in higher specific absorption rate (energy absorbed by the sample/subject when exposed to the radio frequency). For pO_2 experiments, a voxel encompassing the whole tumor is defined and twelve TR values are used to measure the R_1 relaxation rate, ranging between 0.1 and 6 s.

2.4.5. R1 determination and pO_2 extrapolation

PCE nanoemulsion dissolves oxygen, resulting in a linear increase in the ^{19}F spin-lattice relaxation rate (R_1) with increasing pO_2. A calibration curve was established by subjecting emulsion to different pressures of oxygen. Triplicate emulsion samples were placed in 5 mm NMR tubes and bubbled for 15 min with mixtures of oxygen and nitrogen ranging from 0% to 100%. Tubes were then sealed, placed in the 11.7T MRI instrument, and equilibrated to 37 °C. The R_1 of each individual tube was measured using a PRESS sequence and calculated by integrating the ^{19}F peak acquired at different TR values (Fig. 2.15), and the resulting values are fit using a three-parameter single exponential equation in MNova 6.0.2 software (Mestrelab, Spain). The signal is proportional to the exponential of $-TR \times R_1$. Using the same methodology, PCE-labeled cancer or T cell pO_2 can be determined using the calibration curve (Fig. 2.16) [49, 50].

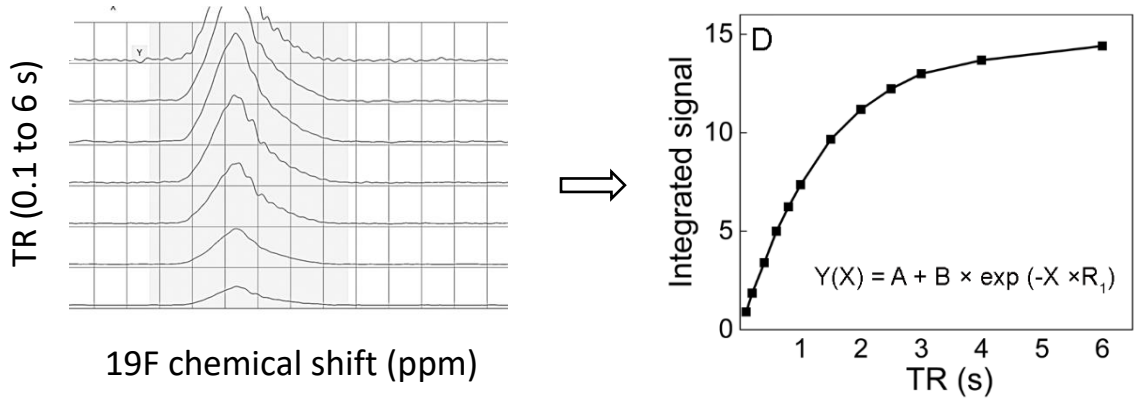

Figure 2.15: Determination of voxel R_1. The signal acquired for each repetition time value is integrated and fitted to a three-parameter single exponential equation, yielding the voxel R_1.

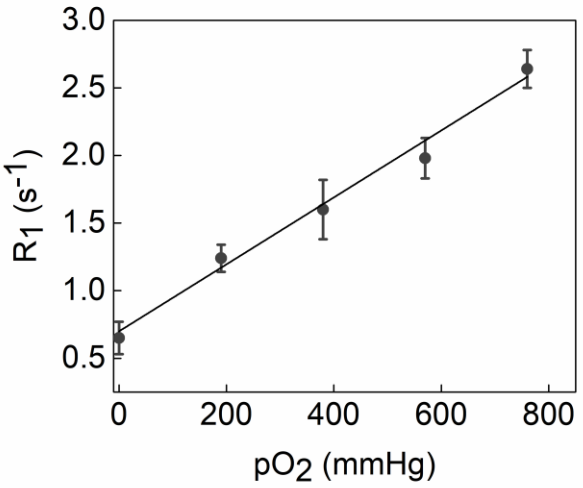

Figure 2.16: *In vitro* calibration curve of R_1 versus pO_2 at 11.7 T and 37 °C. Individual points represent triplicate R_1 measurements of emulsions with different partial oxygen pressures. The solid line represents the resulting linear fit ($R^2 = 0.98$).

2.4.6. Quantification of fluorine atoms from MRI images

Quantification of cell numbers or total fluorine atoms from MRI images follows the same principle as emulsion concentration determination or cell number determination by NMR. In this case, any perfluorocarbon mixture with a known ^{19}F spin concentration can be placed in a reference tube beside the animal. To limit scanning time, PCE or PFPE dilutions are preferred to match the cell labeling agent.

Raw MRI images are loaded in the VoxelTracker™ (Celsense Inc., Pittsburgh, PA) software (Fig. 2.17). Structures including “Reference”, “Noise”, and “Signal” (Fig. 2.17, colored structures) are defined manually by covering the region of interest (ROI). The software algorithm corrects for the Rician-distributed noise present in low-SNR datasets and provides accurate quantification of fluorine atoms in the Signal ROIs[33]. The apparent cell count can be determined from the initial cell loading experiment.

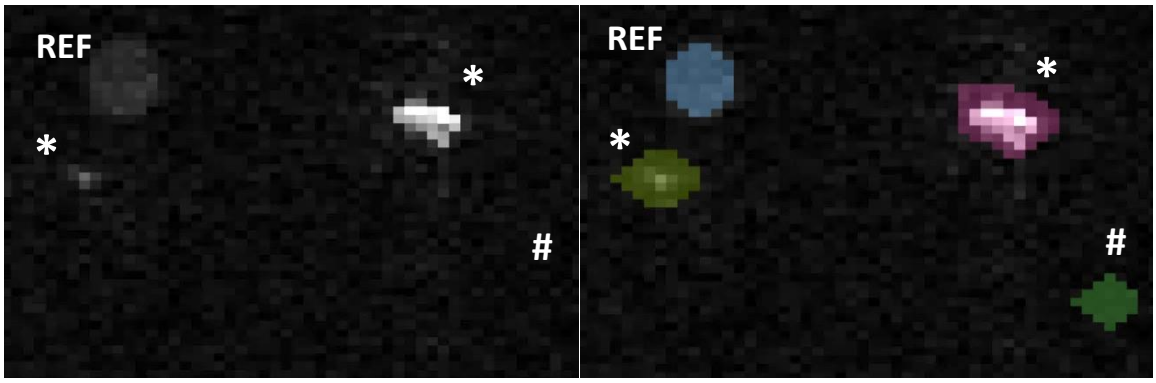

Figure 2.17: Quantification of apparent cell numbers from MRI images. Raw MRI images are loaded in the VoxelTracker software (left panel). Structures including "Reference", "Noise", and "Signal" are defined manually by covering the region of interest (ROI). The blue ROI corresponds to the Reference tube (REF) used for fluorine atoms quantification. The green ROI corresponds to the Noise (#), devoid of signal. The purple and yellow ROIs correspond to two areas with signal to be quantitated (*).

Acknowledgments

Chapter 2, in part, contains text as it appears in two manuscripts: Springer book chapter entitled "Magnetic resonance imaging of immune cell trafficking in response to chemical agents in experimental autoimmune encephalomyelitis", Chapelin F, Ahrens E.T from "Visualizing chemical communication among migratory cells *in vivo*" (2019), and review paper entitled "Fluorine-19 MRI for detection and quantification of immune cell therapy for cancer" Chapelin F, Capitini C, Ahrens E.T, JITC 2018. Chapter 2 also contains figures from supplemental material of published material in the journal Scientific Reports 2017, with revisions and formatting changes for this dissertation. The authors and title of the manuscript are as follows: Chapelin F, Gao S, Okada H, Weber T, Messer K, Ahrens E.T. Fluorine-19 nuclear magnetic resonance of chimeric antigen receptor T cell biodistribution in murine cancer model. Scientific Reports, (2017). Besides this, the content of Chapter 2 is original. The dissertation author was the primary author of these papers.

References

1. Kay, M.A. State-of-the-art gene-based therapies: the road ahead. *Nat Rev Genet* **12**, 316-328 (2011).

2. Ohno, M., Ohkuri, T., Kosaka, A., Tanahashi, K., June, C.H., Natsume, A. & Okada, H. Expression of miR-17-92 enhances anti-tumor activity of T-cells transduced with the anti-EGFRvIII chimeric antigen receptor in mice bearing human GBM xenografts. *Journal for immunotherapy of cancer* **1**, 21 (2013).

3. Janjic, J.M. & Ahrens, E.T. Fluorine-containing nanoemulsions for MRI cell tracking. *Wiley interdisciplinary reviews. Nanomedicine and nanobiotechnology* **1**, 492-501 (2009).

4. Krafft, M.P. Fluorocarbons and fluorinated amphiphiles in drug delivery and biomedical research. *Advanced drug delivery reviews* **47**, 209-228 (2001).

5. Riess, J.G. Understanding the fundamentals of perfluorocarbons and perfluorocarbon emulsions relevant to in vivo oxygen delivery. *Artificial cells, blood substitutes, and immobilization biotechnology* **33**, 47-63 (2005).

6. Partlow, K.C., Chen, J., Brant, J.A., Neubauer, A.M., Meyerrose, T.E., Creer, M.H., Nolta, J.A., Caruthers, S.D., Lanza, G.M. & Wickline, S.A. 19F magnetic resonance imaging for stem/progenitor cell tracking with multiple unique perfluorocarbon nanobeacons. *FASEB journal : official publication of the Federation of American Societies for Experimental Biology* **21**, 1647-1654 (2007).

7. Garrelts, J.C. Fluosol: an oxygen-delivery fluid for use in percutaneous transluminal coronary angioplasty. *DICP : the annals of pharmacotherapy* **24**, 1105-1112 (1990).

8. Ilgiavishute Ia, S., Zhukauskas, G., Dapshis, K.L. & Onishchenko, N.A. [The use of perfluorocarbon emulsions for suppression of rejection reaction in kidney allotransplantation]. *Khirurgiia*, 16-18 (1993).

9. Riess, J.G. Oxygen carriers ("blood substitutes")--raison d'etre, chemistry, and some physiology. *Chemical reviews* **101**, 2797-2920 (2001).

10. Sotak, C.H., Hees, P.S., Huang, H.N., Hung, M.H., Krespan, C.G. & Raynolds, S. A new perfluorocarbon for use in fluorine-19 magnetic resonance imaging and spectroscopy. *Magnetic Resonance in Medicine* **29**, 188-195 (1993).

11. Dardzinski, B.J. & Sotak, C.H. Rapid tissue oxygen tension mapping using 19F inversion-recovery echo- planar imaging of perfluoro-15-crown-5-ether. *Magn Reson Med* **32**, 88-97 (1994).

12. Hees, P.S. & Sotak, C.H. Assessment of changes in murine tumor oxygenation in response to nicotinamide using 19F NMR relaxometry of a perfluorocarbon emulsion. *Magnetic Resonance in Medicine* **29**, 303-310 (1993).

13. Mason, R.P., Antich, P.P., Babcock, E.E., Constantinescu, A., Peschke, P. & Hahn, E.W. Non-invasive determination of tumor oxygen tension and local variation with growth. *Int J Radiat Oncol Biol Phys* **29**, 95-103 (1994).

14. Noth, U., Morrissey, S.P., Deichmann, R., Adolf, H., Schwarzbauer, C., Lutz, J. & Haase, A. In vivo measurement of partial oxygen pressure in large vessels and in the reticuloendothelial system using fast 19F-MRI. *Magn Reson Med* **34**, 738-745 (1995).

15. Balducci, A., Wen, Y., Zhang, Y., Helfer, B.M., Hitchens, T.K., Meng, W.S., Wesa, A.K. & Janjic, J.M. A novel probe for the non-invasive detection of tumor-associated inflammation. *Oncoimmunology* **2**, e23034 (2013).

16. Janjic, J.M., Srinivas, M., Kadayakkara, D.K. & Ahrens, E.T. Self-delivering nanoemulsions for dual fluorine-19 MRI and fluorescence detection. *Journal of the American Chemical Society* **130**, 2832-2841 (2008).

17. Stares, E., Rho, J., Ahrens, E.T., Foster, P., Li, A. & Bartha, R. in Contrast Agents for MRI: Experimental Methods 479-498 (The Royal Society of Chemistry, 2018).

18. Waiczies, H., Lepore, S., Janitzek, N., Hagen, U., Seifert, F., Ittermann, B., Purfurst, B., Pezzutto, A., Paul, F., Niendorf, T. & Waiczies, S. Perfluorocarbon Particle Size Influences Magnetic Resonance Signal and Immunological Properties of Dendritic Cells. *PLoS ONE* **6** (2011).

19. Waiczies, S., Niendorf, T. & Lombardi, G. Labeling of cell therapies: How can we get it right? *Oncoimmunology* **6**, e1345403 (2017).

20. Kabalnov, A.S. & Shchukin, E.D. Ostwald ripening theory: applications to fluorocarbon emulsion stability. *Advances in colloid and interface science* **38**, 69-97 (1992).

21. Maa, Y.F. & Hsu, C.C. Performance of sonication and microfluidization for liquid-liquid emulsification. *Pharmaceutical development and technology* **4**, 233-240 (1999).

22. Varescon, C., Arlen, C., Leblanc, M. & Riess, J.G. An Easy, Convenient Way of Describing the Stability of Fluorocarbon Emulsions. *J Chim Phys Pcb* **86**, 2111-2117 (1989).

23. Lowe, K.C. Engineering blood: synthetic substitutes from fluorinated compounds. *Tissue engineering* **9**, 389-399 (2003).

24. Spahn, D.R. Blood substitutes. Artificial oxygen carriers: perfluorocarbon emulsions. *Crit Care* **3**, R93-97 (1999).

25. Jafari, S.M., He, Y.H. & Bhandari, B. Nano-emulsion production by sonication and microfluidization - A comparison. *Int J Food Prop* **9**, 475-485 (2006).

26. Riess, J.G. Oxygen carriers ("blood substitutes") - Raison d'Etre, chemistry, and some physiology. *Chemical reviews* **101**, 2797-2919 (2001).

27. Taylor, P. Ostwald ripening in emulsions. *Advances in Colloid and Interface Science* **75**, 107-163 (1998).

28. Christian, N.A., Milone, M.C., Ranka, S.S., Li, G.Z., Frail, P.R., Davis, K.P., Bates, F.S., Therien, M.J., Ghoroghchian, P.P., June, C.H. & Hammer, D.A. Tat-functionalized near-infrared emissive polymersomes for dendritic cell labeling. *Bioconjugate Chem* **18**, 31-40 (2007).

29. Nam, Y.S., Park, J.Y., Han, S.H. & Chang, I.S. Intracellular drug delivery using poly(D,L-lactide-co-glycolide) nanoparticles derivatized with a peptide from a transcriptional activator protein of HIV-1. *Biotechnol Lett* **24**, 2093-2098 (2002).

30. Kislukhin, A.A., Xu, H., Adams, S.R., Narsinh, K.H., Tsien, R.Y. & Ahrens, E.T. Paramagnetic fluorinated nanoemulsions for sensitive cellular fluorine-19 magnetic resonance imaging. *Nat Mater* **15**, 662-668 (2016).

31. Walczak, P., Ruiz-Cabello, J., Kedziorek, D.A., Gilad, A.A., Lin, S., Barnett, B., Qin, L., Levitsky, H. & Bulte, J.W. Magnetoelectroporation: improved labeling of neural stem cells and leukocytes for cellular magnetic resonance imaging using a single FDA-approved agent. *Nanomedicine* **2**, 89-94 (2006).

32. Thu, M.S., Bryant, L.H., Coppola, T., Jordan, E.K., Budde, M.D., Lewis, B.K., Chaudhry, A., Ren, J., Varma, N.R., Arbab, A.S. & Frank, J.A. Self-assembling nanocomplexes by combining ferumoxytol, heparin and protamine for cell tracking by magnetic resonance imaging. *Nat Med* **18**, 463-467 (2012).

33. Srinivas, M., Morel, P.A., Ernst, L.A., Laidlaw, D.H. & Ahrens, E.T. Fluorine-19 MRI for visualization and quantification of cell migration in a diabetes model. *Magn Reson Med* **58**, 725-734 (2007).

34. Ruiz-Cabello, J., Walczak, P., Kedziorek, D.A., Chacko, V.P., Schmieder, A.H., Wickline, S.A., Lanza, G.M. & Bulte, J.W. In vivo "hot spot" MR imaging of neural stem cells using fluorinated nanoparticles. *Magn Reson Med* **60**, 1506-1511 (2008).

35. Srinivas, M., Turner, M.S., Janjic, J.M., Morel, P.A., Laidlaw, D.H. & Ahrens, E.T. In vivo cytometry of antigen-specific t cells using 19F MRI. *Magn Reson Med* **62**, 747-753 (2009).

36. Somanchi, S.S., Kennis, B.A., Gopalakrishnan, V., Lee, D.A. & Bankson, J.A. In Vivo (19)F-Magnetic Resonance Imaging of Adoptively Transferred NK Cells. *Methods in molecular biology* **1441**, 317-332 (2016).

37. Bouchlaka, M.N., Ludwig, K.D., Gordon, J.W., Kutz, M.P., Bednarz, B.P., Fain, S.B. & Capitini, C.M. (19)F-MRI for monitoring human NK cells in vivo. *Oncoimmunology* **5**, e1143996 (2016).

38. Bible, E., Dell'Acqua, F., Solanky, B., Balducci, A., Crapo, P.M., Badylak, S.F., Ahrens, E.T. & Modo, M. Non-invasive imaging of transplanted human neural stem cells and ECM scaffold remodeling in the stroke-damaged rat brain by (19)F- and diffusion-MRI. *Biomaterials* **33**, 2858-2871 (2012).

39. Helfer, B.M., Balducci, A., Nelson, A.D., Janjic, J.M., Gil, R.R., Kalinski, P., de Vries, I.J., Ahrens, E.T. & Mailliard, R.B. Functional assessment of human dendritic cells labeled for in vivo (19)F magnetic resonance imaging cell tracking. *Cytotherapy* **12**, 238-250 (2010).

40. Alberts B., J.A., Lewis J., Alberts B., Raff M., Roberts K., Walter P. Lymphocytes and the Cellular Basis of Adaptive Immunity. (Molecular Biology of the Cell. 4th edition, 2002).

41. Chapelin, F., Gao, S., Okada, H., Weber, T.G., Messer, K. & Ahrens, E.T. Fluorine-19 nuclear magnetic resonance of chimeric antigen receptor T cell biodistribution in murine cancer model. *Scientific Reports* **7** (2017).

42. Gonzales, C., Yoshihara, H.A., Dilek, N., Leignadier, J., Irving, M., Mieville, P., Helm, L., Michielin, O. & Schwitter, J. In-Vivo Detection and Tracking of T Cells in Various Organs in a Melanoma Tumor Model by 19F-Fluorine MRS/MRI. *PLoS One* **11**, e0164557 (2016).

43. Ahrens, E.T., Flores, R., Xu, H. & Morel, P.A. In vivo imaging platform for tracking immunotherapeutic cells. *Nature biotechnology* **23**, 983-987 (2005).

44. Hitchens, T.K., Liu, L., Foley, L.M., Simplaceanu, V., Ahrens, E.T. & Ho, C. Combining perfluorocarbon and superparamagnetic iron-oxide cell labeling for improved and expanded applications of cellular MRI. *Magn Reson Med* **73**, 367-375 (2015).

45. Patrick, M.J., Janjic, J.M., Teng, H., O'Hear, M.R., Brown, C.W., Stokum, J.A., Schmidt, B.F., Ahrens, E.T. & Waggoner, A.S. Intracellular pH measurements using perfluorocarbon nanoemulsions. *Journal of the American Chemical Society* **135**, 18445-18457 (2013).

46. Srinivas, M., Boehm-Sturm, P., Figdor, C.G., de Vries, I.J. & Hoehn, M. Labeling cells for in vivo tracking using (19)F MRI. *Biomaterials* **33**, 8830-8840 (2012).

47. Kalos, M. & June, C.H. Adoptive T cell transfer for cancer immunotherapy in the era of synthetic biology. *Immunity* **39**, 49-60 (2013).

48. Nofiele, J.T. & Cheng, H.L.M. Ultrashort Echo Time for Improved Positive-Contrast Manganese-Enhanced MRI of Cancer. *Plos One* **8** (2013).

49. Zhong, J., Sakaki, M., Okada, H. & Ahrens, E.T. In vivo intracellular oxygen dynamics in murine brain glioma and immunotherapeutic response of cytotoxic T cells observed by fluorine-19 magnetic resonance imaging. *PLoS One* **8**, e59479 (2013).

50. Kadayakkara, D.K., Janjic, J.M., Pusateri, L.K., Young, W.B. & Ahrens, E.T. In vivo observation of intracellular oximetry in perfluorocarbon-labeled glioma cells and chemotherapeutic response in the CNS using fluorine-19 MRI. *Magn Reson Med* **64**, 1252-1259 (2010).

Chapter 3: Fluorine-19 nuclear magnetic resonance of chimeric antigen receptor T cell biodistribution in murine cancer model

3.1. Introduction

Immunotherapy, using engineered T cells harboring receptors targeting specific tumor antigens, has opened the path to new treatments for incurable cancers[1]. Cancer cells secrete cytokines that render the host's innate and adaptive immune system 'tolerant' to the tumor, which weakens the intrinsic immunity[2]. In an emerging approach, autologous T cells are genetically modified *ex vivo* to constitutively express a chimeric antigen receptor (CAR) that can help bind T cells to a specific tumor target and overcome tolerance. By delivering high numbers of CAR T cells and stimulating their clonal expansion *in situ*, specific and durable cytotoxicity toward cancer cells has been observed[3]. This strategy has been translated to many types of cancers including leukemia, lymphomas and sarcomas, with custom made receptors for each application[4-6].

Adoptive cell cancer therapy is currently being used in at least 270 active clinical trials worldwide[7]. However, variability in clinical outcomes and the incidence of harmful side effects has challenged researchers to implement methods to validate cell biodistribution and pharmacokinetics in the body[3]. In fact, the United States Food and Drug Administration (FDA) published guidelines[8] specifying that investigational cell therapy should incorporate some means of cell tracking to determine *in vivo* cell survival, anatomic engraftment and biologic activity throughout the product development cycle, preferably starting at the preclinical stage. Indeed, the current gold standard to assess cell biodistribution preclinically involves time-consuming necropsy and histopathological staining of numerous tissue slices,

which, in addition to being tissue-disruptive, only provides quantitative cell information on small tissue 'bites' which is prone to sampling error. Developing a rapid and quantitative preclinical technique for screening new therapeutic cell subtype candidates by assessing cell biodistribution and survival would be highly useful.

Here, we describe the use of nuclear magnetic resonance (NMR) 'cytometry'[9] to assay immunotherapeutic cell biodistribution. This technology employs a perfluorocarbon (PFC) nanoemulsion tracer that labels cells via simple co-incubation in culture prior to *in vivo* delivery. Liquid-state ^{19}F NMR spectroscopy of intact, excised organ and tissue panels is used to measure the effective number of transferred cells within each sample[10-12]. Consequently, the cell biodistribution and survival can be rapidly measured, and specific T cells homing to the tumor and lymphoid organs can be measured, which is presumably predictive of a positive clinical response. We employ a murine model of subcutaneous human glioblastoma treated with CAR T cells expressing Epidermal Growth Factor Receptor variant III (EGFRvIII) transgene[13, 14]. In solid tumors, EGFRvIII is a common tumor-specific variant associated with poor long-term survival[15]. EGFRvIII is present in ~20% of glioblastoma multiforme (GBM) patients; GBM is the most common and aggressive brain cancer[16, 17]. Prior to CAR T cell infusion, the cells are intracellularly tagged with PFC emulsion *in vitro*, and the ^{19}F labeling efficiency, cellular function, and phenotype is verified post-labeling. Following infusion, CAR T cell efficacy is monitored by bioluminescence imaging (BLI) *in vivo,* and CAR T cell biodistribution and pharmacokinetics are quantitated using *ex vivo* ^{19}F NMR. Overall, NMR cytometry may accelerate the timeline to evaluate and screen new engineered cell therapeutic candidates.

3.2. Methods

3.2.1. Chimeric antigen receptor (CAR) lentiviral vector

We employed a vector for CAR consisting of a side chain fragment variable (scFv) specific to EGFR-vIII fused to a CD8α hinge with 4-1BB, CD28 and CD3z intracellular domains as described by Ohno *et al*.[18]. With this construct, lentivirus was produced using ten million human embryonic kidney (HEK) 293T cells (ATCC, Manassas, VA) that were plated in a 175 cm^2 flask with 9 ml of OptiMEM (Gibco) media. The psPAX2, pMD2.G and pELNS-3C10CD28-41BBz plasmids were added to the flask with 120 µl of Lipofectamine (Invitrogen, Carlsbad, CA) as described elsewhere[18]. After 24 hours, the supernatant was harvested and centrifuged at 16,000 rpm for 2 hours at 4 °C. The viral pellet was resuspended in 100 µl of phosphate buffered saline (PBS) and used immediately to transduce human T cells (described below).

3.2.2. Human T cell isolation

Peripheral blood mononuclear cells (PBMCs) were isolated from anonymous donor human blood (San Diego Blood Bank, San Diego, CA) by Ficoll (Histopaque 1077, Sigma Aldrich, St Louis, MO) gradient density centrifugation. T cell enrichment from PBMCs was performed by Pan T cell magnetic cell sorting (Miltenyi Biotech Inc., Auburn, CA). Cell phenotype was confirmed by flow cytometry (LSR Fortessa, BD Biosciences, San Diego, CA) using FITC anti-human CD3 antibody (Biolegend, San Diego, CA). T cells were expanded for two days in Roswell Park Memorial Institute (RPMI) media (Gibco) supplemented with 10% Fetal Bovine Serum (FBS) and 100 units/ml of recombinant human

Intereukin 2 (IL-2, Peprotech, Rocky Hill, NJ) while being activated with dynabeads harboring human T cell CD3/CD28 (Gibco).

3.2.3. CAR transduction and PFC labeling

The T cells were added to 6-well plates at a density of 1×10^6 cells per well and transduced with CAR lentivirus; 30 μl of virus in PBS was added to each well along with 6 μg/ml Polybrene transfection agent (EMD Millipore, Billerica, MA). The T cell transduction efficacy was determined by flow cytometry at 5 and 14 days after virus addition using a primary biotin-SP-AffiniPure F(ab')2 fragment-specific goat anti-mouse antibody (Jackson Immuno Research Laboratories, West Grove, PA) and streptavidin-PE served as the secondary antibody (BD Pharmingen, San Diego, CA).

To label T cells for NMR cytometry, CAR T cells and untransduced T cells (control) were plated at a density of 10 million cells in 5 ml of RPMI in 6-well plates and incubated for 12 h with 10 mg/ml of PFC nanoemulsion (CS-1000 or CS-ATM DM Red, Celsense, Inc., Pittsburgh, PA). Subsequently, labeled cell aliquots were assayed for viability via the Trypan blue assay, as well as CD4/CD8 phenotype by flow cytometry using PE/Cy5 anti-human CD4 clone OKT4 and Alexa 488 anti-human CD8 clone SK1 (Biolegend). In these assays, T cells minus PFC label, with and without CAR transgene, were evaluated alongside as controls.

To quantitatively assay PFC cell uptake, triplicates of 1.5 million cells were resuspended in 150 μl PBS with 0.5% Triton X-100 (Sigma Aldrich) and transferred to a 5 mm NMR tube. Also, a 50 μl solution of 0.1% sodium trifluoroacetate (TFA, Sigma Aldrich)

in D_2O (Acros Organics, Geel, Belgium) was added to each tube and vortexed. ^{19}F NMR spectra were acquired for each sample using a 400 MHz (9.4 Tesla) Bruker AVANCE III HD-NanoBay spectrometer (Bruker, Inc., Billerica, MA) with: 17 μs pulse, 32,000 FID points, 100 ppm spectral width, 32 averages, and a recycle delay of 5 s. Two peaks were observed, with the TFA reference and PFC peaks at -76 ppm and -91.58 ppm, respectively. The ^{19}F content of each sample was determined by calculating the ratio of the PFC peak integrated area to the reference integral multiplied by the number of fluorine atoms in the TFA aliquot. The mean ^{19}F/cell was calculated from the ^{19}F content divided by the cell count in the sample.

3.2.4. Flow cytometry assays

CD4/CD8 phenotype and viability was also validated by flow cytometry using PE/Cy5 anti-human CD4 clone OKT4, Alexa 488 anti-human CD8 clone SK1 and 7-AAD viability marker (Biolegend). In these assays, T cells minus PFC label, with and without CAR transgene, were evaluated alongside as controls. Persistence of dual-mode PFC (CS-ATM-DM-Red) label in CAR T cells was assessed by flow cytometry over 14 days after wash.

3.2.5. Confocal microscopy

Aliquots of CAR T cells (N=6, 1 million cells) labeled with dual-mode PFC emulsion or unlabeled were harvested one day post-labeling, fixed with 4% paraformaldehyde (Affimetrix Inc., Cleveland, OH) for 10 min and stained with CD3-FITC as above and

Hoechst dye nuclear stain (#33342, 1:500 dilution, Thermo Fisher Scientific). Cells were mounted in media (Lerner Laboratories, Cheshire, WA) and slides were imaged using a confocal Leica DM 6000 CFS microscope with a ×63 immersion objective

To quantitatively assay PFC cell uptake, triplicates of 1.5 million cells were resuspended in 150 μl PBS with 0.5% Triton X-100 (Sigma Aldrich) and transferred to a 5 mm NMR tube. Also, a 50 μl solution of 0.1% sodium trifluoroacetate (TFA, Sigma Aldrich) in D_2O (Acros Organics, Geel, Belgium) was added to each tube and vortexed. ^{19}F NMR spectra were acquired for each sample using a 400 MHz (9.4 Tesla) Bruker AVANCE III HD-NanoBay spectrometer (Bruker, Inc., Billerica, MA) with: 17 μs pulse, 32,000 FID points, 100 ppm spectral width, 32 averages, and a recycle delay of 5 s. Two peaks were observed, with the TFA reference and PFC peaks at -76 ppm and -91.58 ppm, respectively. The ^{19}F content of each sample was determined by calculating the ratio of the PFC peak integrated area to the reference integral multiplied by the number of fluorine atoms in the TFA aliquot. The mean ^{19}F/cell was calculated from the ^{19}F content divided by the cell count in the sample.

3.2.6. Electron microscopy

We examined CAR T cells labeled with PFC nanoemulsion by electron microscopy. Pelleted cells were fixed in PBS containing 2% glutaraldehyde in 0.1M sodium cacodylate (SC) buffer at room temperature for 30 min and held overnight at 4°C. The cells were washed five times in 0.1M SC buffer on ice and treated with 1% OsO4 in 0.1M SC buffer for 1 hour. All of the samples were washed in dH2O and treated with 2% uranyl acetate for 1 hour on

ice. Pellets were then dehydrated in an ascending series of ethanol and finally 2× dry acetone at room temperature. The cells were infiltrated overnight in a solution containing a 1:1 mixture of dry acetone and Durcupan for 2 hours on a rotator and in 100% Durcupan overnight. The next day, the mixture was replaced with 100% Durpucan twice, and pellets were embedded in Durpucan and incubated in an oven for 36-48 hours. Ultra-thin (60 nm) sections were cut using a diamond knife and collected on mesh Cu grids. The samples were stained with 1% aqueous uranyl acetate and Reynolds lead citrate. Sections were imaged using a Tecnai Spirit electron microscope at 80KV (FEI company).

3.2.7. Glioblastoma cells

Frozen U87-EGFRvIII-Luc glioblastoma cells[18] overexpressing EGFRvIII, as well as the luciferase gene, were thawed and maintained in RPMI media containing 10% FBS and 1% penicillin/streptomycin (Gibco) in T75 flasks (Sigma).

3.2.8. In vitro T cell cytotoxicity assay

U87-EGFRvIII-Luc cells were plated at a density of 30,000 cells per well (18 wells total) in clear bottom 96-well plates (Corning, Inc., Corning, NY) and were allowed to adhere. Wells (n=6, per condition) received: (i) 5:1 ratio of CAR T cells to cancer cells, (ii) 5:1 ratio of untransduced T cells to cancer cells, or (iii) cancer cells alone to calculate baseline viability. After adding D-luciferin (300 μg/ml) to each well, bioluminescence signals were measured with a Tecan plate reader (Infinite M200PRO, Morrisville, NC) at 6, 12, and 24 hours post T cell addition. The relative glioma cell cytotoxicity was obtained

from the mean photon count for groups (i-iii), and the ratio of treated versus untreated means are displayed as percentages.

3.2.9. Murine model of subcutaneous glioblastoma

Animal protocols were approved by the University of California San Diego Institutional Animal Care and Use Committee (IACUC). *In vivo* studies were performed to confirm anti-cancer efficacy of PFC-labeled CAR T cells. Female (n=45) SCID mice 6-8 weeks of age (Jackson Laboratories, Bar Harbor, ME) received bilateral sub-cutaneous flank injections, each containing 5×10^6 U87-EGFRvIII-Luc cells in buffered 50% Matrigel (Corning, Tewksbury, MA). Once tumors were established (~4 mm size), mice were divided into 3 groups (n=15 per group), with Group 1 receiving 20×10^6 PFC labeled CAR T cells intravenously (IV) via tail vein, Group 2 receiving the same number of PFC-labeled untransduced T cells IV, and Group 3 was untreated. For histology purposes, one additional animal in Groups 1-2 received T cells labeled with a fluorescent dye-conjugated PFC nanoemulsion (CS-ATM DM Red, ex/em 596/615, Celsense Inc.), to enable histological validation of colocalization of imaging agent and transferred labeled T cells.

3.2.10. In vivo bioluminescence imaging (BLI)

All mice underwent serial BLI using an IVIS Spectrum (Perkin Elmer, Waltham, MA) at day 0, 3, 7, 10 and 14 after receiving T cells. Prior to BLI, mice received 150 mg/kg of D-Luciferin (Intrace Medical, Lauzanne, Switzerland) intraperitoneally, and images were acquired 10 to 15 min after injection to measure total flux. A white-light body surface image

was collected with a field of view to fit five mice, followed by an image of the spatial distribution of photon counts rendered in pseudo-color, which was overlaid onto the surface image. Quantitative analysis of the radiance flux (photons/s) was performed with the Living Image Software (Perkin Elmer, Waltham, MA) by defining identical regions of interest covering the tumor area. Following BLI, tumor sizes were measured using a caliper.

3.2.11. Ex vivo ^{19}F NMR

In each animal group, five mice were euthanized at days 2, 7 or 14 after treatment infusion to evaluate cell biodistribution. Mice were sacrificed by CO_2 inhalation, and intact tissues of interest (brain, thymus, heart, lungs, liver, spleen, tumors, lymph nodes, kidneys, small intestine, spinal cord, femur, tail and blood) were harvested. All organs were fixed in 4% paraformaldehyde (Affimetrix Inc., Cleveland, OH) overnight, rinsed in PBS and weighed before transfer to either 5 or 10 mm glass NMR tubes (Wilman Labglass, Vineland, NJ), depending on organ size. Importantly, the specimen size fit entirely within the manufacturer-specified receptive field of the NMR detector coil, which spanned ~2 cm length from the bottom of the NMR tube, thereby ensuring that all ^{19}F nuclei in the sample are detected. Also, a sealed glass reference capillary (Kimble Kontes, Vineland, NJ) containing a mixture of 0.1% (w/v) TFA, as well as 0.325 mM $MnCl_2$ to shorten the TFA's ^{19}F T_1 relaxation to match that of the PFC nanoemulsion (T_1~470 ms at 9.4 Tesla)[19], was placed inside the NMR tube with the sample. All samples were first measured individually, and for organs/tissues with very low ^{19}F signal, multiple specimens were pooled into a single NMR tube to boost sensitivity. After shimming, the ^{19}F NMR spectra were acquired using a 400 MHz spectrometer with: 17 μs pulse, 32,000 FID points, 100 ppm spectral width, 32 to

1024 averages (depending on SNR), and a recycle delay of 1.5 s. Phase and baseline corrections were performed to improve measurement accuracy. The ^{19}F content of each tissue sample was determined by calculating the ratio of the PFC peak (-91.58 ppm) integrated area to the TFA reference (-76 ppm) integral, multiplied by the number of fluorine atoms in the reference. The apparent cell number per tissue sample was calculated by dividing the ^{19}F content of each tissue sample by the mean ^{19}F/cell of T cells measured after labeling (above).

3.2.12. Histological analyses

In the one animal per experimental group receiving fluorescent PFC nanoemulsion (CS-ATM DM Red, Celsense) spleens, tumors and livers were embedded in optimal cutting temperature (OCT) compound (Sakura Finetek USA, Inc., Torrance, CA) and stored at -80 °C. All tissues were cryosectioned (CM1950, Leica Microsystems Inc., Buffalo Grove, IL) at 10 μm thickness. Sections were fixed with 4% paraformaldehyde, stained for T cells using FITC anti-human CD3 (UCHT1, 1:500 dilution, Biolegend) and for nuclei using Hoechst dye (#33342, 1:500 dilution, Thermo Fisher Scientific) and then mounted. Liver sections were stained for macrophages with an Alexa 488 anti-mouse F4/80 antibody (BM8, 1:200 dilution, Biolegend)[20]. Fluorescence images were acquired on an Axiovert 40 CFL microscope (Zeiss, Thornwood, NY) using a ×5 objective. Confocal images were acquired on a Leica SP5 2 confocal system with a Leica DM 6000 CFS microscope and a ×63 immersion objective. For direct cell counts in tumor, we used sections (two per tumor) stained against CD3 from five tumors total, three from day 2 and one each from days 7 and

14. We counted T cells in six high power fields per slice (×20 magnification, 120 high power fields total).

3.2.13. Statistical analyses

Generally, measurements are presented as mean ± standard error. A one-way ANOVA along with unpaired T-tests with unequal variances were performed to compare groups as a whole and by pairs, respectively, for bioluminescence and tumor volume measurements. For ANOVAs, we used the Bonferroni correction for multiple comparisons, thereby controlling the family-wise error rate at 5%. Unpaired T-tests were used to compare the apparent cell numbers between groups. P-values <0.05 are considered statistically significant. ANOVA results are expressed as an F-statistic and its associated degrees of freedom and P-value. For pooled samples (thymus and lymph nodes), an estimate of the NMR measurement error is displayed, which was calculated from the standard error of the baseline noise signal over the same integral interval width used to measure the ^{19}F tissue peak. Average ^{19}F NMR signal in tumors was correlated with the number of CAR or untransduced T cells count by histopathology using a Pearson's correlation coefficient test.

3.3. Results

3.3.1. In vitro characterization of CAR-expressing T cells

Initially, we assessed the phenotype and PFC labeling levels in T cells. The lymphocyte isolation from PBMC yields a pure population of CD3+ T cells with an approximate 2/3 CD4+ and 1/3 CD8+ phenotype distribution (Fig. 3.1a and b). In T cells transduced with lentivirus harboring EGFRvIII antibody, transgene expression levels persist,

with >70% of the human T cells expressing the CAR receptor after two weeks *in vitro* (Fig. 3.1c). For *in vivo* animal studies (below), infused T cells were 85±10% CAR-positive.

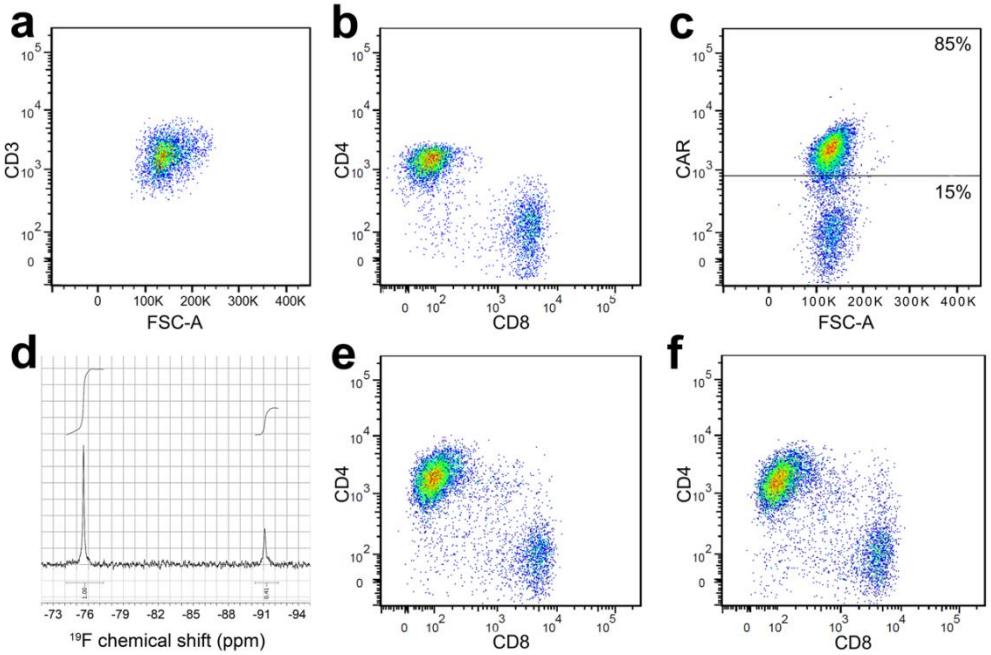

Figure 3.1: CAR T cell transduction and characterization. (**a)** Scatter plot showing the pure population of human T cells (CD3) after magnetic assisted cell sorting of blood samples. (**b**) Isolated T cell flow analysis for expression of CD4/CD8 shows that 2/3 of T cells are CD4+ and 1/3 are CD8+. (**c**) CAR T cell population 2 weeks after transduction shows 85% CAR-expressing T cells. (**d**) ^{19}F NMR spectrum showing PFC uptake of CAR T cells (peak at -91 ppm, 2×10^{11} atoms/cells) normalized to the TFA reference (peak at -76 ppm). (**e**) Flow cytometry histogram showing similar repartition of CD4+ and CD8+ CAR T cells after transduction compared to untransduced T cells (**b**). (**f**) CAR T cells labeled with PFC *ex vivo* exhibit comparable phenotype to unlabeled cells.

Labeling experiments with PFC nanoemulsions at 10 mg/ml over a period of 12 hours co-incubation display minimal viability impairment as assessed by Trypan blue exclusion test (Average 95±1%, N=3 replicates) and flow cytometry viability measurements ($p>0.05$). These conditions yield an average labeling efficiency of $2\pm0.5\times10^{11}$ atoms of fluorine per cell (N=3 replicates, Fig. 3.1d), as determined by ^{19}F NMR. Moreover, PFC labeling does

not appear to alter T cell phenotype as defined by CD4+ and CD8+ expression (Fig. 3.1e and f, $p>0.05$).

Intracellular and perinuclear localization of PFC label in CAR T cells was confirmed by confocal microscopy (Fig.3.2a-b) using a dual-mode MRI-fluorescent PFC nanoemulsion. This result was corroborated by electron microscopy (Fig. 3.2c-d). Bright spheroids corresponding to electron-sparse scattering perfluorocarbon droplets were found in most labeled cells (Fig.3.2c, see inset, ×11,000) but not in control unlabeled cells (Fig 3.2d). Flow cytometry (Fig. 3.2e-f) measurement of CAR T cells labeled with the dual mode agent revealed a shift in red fluorescence compared to control unlabeled cells indicating that essentially 100% of CAR T cells are labeled with PFC one day after labeling (Fig. 3.2e). The fluorescence shift remains discernable for several days after labeling but returns to unlabeled baseline by day 14 due to cell division and agent dilution; the degree rate of label dilution is consistent with the CAR T cell division rate *in vitro*.

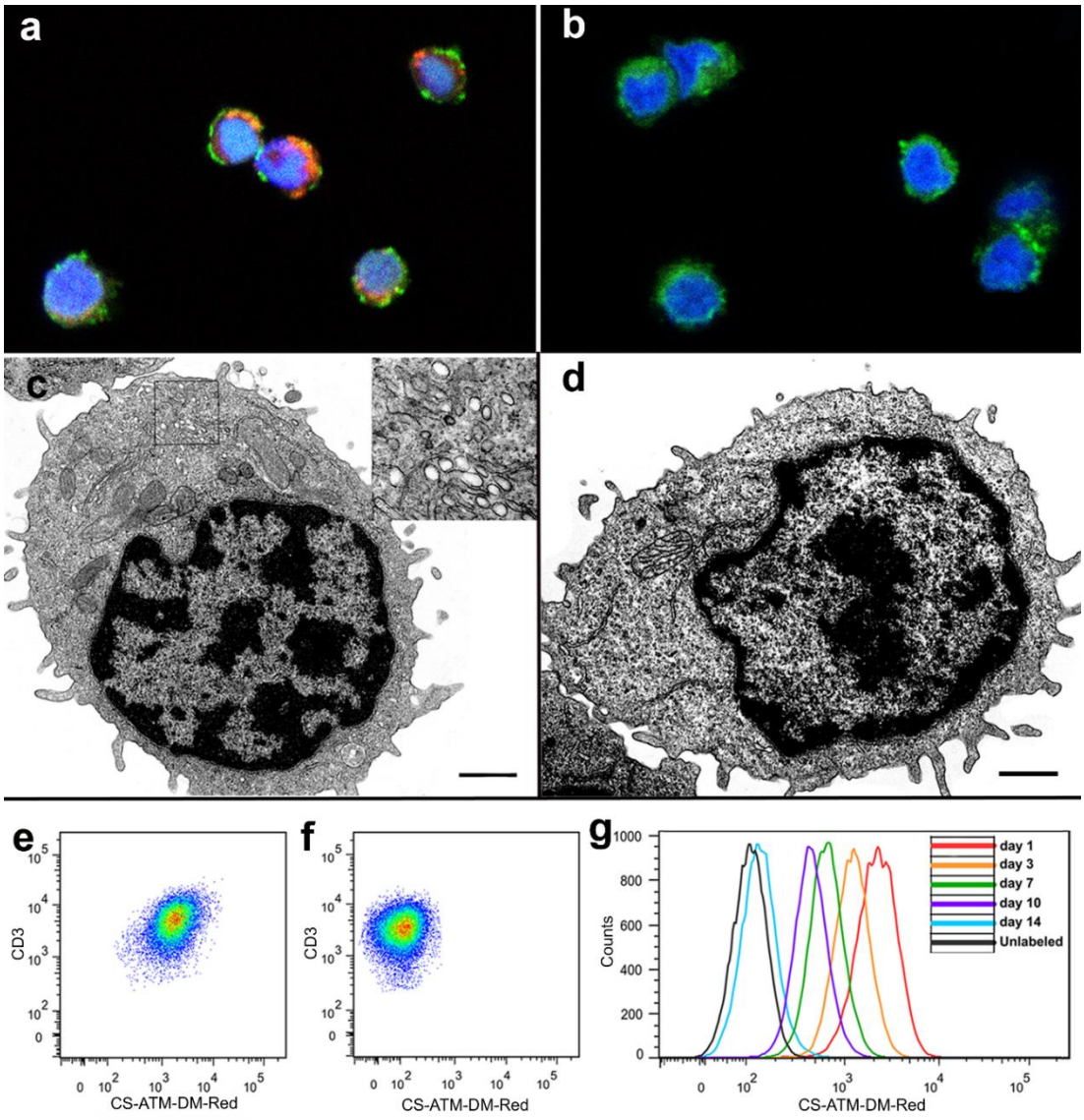

Figure 3.2. Confirmation of intracellular localization of PFC. (**a**) Confocal image (×63) showing perinuclear localization of dual-mode PFC nanoemulsion (in red) in CAR T cells. Nucleus is stained in blue and cell membrane in green via CD3-FITC (**b**) Control unlabeled CAR T cells do not exhibit red fluorescence. (**c**) Electron microscopy (EM) micrograph of ultra-thin PFC-labeled CAR T cells reveals the presence of bright vesicles (inset = ×11,000) corresponding to internalized PFC droplets. (**d**) In control unlabeled cells, no PFC vesicles are found (× 4800, scale bars = 1 μm). (**e**) Flow cytometry scatter plot showing the resulting shift in red fluorescence of CAR T cells after labeling. All cells are labeled after overnight incubation as evidenced by fluorescence gap between labeled (**e**) and unlabeled (**f**) CAR T cells. (**g**) Longitudinal red fluorescence measurement after labeling shows persistent signal and consistent decrease of fluorescence intensity due to cell division.

3.3.2. CAR T cells exhibit cytotoxicity against U87-EGFRvIII glioma cells

CAR T cells exhibit significant, antigen specific, cytotoxic activity against U87-EGFRvIII-Luc cells *in vitro* (Fig. 3.3). Ultraviolet-visible (UV-Vis) spectroscopy measurements show that CAR T cells induce 93% tumor cell death compared to 53% for untransduced T cells at 24 h (Fig. 3.3). These results are statistically significant at all time points ($p<0.0001$). Untransduced T cells generated notable non-specific tumor cell death, but apoptosis induction plateaued rapidly to 50%. Pro-inflammatory cytokines present in the media, including IL-2 and CD3/CD28 beads, may have contributed to untransduced T cell activation, leading to granzyme and perforin release and detectable cancer cell death[21]. Nonetheless, these *in vitro* results confirmed the targeted cytotoxic activity of CAR T cells against EGFRvIII+ glioma cells.

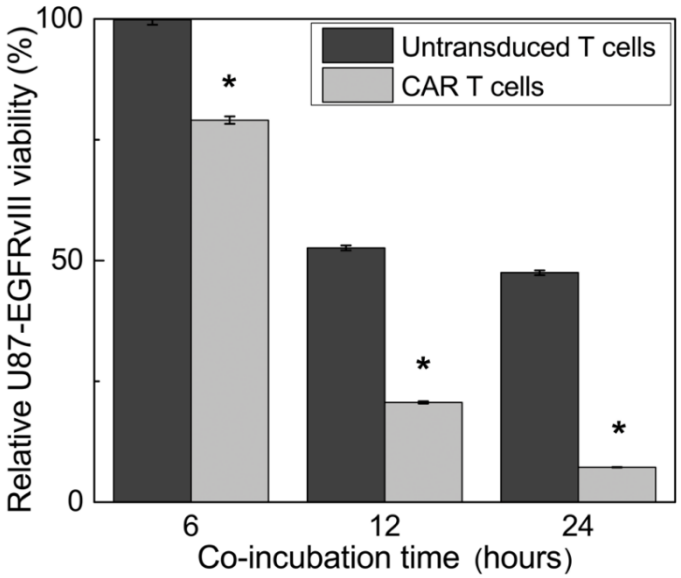

Figure 3.3: Human CAR T cell cytotoxicity assay *in vitro*. Co-incubation of CAR T cells or untransduced T cells with human U87-EGFRvIII-Luc glioma cells resulted in significant cell death at 6, 12 and 24 h. The CAR T cells exhibit significant tumor killing ability (93%) compared to untransduced T cells (53%, $p<0.0001$ indicated by *). The relative glioma cell cytotoxicity was obtained from the mean photon count, and the ratio of treated versus untreated means are displayed as percentages.

3.3.3. CAR T cells inhibit tumor growth

The anti-tumor efficacy of PFC-labeled CAR T cells was verified using immunocompromised SCID mice bearing bilateral subcutaneous U87-EGFRvIII tumors. Engraftment of tumors was confirmed by BLI and caliper measurements just prior to T cell infusion (day 0). Longitudinal BLI and tumor measurements show considerably reduced tumor growth as early as 7 days after CAR treatment (Fig. 3.4a) compared to controls. The radiance of CAR-treated tumors average $2.9\pm0.4\times10^{10}$ photons/s, which was three times lower than the luminescence for both the T cell treated ($1.06\pm0.1\times10^{11}$ photons/s) and untreated ($1.01\pm0.1\times10^{11}$ photons/s) groups (Fig. 3.4b, F-statistic $F(2,29)=18.06$, $p<0.0003$). Similarly, the mean tumor volume at day 7 in the CAR-treated group is 226 ± 28 mm^3, compared to 497 ± 50 mm^3 and 502 ± 41 mm^3 for untransduced T cells and untreated groups, respectively (Fig. 3.4c, $p<0.003$). The disparity among groups grew until the last measurement on day 14, where the mean luminescence in the CAR-treated group is $2.33\pm0.3\times10^{11}$ photons/s, and the untransduced T cell and untreated groups is $9.08\pm0.6\times10^{11}$ and $8.21\pm0.8\times10^{11}$ photons/s, respectively. The T-test p-value between CAR treated and untransduced T cell treated or untreated is ≤0.0001; the corresponding ANOVA test of the three groups $F(2,29)=18.06$-37.29, $p<0.0003$ is extremely significant at 7, 10 and 14 days post-treatment, using a Bonferroni correction.

The cancer cells in a solid tumor, in particular in the necrotic center, are much less accessible to the T cell pool compared to the *in vitro* case where the cancer cells are directly in contact with T cells. In fact, cell quantitation shows that the number of cells reaching the tumor *in vivo* is fairly low, and this is one of the plausible explanations as to why the CAR T cells fail to completely ‘reverse’ tumor growth (Fig. 3.4).

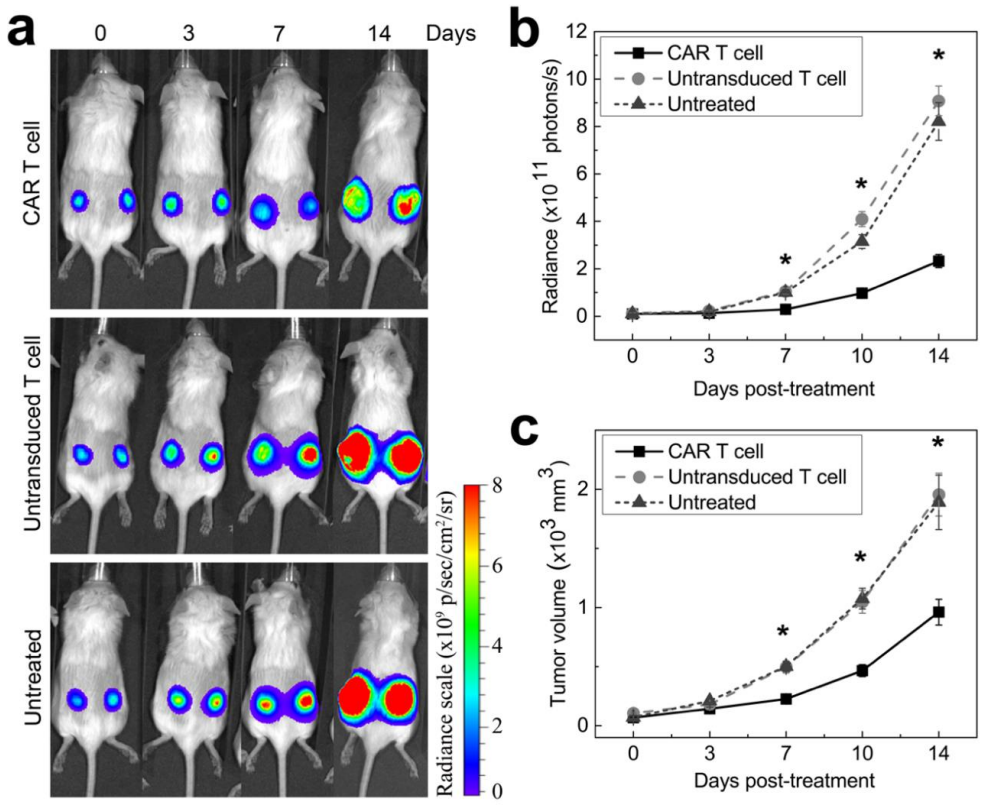

Figure 3.4: Impact of cell therapy on tumor growth *in vivo*. (**a**) Representative bioluminescence images at day 0, 3, 7, 10 and 14 after cell therapy for all three groups show tumor growth reduction for the CAR T cell treated mice compared to untransduced T cell treated or untreated mice. (**b**) Bioluminescence signal is significantly lower in the CAR T cell treated group starting at day 7 compared to controls. CAR T cell treated animals display a radiance four times lower than untransduced T cell treated animals or untreated animals at day 14 (* indicates $p<0.0003$ at day 7,10 and 14). (**c**) Corresponding tumor volume measurements show 50% reduction in tumor growth for the CAR T cell treated group at day 7, 10 and 14 (* indicates $p<0.0003$) and no significant difference between untransduced T cell treated and untreated groups ($p=0.38$). ^{19}F NMR cytometry of T cell biodistribution

NMR measurements on intact tissue samples enable quantification of the total ^{19}F content and the apparent number of labeled T cells infiltrating the tissue (Fig. 3.5). The results at day 2 post-treatment show greater CAR T cell homing to the tumors and spleen compared to untransduced T cells ($p=0.01$ and 0.04, respectively). Approximately 85,000±14,000 CAR-T cells are found in the tumors at day 2. The number of apparent CAR T cells in the tumor is stable until day 7, whereas untransduced T cells are below the LOD,

which is estimated to be on the order of ~7×10^3 cells per sample for the 5 mm probe and ~4×10^4 for the 10 mm probe (see Fig. 2.10). On average, $5\pm0.7\times10^5$ CAR T cells (*i.e.*, the equivalent amount of ^{19}F signal) is found in the spleen at day 2 and 14, whereas only half this amount is observed in untransduced T cell treated animals. These NMR cytometry measurements do not account for possible T cell division *in vivo*; cell division can diminish the accuracy of the apparent total cell count per tissue, particularly at later time points.

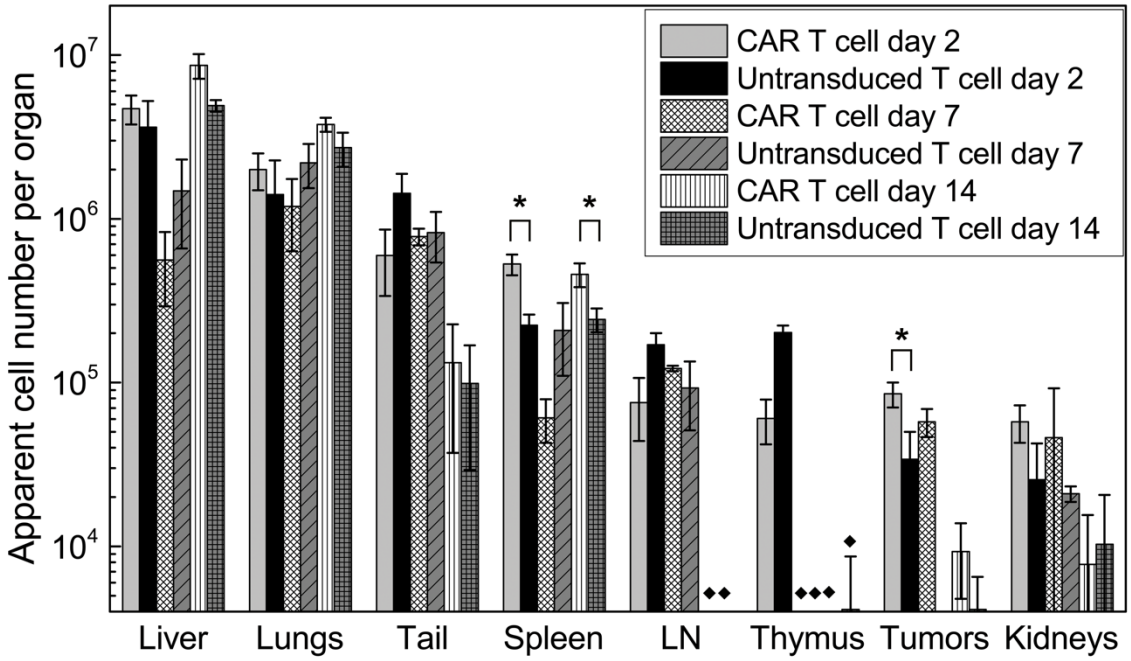

Figure 3.5: Biodistribution of tissue samples by ^{19}F NMR at 2, 7 and 14 days post-treatment. ^{19}F NMR measurements of organ biodistribution of the PFC-labeled cells show greater CAR T cell homing to the spleen and tumors compared to untransduced T cells at day 2. The liver signal likely represents the dead T cell fraction. These measurements do not account for cell division, thus referred to as 'apparent' cell number. LN indicates lymph nodes, (*) indicate significance, and (♦) indicate pooled samples.

The average ^{19}F signal in the liver is approximately 15% of the injected dose at day 2 in both groups. At day 14, 33% of the fluorine signal is found in the liver. The liver ^{19}F signal (Fig. 3.5) presumably represents the dead T cell fraction, as PFC droplets from dead cells

are taken up predominantly by Kupffer cells of the liver[22]. No significant differences are found in the lymph node signals between groups (Fig. 3.5). The tail ^{19}F signal (Fig. 3.5) represents the fraction of cells that are 'mis-injected' during tail vein delivery and presumably resides in local subcutaneous tissue; using this measured value one can in principle calculate the actual T cell dose delivered intravenously in each subject by subtracting out this missed cell fraction. All measurements presented are above our LOD of ~7×10^3 to ~4×10^4 cells per sample (for 5 mm and 10 mm probes, respectively) for a 20 min acquisition time (see Fig. 2.10). Organs with undetectable fluorine levels in all animals are not displayed (brain, heart, small intestine, spinal cord, femur, blood). In the recovered blood samples, the ^{19}F NMR displayed signal below the LOD, thus residual blood in tissue samples would not be a significant source of false-positive signal.

3.3.4. Histopathology

Histopathological staining confirms the presence of numerous CAR T cell infiltrates in the tumors as evident by the fluorescent green signal targeting human CD3 (Fig. 3.6a). In comparison, untransduced T cell infiltrates are sparser in these tissues (Fig. 3.6b). At day 2, both CAR-T cells and untransduced T cells show persisting red fluorescent signal corresponding to the dual-mode (CS-ATM DM Red) PFC nanoemulsion (Fig. 3.6c-d). No endogenous T cells are present in untreated SCID mice (Fig. 3.6e). Quantitative analysis of the number of CAR or untransduced T cells per high power field show significantly higher CAR T cell numbers in the tumor tissue than untransduced T cells at all time points (Fig. 3.6f). In addition, histology counts strongly correlate to the average NMR fluorine signal measured in tumors (Pearson's r = 0.89, Fig 3.6g).

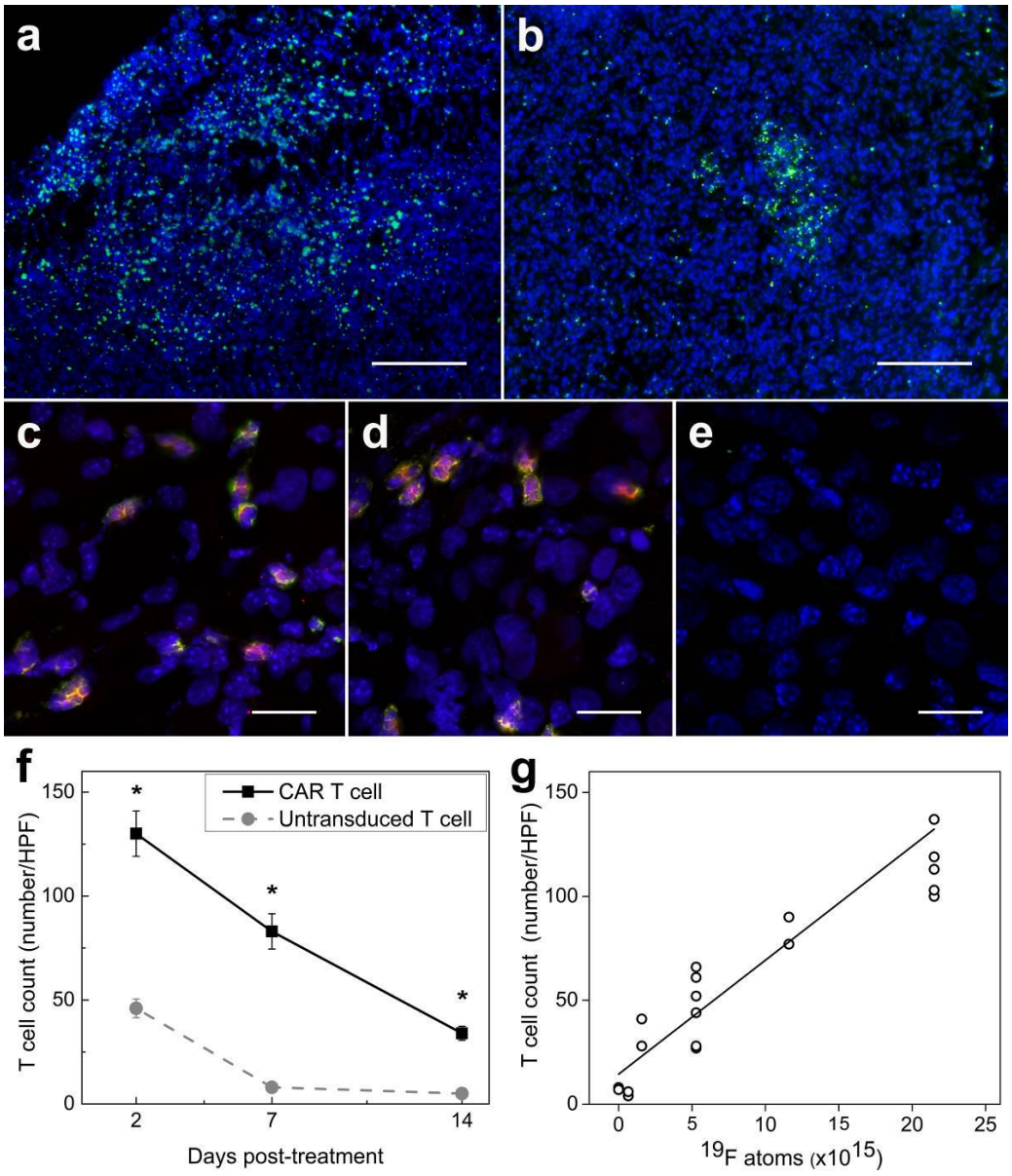

Figure 3.6. Histological correlation of tumor tissue of T cell treated SCID mice. (**a**) Low magnification (×5) fluorescent image of the tumor tissue displays prominent CD3+ CAR T cell infiltrates (green). (**b**) Conversely, sparse untransduced T cells localize to the tumor (scale bars = 100 μm). (**c**). Confocal images (×63) show that dual-mode PFC nanoemulsion (red) remains colocalized within CAR T cells (green, **c**) and untransduced T cells (**d**) at day 2 after infusion. (**e**) Untreated mice do not exhibit green or red fluorescence due to absence of treatment and endogenous T cells in SCID mice (scale bars = 25 μm). (**f**) Histological T cell count in high power fields of tumor sections shows greater CAR T cell numbers at all time points compared to sections from untransduced T cell-treated animals (* indicates $p < 0.001$). (**g**) Plot showing strong positive correlation ($r = 0.89$) between average ^{19}F atoms in tumors as measured by NMR and T cell count (N=120, HPF = high power fields)

CAR T cells and untransduced T cells are also present in large numbers in the spleen (Fig. 3.7a-b). Red fluorescence does not colocalize to phagocytic cells in the tumor and spleen (Fig. 3.7c-d), which indicates minimal contamination of dead T cell signal in these tissues, contrary to phagocytic Kupffer cells in the liver (Fig. 3.7e), which contain red fluorescence signal from dead T cells.

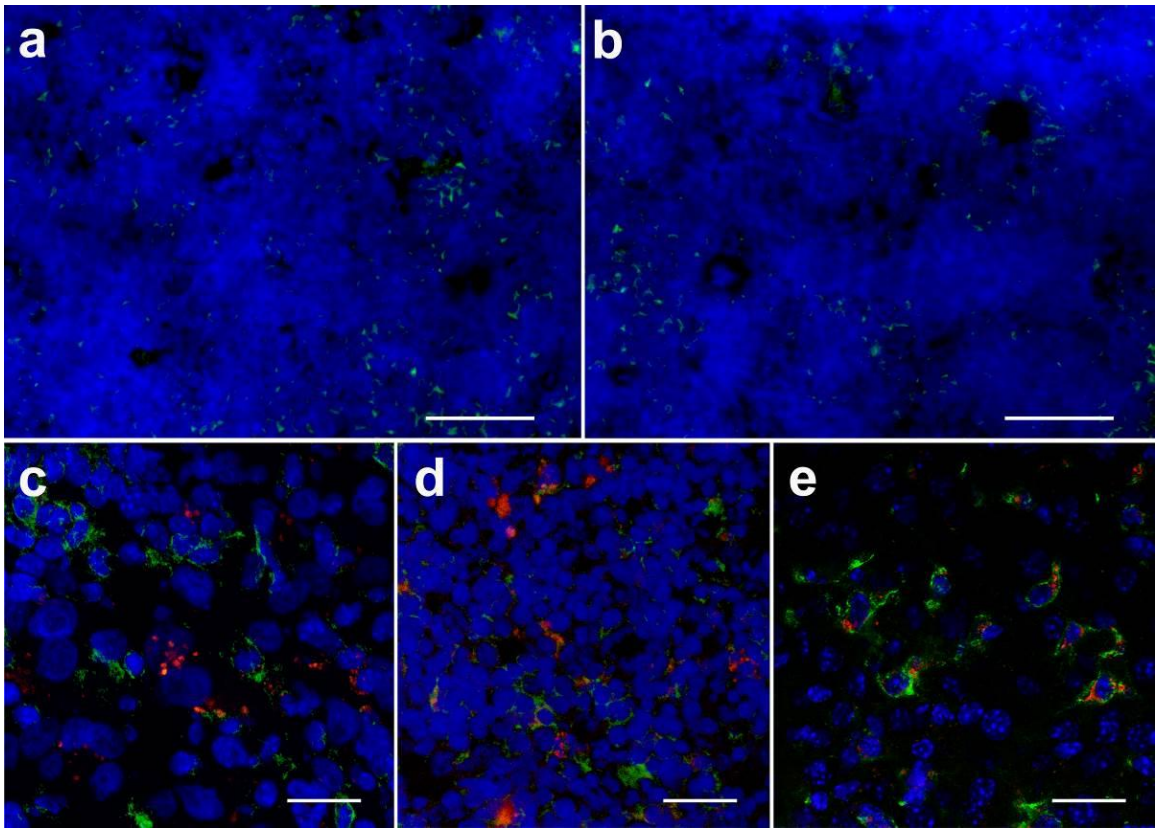

Figure 3.7. Histology in spleen and liver tissue of T cell treated SCID mice. (**a**) Low magnification (×5) fluorescent image of the spleen tissue displays prominent CD3+ CAR T cell infiltrates (green). (**b**) Untransduced T cells also localize to the spleen (scale bars = 50 μm). (**c**). Confocal images (×63) show that dual-mode PFC nanoemulsion (red) does not colocalize within phagocytic cells (F4/80 staining, green) in the tumor (**c**) and spleen (**d**) at day 2 after infusion. (**e**) Conversely, F4/80 staining in the liver tissue displays dual-mode PFC (red) colocalizing with Kupffer cells or liver macrophages (scale bars = 25 μm).

3.4. Discussion

We describe the use of NMR cytometry for quantifying the apparent biodistribution of human CAR T cell therapy in a murine xenograft model of glioma. We compared CAR T cell biodistribution and efficacy to untransduced T cells. Tumor growth and volume was assessed by bioluminescence imaging and caliper measurements. NMR measurements in whole organs demonstrated significantly higher CAR T cell homing to tumors and spleen compared to untransduced T cells, consistent with conventional histopathology staining. Our results corroborate the importance of the EGFRvIII receptor as a target for immunotherapy and the efficacy of CAR T cells against these tumors. Injection of untransduced lymphocytes did not result in enhanced tumor inhibition over untreated mice and appeared to have a lower and more transient accumulation at tumor sites compared to CAR T cells.

Our view is that NMR cytometry is an option for discovery and preclinical evaluation of emerging immunotherapeutic cell candidates by helping to streamline the evaluation of cell biodistribution and survival. One of the key advantages is that the analysis is in intact tissues, with the only treatment being an optional fixation step. PFC nanoemulsion internalized in cells does not alter the PFC chemical shift of the NMR spectrum which is defined by their molecular structure[23-25]. Moreover, The PFC label in tissue T cells is stable and can be stored or frozen indefinitely without signal loss[26-28]. Measurement of ^{19}F content of a sample can be accomplished using conventional NMR spectroscopy in tens of minutes or less, and data acquisition can be automated with robotic sample changers and auto-shimming. Programing automated data analyses routines to extract the PFC ^{19}F peak integrals and apparent cell counts is straightforward. Generally, NMR instrumentation is a routine analytic tool for molecule structure elucidation and is commonplace in virtually

every major chemistry lab, with tens of thousands of such instruments sited worldwide. Use of *in vitro* NMR cytometry as described herein has the advantage of higher sensitivity to sparser cell numbers compared to MRI by an order magnitude[9]. We note that the use of preclinical ^{19}F MRI in murine models of CAR T cell therapy remains a topic of future study.

If cell division occurs, the accuracy of the absolute T cell counts for NMR cytometry may diminish, particularly at later time points, thus we describe these as 'apparent' cell counts. The impact of cell division on PFC labeled T cell quantification during longitudinal studies in mouse is described in detail elsewhere[29]. Potentially a carboxyfluorescein succinimidyl ester (CFSE) assay can be used to determine mitosis rates *in vivo*[30]. However, considering the heterogeneity of cell phenotypes used in CAR T cell therapies, as well as differential division rates in different tissues, estimation of whole-body CAR T cell division rates *in vivo* remains challenging.

Labeling of T cells, which have weak phagocytic properties and a small cytoplasm, will always be a challenge, in contrast to phagocytic cells such as DCs. Nonetheless, authors have successfully labeled T cells *in vitro* using iron-based nanoparticles[31] or fluorinated nanoemulsions[32] and later tracked them *in vivo* by MRI. Similarly, natural killer (NK) cells have also been labeled with PFC and imaged longitudinally after intratumoral injection in mice[33]. The PFC nanoemulsion used in this study (CS-1000) has previously been used for numerous preclinical ^{19}F magnetic resonance imaging (MRI) studies of immune and stem cells in various disease models[26, 32-40]. By means of fluorescence and electron microscopy and flow cytometry, the dual-mode PFC nanoemulsion agent has been shown to be internalized by immune cells in multiple studies[12, 23, 32, 38, 41, 42]. Immune cell labeling with the nanoemulsion used (CS-1000) does not alter cell viability, phenotype or cytokine

production[26, 32, 33, 38]. In addition, the same imaging agent has been used in a clinical trial monitoring a PFC-labeled dendritic cell immunotherapy in colorectal cancer patients[7]. Moreover, CS-1000 is the subject of an FDA Drug Master File (DMF), as well as a similar DMF at Health Canada. Thus, the safety of this PFC nanoemulsion to cells and organisms at appropriate doses used in cell therapy has been extensively investigated. Utmost care and caution should nonetheless be applied before proceeding with any *in vivo* application of ^{19}F-labeled CAR T cells in human subjects.

Alternative methods for assessing cell distribution in preclinical studies often involve laborious and tissue-destructive histopathology, or flow cytometry measurements in blood and tissue samples prepared as single cell suspensions[3, 43, 44]. Analyses of tissues requires multiple manual processing and chemical treatment steps, as well as human input in the data collection and computer analysis, all of which are time-intensive. Histopathology remains semi-quantitative for analysis of multi-organ tissue panels, and is often limited by a finite number of tissue slices leading to potential sampling error, as well as confounding factors such as tissue autofluorescence[45]. Flow cytometry is most often used to measure remaining circulating T cells in blood. Others have reported that the average LOD for circulating T cells by flow cytometry is on the order of 3-10 CAR T cells per microliter of blood[44, 46, 47]. Thus, flow cytometry, as well as histology, may enable the detection of 'rare' cells in tissues.

To conclude, ^{19}F NMR cytometry is a rapid and quantitative technique to evaluate adoptive cell transfer biodistribution in intact tissues. This technique provides unbiased quantification in samples. Overall, ^{19}F NMR cytometry may accelerate the timeline to evaluate new immunotherapeutic cell candidates by providing a straightforward method to evaluate cell therapy biodistribution and cell fate.

Acknowledgements

Chapter 3, in full, is a reprint of the material as it appears in the journal *Scientific Reports* 2017, with minor revisions and formatting changes for this dissertation. The authors and title of the manuscript are as follows: Chapelin F, Gao S, Okada H, Weber T, Messer K, Ahrens E.T. Fluorine-19 nuclear magnetic resonance of chimeric antigen receptor T cell biodistribution in murine cancer model; Scientific Reports 2017. The authors acknowledge technical support from Mrs Hongyan Xu. The dissertation author was the primary investigator and author of this paper.

References

1. Rosenberg, S.A., Restifo, N.P., Yang, J.C., Morgan, R.A. & Dudley, M.E. Adoptive cell transfer: a clinical path to effective cancer immunotherapy. *Nat Rev Cancer* **8**, 299-308 (2008).

2. Razavi, S.M., Lee, K.E., Jin, B.E., Aujla, P.S., Gholamin, S. & Li, G. Immune Evasion Strategies of Glioblastoma. *Front Surg* **3**, 11 (2016).

3. Turtle, C.J., Hanafi, L.A., Berger, C., Gooley, T.A., Cherian, S., Hudecek, M., Sommermeyer, D., Melville, K., Pender, B., Budiarto, T.M., Robinson, E., Steevens, N.N., Chaney, C., Soma, L., Chen, X., Yeung, C., Wood, B., Li, D., Cao, J., Heimfeld, S., Jensen, M.C., Riddell, S.R. & Maloney, D.G. CD19 CAR-T cells of defined CD4+:CD8+ composition in adult B cell ALL patients. *J Clin Invest* **126**, 2123-2138 (2016).

4. Ahmed, N., Brawley, V.S., Hegde, M., Robertson, C., Ghazi, A., Gerken, C., Liu, E., Dakhova, O., Ashoori, A., Corder, A., Gray, T., Wu, M.F., Liu, H., Hicks, J., Rainusso, N., Dotti, G., Mei, Z., Grilley, B., Gee, A., Rooney, C.M., Brenner, M.K., Heslop, H.E., Wels, W.S., Wang, L.L., Anderson, P. & Gottschalk, S. Human Epidermal Growth Factor Receptor 2 (HER2) -Specific Chimeric Antigen Receptor-Modified T Cells for the Immunotherapy of HER2-Positive Sarcoma. *J Clin Oncol* **33**, 1688-1696 (2015).

5. Liu, X., Barrett, D.M., Jiang, S., Fang, C., Kalos, M., Grupp, S.A., June, C.H. & Zhao, Y. Improved anti-leukemia activities of adoptively transferred T cells expressing bispecific T-cell engager in mice. *Blood Cancer J* **6**, e430 (2016).

6. Magnani, C.F., Turazzi, N., Benedicenti, F., Calabria, A., Tenderini, E., Tettamanti, S., Giordano Attianese, G.M., Cooper, L.J., Aiuti, A., Montini, E., Biondi, A. & Biagi, E. Immunotherapy of acute leukemia by chimeric antigen receptor-modified lymphocytes using an improved Sleeping Beauty transposon platform. *Oncotarget* (2016).

7. Ahrens, E.T., Helfer, B.M., O'Hanlon, C.F. & Schirda, C. Clinical cell therapy imaging using a perfluorocarbon tracer and fluorine-19 MRI. *Magnetic resonance in medicine* **72**, 1696-1701 (2014).

8. FDA, C.f.B.E.a.R. (2013).

9. Ahrens, E.T. & Zhong, J. In vivo MRI cell tracking using perfluorocarbon probes and fluorine-19 detection. *NMR in biomedicine* **26**, 860-871 (2013).

10. Ahrens, E.T., Young, W.B., Xu, H. & Pusateri, L.K. Rapid quantification of inflammation in tissue samples using perfluorocarbon emulsion and fluorine-19 nuclear magnetic resonance. *Biotechniques* **50**, 229-234 (2011).

11. Kadayakkara, D.K., Beatty, P.L., Turner, M.S., Janjic, J.M., Ahrens, E.T. & Finn, O.J. Inflammation driven by overexpression of the hypoglycosylated abnormal mucin 1 (MUC1) links inflammatory bowel disease and pancreatitis. *Pancreas* **39**, 510-515 (2010).

12. Srinivas, M., Morel, P.A., Ernst, L.A., Laidlaw, D.H. & Ahrens, E.T. Fluorine-19 MRI for visualization and quantification of cell migration in a diabetes model. *Magnetic resonance in medicine* **58**, 725-734 (2007).

13. Johnson, L.A., Scholler, J., Ohkuri, T., Kosaka, A., Patel, P.R., McGettigan, S.E., Nace, A.K., Dentchev, T., Thekkat, P., Loew, A., Boesteanu, A.C., Cogdill, A.P., Chen, T., Fraietta, J.A., Kloss, C.C., Posey, A.D., Jr., Engels, B., Singh, R., Ezell, T., Idamakanti, N., Ramones, M.H., Li, N., Zhou, L., Plesa, G., Seykora, J.T., Okada, H., June, C.H., Brogdon, J.L. & Maus, M.V. Rational development and characterization of humanized anti-EGFR variant III chimeric antigen receptor T cells for glioblastoma. *Science translational medicine* **7**, 275ra222 (2015).

14. Carpenito, C., Milone, M.C., Hassan, R., Simonet, J.C., Lakhal, M., Suhoski, M.M., Varela-Rohena, A., Haines, K.M., Heitjan, D.F., Albelda, S.M., Carroll, R.G., Riley, J.L., Pastan, I. & June, C.H. Control of large, established tumor xenografts with genetically retargeted human T cells containing CD28 and CD137 domains. *Proc Natl Acad Sci U S A* **106**, 3360-3365 (2009).

15. Heimberger, A.B., Hlatky, R., Suki, D., Yang, D., Weinberg, J., Gilbert, M., Sawaya, R. & Aldape, K. Prognostic effect of epidermal growth factor receptor and EGFRvIII in glioblastoma multiforme patients. *Clin Cancer Res* **11**, 1462-1466 (2005).

16. Okada, H. & Kasahara, N. in Cancer Immunotherapy Principles and Practice. (eds. L.H. Butterfield, H.L. Kaufman & F. Marincola) In Press (Demos Medical Publishing, 2017).

17. Thorne, A.H., Zanca, C. & Furnari, F. Epidermal growth factor receptor targeting and challenges in glioblastoma. *Neuro Oncol* **18**, 914-918 (2016).

18. Ohno, M., Ohkuri, T., Kosaka, A., Tanahashi, K., June, C.H., Natsume, A. & Okada, H. Expression of miR-17-92 enhances anti-tumor activity of T-cells transduced with the anti-EGFRvIII chimeric antigen receptor in mice bearing human GBM xenografts. *Journal for immunotherapy of cancer* **1**, 21 (2013).

19. Kadayakkara, D.K., Damodaran, K., Hitchens, T.K., Bulte, J.W. & Ahrens, E.T. (19)F spin-lattice relaxation of perfluoropolyethers: Dependence on temperature and magnetic field strength (7.0-14.1T). *J Magn Reson* **242**, 18-22 (2014).

20. Nakashima, H., Ogawa, Y., Shono, S., Kinoshita, M., Nakashima, M., Sato, A., Ikarashi, M. & Seki, S. Activation of CD11b+ Kupffer cells/macrophages as a common cause for exacerbation of TNF/Fas-ligand-dependent hepatitis in hypercholesterolemic mice. *PloS one* **8**, e49339 (2013).

21. Seyda, M., Elkhal, A., Quante, M., Falk, C.S. & Tullius, S.G. T Cells Going Innate. *Trends Immunol* **37**, 546-556 (2016).

22. Yanagisawa, K., Moriyasu, F., Miyahara, T., Yuki, M. & Iijima, H. Phagocytosis of ultrasound contrast agent microbubbles by Kupffer cells. *Ultrasound Med Biol* **33**, 318-325 (2007).

23. Ahrens, E.T., Flores, R., Xu, H. & Morel, P.A. In vivo imaging platform for tracking immunotherapeutic cells. *Nature biotechnology* **23**, 983-987 (2005).

24. Partlow, K.C., Chen, J., Brant, J.A., Neubauer, A.M., Meyerrose, T.E., Creer, M.H., Nolta, J.A., Caruthers, S.D., Lanza, G.M. & Wickline, S.A. 19F magnetic resonance imaging for stem/progenitor cell tracking with multiple unique perfluorocarbon nanobeacons. *FASEB journal : official publication of the Federation of American Societies for Experimental Biology* **21**, 1647-1654 (2007).

25. Riess, J.G. Perfluorocarbon-based oxygen delivery. *Artificial cells, blood substitutes, and immobilization biotechnology* **34**, 567-580 (2006).

26. Helfer, B.M., Balducci, A., Nelson, A.D., Janjic, J.M., Gil, R.R., Kalinski, P., de Vries, I.J., Ahrens, E.T. & Mailliard, R.B. Functional assessment of human dendritic cells labeled for in vivo (19)F magnetic resonance imaging cell tracking. *Cytotherapy* **12**, 238-250 (2010).

27. Riess, J.G. Understanding the fundamentals of perfluorocarbons and perfluorocarbon emulsions relevant to in vivo oxygen delivery. *Artificial cells, blood substitutes, and immobilization biotechnology* **33**, 47-63 (2005).

28. Patrick, M.J., Janjic, J.M., Teng, H., O'Hear, M.R., Brown, C.W., Stokum, J.A., Schmidt, B.F., Ahrens, E.T. & Waggoner, A.S. Intracellular pH measurements using perfluorocarbon nanoemulsions. *Journal of the American Chemical Society* **135**, 18445-18457 (2013).

29. Srinivas, M., Turner, M.S., Janjic, J.M., Morel, P.A., Laidlaw, D.H. & Ahrens, E.T. In vivo cytometry of antigen-specific t cells using 19F MRI. *Magnetic resonance in medicine* **62**, 747-753 (2009).

30. Quah, B.J., Warren, H.S. & Parish, C.R. Monitoring lymphocyte proliferation in vitro and in vivo with the intracellular fluorescent dye carboxyfluorescein diacetate succinimidyl ester. *Nature protocols* **2**, 2049-2056 (2007).

31. Yeh, T.C., Zhang, W., Ildstad, S.T. & Ho, C. In vivo dynamic MRI tracking of rat T-cells labeled with superparamagnetic iron-oxide particles. *Magnetic resonance in medicine* **33**, 200-208 (1995).

32. Gonzales, C., Yoshihara, H.A., Dilek, N., Leignadier, J., Irving, M., Mieville, P., Helm, L., Michielin, O. & Schwitter, J. In-Vivo Detection and Tracking of T Cells in Various Organs in a Melanoma Tumor Model by 19F-Fluorine MRS/MRI. *PloS one* **11**, e0164557 (2016).

33. Bouchlaka, M.N., Ludwig, K.D., Gordon, J.W., Kutz, M.P., Bednarz, B.P., Fain, S.B. & Capitini, C.M. (19)F-MRI for monitoring human NK cells in vivo. *Oncoimmunology* **5**, e1143996 (2016).

34. Gaudet, J.M., Hamilton, A.M., Chen, Y., Fox, M.S. & Foster, P.J. Application of dual 19 F and iron cellular MRI agents to track the infiltration of immune cells to the site of a rejected stem cell transplant. *Magnetic resonance in medicine* (2016).

35. Somanchi, S.S., Kennis, B.A., Gopalakrishnan, V., Lee, D.A. & Bankson, J.A. In Vivo (19)F-Magnetic Resonance Imaging of Adoptively Transferred NK Cells. *Methods in molecular biology* **1441**, 317-332 (2016).

36. Rose, L.C., Kadayakkara, D.K., Wang, G., Bar-Shir, A., Helfer, B.M., O'Hanlon, C.F., Kraitchman, D.L., Rodriguez, R.L. & Bulte, J.W. Fluorine-19 Labeling of Stromal Vascular Fraction Cells for Clinical Imaging Applications. *Stem Cells Transl Med* **4**, 1472-1481 (2015).

37. Ribot, E.J., Gaudet, J.M., Chen, Y., Gilbert, K.M. & Foster, P.J. In vivo MR detection of fluorine-labeled human MSC using the bSSFP sequence. *International journal of nanomedicine* **9**, 1731-1739 (2014).

38. Helfer, B.M., Balducci, A., Sadeghi, Z., O'Hanlon, C., Hijaz, A., Flask, C.A. & Wesa, A. (1)(9)F MRI tracer preserves in vitro and in vivo properties of hematopoietic stem cells. *Cell transplantation* **22**, 87-97 (2013).

39. Bible, E., Dell'Acqua, F., Solanky, B., Balducci, A., Crapo, P.M., Badylak, S.F., Ahrens, E.T. & Modo, M. Non-invasive imaging of transplanted human neural stem cells and ECM scaffold remodeling in the stroke-damaged rat brain by (19)F- and diffusion-MRI. *Biomaterials* **33**, 2858-2871 (2012).

40. Boehm-Sturm, P., Mengler, L., Wecker, S., Hoehn, M. & Kallur, T. In vivo tracking of human neural stem cells with 19F magnetic resonance imaging. *PloS one* **6**, e29040 (2011).

41. Waiczies, H., Lepore, S., Janitzek, N., Hagen, U., Seifert, F., Ittermann, B., Purfurst, B., Pezzutto, A., Paul, F., Niendorf, T. & Waiczies, S. Perfluorocarbon particle size influences magnetic resonance signal and immunological properties of dendritic cells. *PloS one* **6**, e21981 (2011).

42. Janjic, J.M., Srinivas, M., Kadayakkara, D.K. & Ahrens, E.T. Self-delivering nanoemulsions for dual fluorine-19 MRI and fluorescence detection. *Journal of the American Chemical Society* **130**, 2832-2841 (2008).

43. Lee, D.W., Kochenderfer, J.N., Stetler-Stevenson, M., Cui, Y.K., Delbrook, C., Feldman, S.A., Fry, T.J., Orentas, R., Sabatino, M., Shah, N.N., Steinberg, S.M., Stroncek, D., Tschernia, N., Yuan, C., Zhang, H., Zhang, L., Rosenberg, S.A., Wayne, A.S. & Mackall, C.L. T cells expressing CD19 chimeric antigen receptors for acute lymphoblastic leukaemia in children and young adults: a phase 1 dose-escalation trial. *Lancet* **385**, 517-528 (2015).

44. Kunkele, A., Taraseviciute, A., Finn, L.S., Johnson, A.J., Berger, C., Finney, O., Chang, C.A., Rolczynski, L.S., Brown, C., Mgebroff, S., Berger, M., Park, J.R. & Jensen, M.C. Preclinical Assessment of CD171-Directed CAR T Cell Adoptive Therapy For Childhood Neuroblastoma: CE7 Epitope Target Safety and Product Manufacturing Feasibility. *Clin Cancer Res* (2016).

45. Stack, E.C., Wang, C., Roman, K.A. & Hoyt, C.C. Multiplexed immunohistochemistry, imaging, and quantitation: A review, with an assessment of Tyramide signal amplification, multispectral imaging and multiplex analysis. *Methods* **70**, 46-58 (2014).

46. Davila, M.L., Kloss, C.C., Gunset, G. & Sadelain, M. CD19 CAR-targeted T cells induce long-term remission and B Cell Aplasia in an immunocompetent mouse model of B cell acute lymphoblastic leukemia. *PloS one* **8**, e61338 (2013).

47. Hobbs, T.R., Blue, S.W., Park, B.S., Greisel, J.J., Conn, P.M. & Pau, F.K. Measurement of Blood Volume in Adult Rhesus Macaques (Macaca mulatta). *J Am Assoc Lab Anim Sci* **54**, 687-693 (2015).

Chapter 4: Cell penetrating peptide functionalized perfluorocarbon nanoemulsions for targeted cell labeling and enhanced fluorine-19 MRI detection

4.1. Introduction

Noninvasive methods for tracking cell therapy grafts are an urgent unmet clinical need[1, 2]. With the development of adoptive immunotherapy against cancer, such as using chimeric antigen receptor (CAR) T cell therapy[3, 4], there is a need to determine the initial biodistribution and survival of the therapeutic cells[5]. Visualizing cell populations *in vivo* can also provide insights into off-site toxicities and help refine dosing regimens to enhance therapeutic efficacy[6, 7].

Noninvasive imaging techniques for cell detection post-transfer often employ radioisotopes[8, 9], bioluminescence reporters[10], and fluorescence probes[11, 12]. Magnetic resonance imaging (MRI) is also being adapted to visualize cells[13]. MRI has no depth penetration limitations, displays anatomy with clarity, and can be used with in conjunction with imaging agents clinically[1, 14].

Fluorine-19 based MRI nanoemulsion probes are an option for non-invasively imaging of cell populations[15-21]. The ^{19}F nuclei have high intrinsic sensitivity, with 89% relative sensitivity compared to ^{1}H. *De minimis* endogenous ^{19}F in the body ensures that any MRI signals collected are from the introduced tracer probe. F-dense perfluorocarbon (PFC) molecules are often used to form nanoemulsion imaging probes that can be endocytosed by cells. As PFCs are mostly chemically inert, lipophobic, hydrophobic, and nanemulsions do not osmotically diffuse out of viable cells thereby ensuring lasting labeling. Detailed reviews of the biomedical applications of ^{19}F cell detection and tracking are found elsewhere[22-24].

Engineered lymphocytes commonly used in immunotherapy[25] have an intrinsically small cytoplasmic volume and are weakly phagocytic, thereby restricting uptake of intracellular PFC label. The limits of cell detection in spin-density weighted ^{19}F MRI is linearly proportional to the cell labeling levels. Thus, to boost cell labeling, we designed PFC nanoemulsion imaging probes displaying a cell penetrating peptide (CPP) from the transactivator of transcription (TAT) component of the human immunodeficiency virus type-1[26]. TAT is an 86 amino acid protein, and residues 49-58 [Arg-Lys-Lys-Arg-Arg-Gln-Arg-Arg-Arg] are positively charged and carry a nuclear localization signal sequence facilitating endocytosis[27]. We report the synthesis schemes and physical characterizations of three novel TAT co-surfactants for PFC nanoemulsion formulation. For PFC, we employ perfluoropolyether (PFPE, a perfluorinated polyethylene glycol) or perfluoro-15-crown-5-ether (PFCE); both molecules are used for ^{19}F MRI due to unitary major fluorine peaks and high sensitivity[28, 29]. The efficacy of TAT co-surfactants was tested by measuring cell uptake in Jurkat cells and in human primary CAR T cells. *In vitro* functional cell (glioma) killing assays were performed using TAT-PFC labeled CAR T cells. The intracellular localization of PFC oil droplets in labeled CAR T cells was investigated by fluorescence and electron microscopy. Additionally, we conducted proof-of-concept *in vivo* ^{19}F MRI sensitivity studies in CAR T cells labeled with TAT-PFC injected into flank gliomas.

4.2. Materials and Methods

4.2.1. Synthesis of F68-TAT

3.78 g of polyethylene-polypropylene (F68, 1 equiv, 0.0453 mmol, mol wt = 8350 g/mol, Spectrum Chemicals, Gardena, CA), purchased as a solid, was further dried under

high vacuum for 1 hour prior to use. To this dried white powder, 25 mL of anhydrous dichloromethane was added and stirred until dissolution, yielding a clear solution. Reaction was maintained under dry conditions using a steady stream of N_2 gas. 172 mg of 6-maleimidohexanoic acid (1.8 equiv, 0.815 mmol) was added in one portion yielding a pale yellow solution. 0.906 mL of N, N'-Dicyclohexylcarbodiimide (DCC) was added dropwise; solution cloudiness and formation of precipitate was observed almost immediately. The reaction was stirred overnight at room temperature under inert gas. Reaction was monitored by thin layer chromatography (TLC) with product retention factor (R_f) = 0.1 in 20:80:0.5 mix of MeOH:$CHCl_3$:AcOH. Reaction byproduct was removed by filtration. To the filtrate, an excess of hexanes was added causing the product to crash out which is collected by filtration. Product is a pale pink solid, **10** (yield = 2.183 g, mol wt = 8493 g/mol). To 2.5 mg of **10** (1 equiv, 0.00029 mmol) prepared as a 5 mg/mL solution in distilled water, 0.3 mg of Cys-TAT (0.68 equiv, 0.00020 mmol) prepared as a 2 mg/mL solution in HEPES buffer was added and allowed to stir overnight. Thereafter, 10 equiv of cysteine was added to cap any remaining maleimide groups. The contents of the reaction vessel were dialyzed (Slide-A-Lyzer Dialysis Cassettes, 3.5K MWCO, 3 mL, Thermo Scientific, Rockford, IL) to remove residual Cys-Tat (mol wt = 1661.99 g/mol) and cysteine (mol wt = 121 g/mol).

4.2.2. Synthesis of Perfluorocarbon (PFC) Nanoemulsions with Cell-Penetrating Peptide (CPP) and Poloxamer Surfactants

To prepare CPP surfactant, 1 mmol of 1H,1H-perfluoro-1-heptanol (0.350 g, 1 mmol, mol wt = 350 g/mol) or 1H,1H-perfluoro-3,6,9-trioxadecan-1-ol (0.398 g, 1 mmol, mol wt = 398 g/mol, Exfluor Research Corporation, Round Rock, TX) was added to a 25 mL round

bottom flask along with 232 mg 6-maleimidohexanoic acid (232 mg, 1.1 equiv, 1.1 mmol, mol wt = 211.32 g/mol, TCI America, Portland, OR). Anhydrous dichloromethane (5 mL) was added, and the flask was maintained under a constant stream of N_2 gas while stirring. Once the reactants dissolved, 572.4 mg benzotriazol-1-yl-oxytripyrrolidinophosphonium hexafluorophosphate (PyBOP, 572.4 mg, 1.1 equiv, 1.1 mmol, mol wt = 520.39 g/mol, Bachem, Torrance, CA) was added in one portion. After 2 min for the coupling reagent to dissolve, 350 µL of diisopropylethylamine (DIEA, 2 equiv, 2 mmol, Sigma Aldrich, St Louis, MO) was added to start the reaction. The flask was left under a slow N_2 stream with constant stirring at room temperature for 16 h. The reaction completion was monitored by TLC (R_f = 0.4, 3:7 EtOAc: hexanes). Purification and solvent removal were accomplished using a Combiflash Rf Lumen (Teledyne Isco, Lincoln, NE) silica gel column (12 g, silica Redisep column) using a hexane and ethyl acetate gradient with 1:0 hexane:EtOAc for 3 min, followed by an increase in polarity to 1:1 hexane:EtOAc from 3 min to 14 min, followed by a 0:1 hexane:EtOAc wash for 1 min. An evaporative light scattering (ELS) detector was used for monitoring product peaks, at 250 nm and 280 nm wavelengths, which elute at retention times (t_R) = 9 min (**1**) and t_R = 10.5 min (**2**), respectively. The collected fractions were concentrated with a rotary evaporator followed by drying on high vacuum overnight. The products are a clear oil with mol wt = 591.28 g/mol (**1**) (yield = 325 mg) and mol wt = 543.28 g/mol (**2**) (yield = 380.1 mg).

Cys-TAT.9TFA (30 mg, 0.016 mmol, 1 equiv, mol wt = 2688.16 g/mol, Biomatik, Wilmington, DL) and dissolved in 464 µL of 0.05% TFA-water. A solution of **1** or **2** (0.014 mmol) in trifluoroethanol (556 µL) was then added to the solution of Cys-TAT, followed by the addition of 116 µL of 1 M 3-(*N*-morpholino)propanesulfonic acid (MOPS) buffer at pH

= 7.4. Reaction completion was assessed by liquid chromatography mass spectroscopy (LC-MS, Model 1100 with LC/MSD Trap, Agilent, Santa Clara, CA) using a 95:5 gradient of water + 0.05% TFA: acetonitrile + 0.05% TFA for 5 min, then 95:5 to 10:90 in 20 min, followed by 10:90 to 0:100 in 10 min, t_R = 18.5 min (**1**) and t_R = 18.6 min (**2**)] and stopped after 30 min by addition of 100 µL of glacial acetic acid. Following filtration (0.22 µm nylon filter), the crude mixture was purified by semi-prep high pressure liquid chromatography [HPLC, gradients used: 90:10 descending to 10:90 water + 0.05% TFA, acetonitrile + 0.05% TFA in 20 min, t_R = 12.5 min, *m/z* = 1127.4, mol wt = 2254.28 g/mol (**1a, TATP**) and t_R = 13.7, *m/z* = 1103.5, mol wt = 2206.28 g/mol (**2a, TATA**)].

To prepare nanoemulsions, a 5% w/w ratio of total surfactant to PFC was used. For 4 mL of nanoemulsion product, 40 mg of F68 in 400 µL of water was added to a glass vial containing 465 µL perfluo-15-crown-5-ether (PFCE, Exfluor Research, Round Rock, TX). To this solution, 4 mg (1.21 µmol) of TATP (**1a)** or TATA (**2a**) (1.23 µmol) was added followed by 3.135 mL of purified water. The solution was ultrasonicated (30% power, 1 min, Omni Ruptor 250W, Kennesaw, GA) and then passed through a microfluidizer (LV1, Microfluidics, Westwood, MA) at 10,000 psi pressure four times. The TATA- and TATP-F68-PFC (**3**) nanoemulsions were sterile filtered using a 0.22 µm syringe filter (Acrodisc PF, Pall, Port Washington, NY) and bottled in autoclaved glass vials. The capped vials were stored at 4 °C until use.

4.2.3. Synthesis of PFC Nanoemulsions with CPP-Phospholipid Surfactants

For CPP-phospholipid surfactant, 1,2-distearoyl-sn-glycero-3-phosphoethanolamine-N-[maleimide(polyethyleneglycol)-2000] (DSPE-PEG2000-

maleimide, 1.8 equiv., 0.00217 mmol, 6.5 mg, Avanti Polar Lipids, Alabaster, AL) was suspended in HEPES buffer (0.05 M, 500 μL, pH = 7.5) by sonication. A fresh solution of Cys-TAT (1 equiv, 0.0012 mmol, 2.0 mg) in HEPES buffer (0.05 M, 300 μL, pH = 7.5) was added in one portion, and the mixture was agitated on a shaker at 37 °C for 6 hours. 2-Mercaptoethanol (0.8 μL, 10 equiv, 0.012 mmol, Sigma Aldrich) was added to react with any remaining maleimide groups, and the solution was agitated further for 30 min.

The conjugate was de-salted and purified in deionized water using a dialysis cassette (Slide-A-Lyzer #2K MWCO, cassette size = 3 mL, Thermo Scientific) at room temperature. Water was replaced at 2, 4 and 22 hours (volume 300:1 compared to cassette size). The sample was recovered from cassette and analyzed by matrix assisted laser desorption/ionization (MALDI) mass spectrometry (Biflex IV MALDI-TOFMS, Bruker, Billerica, MA) and identified as a mixture of the desired product, DSPE-PEG(2000)-Cys-TAT (mol wt= 4660 g/mol) **4** and DSPE-PEG(2000)-mercaptoethanol (mol wt= 3020 g/mol). The solution was lyophilized to a dry powder to give a near-quantitative yield of the desired product, **4**.

The phospholipid-PEG-TAT conjugate was incorporated into egg yolk phospholipid (EYP) by the two methods described below. For both methods, compound **1** (2.8 mg, 0.6 μmol) and EYP (304 mg, 0.4 mmol, Sigma Aldrich) were mixed resulting in a TAT to lipid surfactant ratio of 0.15 mol %. Thereafter, perfluoropolyether (PFPE) oil (1.18 g, 0.87 mmol, mol wt = 1300-1400 g/mol, Exfluor) was added to obtain a 26% w/w ratio of phospholipid to PFC. Sterile water was added to obtain a 120-150 mg/mL concentration of PFC. The nanoemulsions were then sterile-filtered through (0.2 μm, Pall) into glass vials, capped, and

stored at 4 °C until use. Following formulation and filtration, each nanoemulsion was characterized by dynamic light scattering (DLS) particle analysis and ^{19}F NMR.

Method 1: Direct Insertion of Peptide Conjugate

Compound **4** was added to a solution of EYP in chloroform (5 mL), vortexed on medium for 1 min, and the resulting solution evaporated with a stream of nitrogen while manually rotating the vial to evenly coat the vessel. The vial was then placed under high vacuum overnight to give a dry lipid film. Sterile water was added to hydrate the lipid film for 5 min followed by vortexing on medium for 2 min and then ultrasonication (30% power, 4 min). PFPE was added to the vial in one portion, vortexed briefly, and then ultrasonicated (30% power, 2 min). The crude emulsion (**5**) was passed four times through a microfluidizer at 20,000 psi with the reaction chamber cooled on ice.

Method 2: Post-Insertion of Peptide Conjugate

A suspension of EYP in sterile water was formed by ultrasonication (30% power, 4 min), and PFPE oil was added to the vial in one portion, vortexed briefly, and then ultrasonicated (30% power, 2 min). The crude emulsion was passed four times through a microfluidizer as in Method 1. To add TAT, solutions of **1** based on mol% of total EYP surfactant were prepared in sterile water. The solution of **1** is added to the preformed nanoemulsion and agitated on a bioshaker at 37 ºC for 5 h to obtain (**5**) nanoemulsion.

4.2.4. Nanoemulsion Size and Homogeneity

DLS instrumentation (Zetasizer ZS, Malvern Panalytical, Malvern, UK) was used to determine the particle size, polydispersity index (PDI) and zeta potential for the samples. Nanoemulsions were diluted to 0.5% v/v in water and transferred to low volume (1.5 mL) disposable cuvettes. Measurements were performed in triplicate samples for each nanoemulsion.

4.2.5. *^{19}F NMR Measurement of Nanoemulsion Fluorine Concentration*

The ^{19}F NMR spectral data were acquired using a 400 MHz Bruker NanoBay Spectrometer (Bruker BioSpin, Billerica, MA) with a single 17 μs pulse, 32,000 free induction decay points, 100 ppm spectral width, 32 averages and 15 s repetition time. NMR samples were prepared by adding 0.1% (w/v) sodium TFA in D_2O to nanoemulsion (10% v/v). The concentration of PFC in nanoemulsion (C_F) was calculated from the integrals of the TFA signal (normalized to 1) and the major PFC peak (I_{PFC}) using the relation $C_F = a\, I_{PFC} C_{TFA} V_{TFA} (b V_{PFC})^{-1}$, where C_{TFA} is the concentration of TFA in mg/mL, V_{TFA} and V_{PFC} respective volumes of nanoemulsion and 0.1% TFA solution in mL in the NMR sample, and a and b are constants representing the ^{19}F mass fraction of TFA (0.42) and PFC (*e.g.*, 0.655 for PFCE and 0.58 for PFPE), respectively.

4.2.6. T Cell Preparation

The Jurkat T cell line was obtained commercially (#TIB-152, ATCC, Manassas, VA) for initial nanoemulsion cell labeling characterizations. Jurkat cells were grown in RPMI-1640 media (Gibco, Waltham, MA) plus 10% fetal bovine serum (FBS), 10 mM HEPES

buffer (4-(2-hydroxyethyl)-1-piperazineethanesulfonic acid), 1 mM sodium pyruvate and 1.5 mg/mL sodium bicarbonate media.

Primary human T cells were obtained from blood samples sourced from the San Diego Blood Bank and enriched for T cells by Ficoll (Histopaque 1077, Sigma Aldrich) gradient density centrifugation and magnetic assisted cell sorting (Dynabeads, Thermo Fisher). T-cells were then activated with human T-activator CD3/CD28 Dynabeads and allowed to expand for two days in RPMI-1640 supplemented with 10% FBS and 100 units/mL of recombinant human interleukin 2 (IL-2, Peprotech, Rocky Hill, NJ). For transduction, we employed a vector specific to epidermal growth factor receptor variant III (EGFR-vIII) as described by Johnson *et al*[30]. A detailed protocol for chimeric antigen receptor (CAR) virus production and human T cell transduction is available elsewhere[31]. CAR receptor expression was confirmed by flow cytometry. We used T cell populations with >70% CAR+ expression.

4.2.7. Glioma Cell Line

A human glioblastoma multiform (U87-EGFRvIII-Luc) cell line overexpressing EGFR-vIII[32] and the luciferase reporter gene (Luc) were used. Cells were incubated (37 ºC, 5% CO_2) and cultured in T-75 flasks (Thermo Fisher) in RPMI-1640 medium supplemented with 10% FBS.

4.2.8. In Vitro T Cell Labeling

For initial uptake experiments, 1 million Jurkat or CAR T cells were plated in 1 mL full media in 24 well plates (n = 3 wells per condition). PFC nanoemulsion was added to

each well and incubated overnight (16 h) at 37 ^{o}C and 5% CO_2. The cells were then washed three times with phosphate buffered saline (PBS) to rinse free nanoemulsion. Cells were counted and viability was assessed by Trypan blue staining. Thereafter, the cells were spun down, resuspended in 150 μL lysis buffer (1% Triton X in PBS) and transferred to a 5 mm NMR tube. 50 μL 0.1% TFA was added to each NMR tube, and spectra were acquired as described above. Total fluorine atom count was divided by the sample cell number to yield the average number of fluorine atoms per cell.

For *in vivo* experiments, CAR T cells were plated at a density of 10 million cells in 5 mL of media per well of a 6-well plate and incubated overnight with 15 mg/mL of nanoemulsion. Cells were washed as described above and an aliquot of 1 million cells was set aside to measure cell uptake by ^{19}F NMR.

4.2.9. Synthesis of Cyanine-5 (Cy5) Fluorescence Nanoemulsions

TAT-PFC nanoemulsions were prepared with Cy5 dye attached. To 0.5 mmol of 1H,1H-Perfluoro-1-heptanol (mol wt = 350.08 g/mol) or 1H,1H-Perfluoro-3,6,9-trioxadecan-1-ol (mol wt = 398.08 g/mol), we added 0.55 mmol of 6-(Boc-amino)caproic acid (mol wt = 231.29 g/mol, Sigma Aldrich); this mixture was dissolved in a minimum amount of dry dichloromethane (DCM), and the reaction mix was stirred under N_2 gas. 0.55 mmol pyBOB (benzotriazol-1-yl-oxytripyrrolidinophosphonium hexafluorophosphate) was added, followed by 0.74 mmol of diisopropylethylamine (DIEA), and mixture was stirred under inert gas overnight at room temperature. Reaction completion was monitored by TLC. The solvent was removed with a rotary evaporator, and sample was dissolved in minimum amount of DCM. Wet crude sample was loaded on a 4 gm silica gel Redisep column for purification using the Combiflash Rf Lumen. We eluted with 100% hexane for 2 min, then

70%:30% EtOAc:hexane over 10 min. The desired product **6** or **7** was eluted between 30-40% EtOAc and t_R = 6-7.5 min, as monitored by ELS detector.

Boc protecting group in compound **6** or **7** was removed by adding 1 mL of TFA and 3 mL of DCM while stirring at room temperature for 1 h. The TFA was removed by forming an azeotrope with toluene, and the sample was dried under a rotary evaporator followed by high vacuum to extract all solvents. LC-MS used 10:90 to 90:10 Acetonitrile + 0.05% TFA:H_2O in 20 min. The purified compound eluted at t_R = 15.3 min, *m/z* = 515.3 (**6a**) and t_R = 16.6 min, *m/z* = 564.0 (**7a**) using the 215 nm detector.

A 25 mM stock solution of **6a** or **7a** was prepared by dissolving weighed oil in calculated amount of trifluoroethanol. We used 8 µL of 6 mM Cy5-N-hydroxysuccinimide (Cy5-NHS, 48 nmol, GE Healthcare, Chicago, IL) and an excess of **6a** or **7a** (approximately 20 equiv, 960 nmol or 38.5 µl of 25 mM stock prepared above) was added. The molar equivalent amount of N-methyl morpholine was added, prepared as a 50 mM solution in DMSO. The reaction was stirred at room temperature overnight. Thereafter, 2 µl of acetic acid was added, and the reaction mix was purified by HPLC (gradient 10:90 to 90:10 water + 0.05% TFA:Acetonitrile + 0.05% in 20 min and retain at 90:10 for an additional 10 min on a Phenomenex Luna 5 µm C18(2) 100 Å, 250 x 10 mm column). The desired product was eluted at t_R = 21.6 min, *m/z* = 1150.3 (**8**) and t_R = 20.3 min, *m/z* = 1102.3 min (**9**), as monitored by UV absorbance at 650 nm.

To prepare nanoemulsions, we used the procedure as described above. Prior to sonication, 0.3 µM of **8** is added to cocktail where TATP is used as the chosen anchor. Similarly, 0.3 µM of **9** is added to cocktail using TATA. Following sonication and microfluidization a faint blue nanoemulsion is obtained.

4.2.10. Fluorescence Microscopy

Aliquots of CAR T cells (1×10^6 cells, N = 3) were labeled with Cy5-TATP-F68-PFC nanoemulsion or mock-labeled for a 24 h period and then fixed with 4% paraformaldehyde for 20 min. Cells were stained with CD3-Alexa488 (1:200 dilution, Biolegend, San Diego, CA) and Hoechst dye nuclear stain (#33342, 1:500 dilution, Thermo Fisher). Cells were then mounted in Aqua-Mount media (Lerner Laboratories, Cheshire, WA), and slides were imaged using a confocal microscope (Model A1, Nikon Instruments, Melville, NY) with a 40× water immersion objective and 405 nm, 488 nm and 640 nm lasers for excitation.

4.2.11. Tumor Cell Killing Assay

U87-EGFRvIII-Luc cells were plated at a density of 30,000 cells per well in clear bottom 96-well plates (Corning, Inc., Corning, NY) and were allowed to adhere overnight (60 wells total for two time points). Wells (n = 6, per condition) received: (i) 5:1 ratio of CAR T cells to cancer cells, (ii) 5:1 ratio of TATP-F68-PFC-labeled CAR T cells to cancer cells, (iii) 5:1 ratio of untransduced T cells to cancer cells, (iv) 5:1 ratio of TATP-F68-PFC-labeled untransduced T cells to cancer cells or (v) untreated cancer cells for baseline signal. At 12 and 24 hours post T cell treatment, D-luciferin (300 μg/mL, Biosynth International, Itasca, IL) was added to wells and bioluminescence signals were immediately measured with a plate reader (Infinite M200PRO, Tecan, Morrisville, NC). The relative U87-EGFRvIII-Luc cell killing efficacy was obtained from the mean photon count for groups (i-iv); the numerical differences between treated versus untreated (v) means are displayed as percentages.

4.2.12. Electron Microscopy

To confirm intracellular PFC localization, we examined CAR T cells labeled with TATP-F68-PFC or TATA-F68-PFC alongside unlabeled CAR T cells using electron microscopy. Cells were labeled as above. CAR T cell pellets were fixed in PBS containing 2% glutaraldehyde in 0.1 M sodium cacodylate (SC) buffer at room temperature for 30 min and stored overnight at 4 °C. The cells were washed five times in 0.1 M SC buffer on ice and treated with 1% OsO_4 in 0.1 M SC buffer for 1 hour. All samples were washed in deionized water and treated with 2% uranyl acetate for 1 hour on ice. Pellets were dehydrated in ethanol and then anhydrous acetone. The cells were embedded in a solution containing a 1:1 mixture of acetone and Durcupan resin (Sigma-Aldrich) for 2 h on a tube rotator and then in 100% Durcupan overnight. The next day, cell pellets were embedded in Durcupan resin and polymerized over 36 h at 60 °C. Ultra-thin (60 nm) sections were cut using a diamond knife and collected on Cu mesh grids. The samples were stained with 1% aqueous uranyl acetate and Reynolds lead citrate. Sections were imaged using a Tecnai Spirit electron microscope (FEI, Hillsboro, OR) at 80 kV.

4.2.13. Flow Cytometry

Potential impact of TATP-F68-PFC on CAR T cell phenotype and viability was evaluated by measuring surface expression levels of CD3, CD4, CD8, and 7-AAD (viability marker) by flow cytometry (LSR Fortessa, BD Biosciences, San Jose, CA). We used Alexa488 anti-human CD3 clone HIT3a, Phycoerythrin-cyanine 5 (PE-Cy5) anti-human CD4 clone OKT4, Fluorescein isothiocyanate (FITC) anti-human CD8 clone SK1, and 7-

Aminoactinomycin D (7-AAD) viability marker (all purchased from Biolegend, San Diego, CA). In these assays, we evaluated CAR T cells without PFC label as controls. Flow cytometry data processing used FlowJo software (FlowJo, Ashland, OR).

4.2.14. In Vivo MRI

All animal protocols were approved by the University of California, San Diego, Institutional Animal Care and Use Committee (IACUC). Bilateral subcutaneous flank tumors were implanted in N = 4 female NOD/SCID 4-6 week old mice (Jackson Laboratories, Bar Harbor, ME). Tumor inoculant consisted of 5×10^6 U87-EGFRvIII-Luc tumor cells in 100 μL matrigel (Corning, Tweksbury, MA) in PBS (1:1). Five days later, mice received intra-tumoral injection of 1×10^7 labeled CAR T cells labeled with either TATP-F68-PFC or PFC-F68 nanoemulsion. Two hours after intratumoral injection, mice were anesthetized with 1-2% isoflurane in O_2 and positioned an 11.7 T Bruker BioSpec preclinical scanner with a dual-tuned $^1H/^{19}F$ birdcage volume coil. Animal temperature was regulated, and respiration was monitored during scans. A reference capillary with dilute PFC nanoemulsion was positioned along the animal in the image field of view (FOV). The ^1H anatomical images were acquired using the RARE (rapid acquisition with relaxation enhancement) sequence with TR/TE = 2000/13 ms, RARE factor 4, matrix 256×184, FOV 38×30 mm^2, slice thickness 1 mm, 18 slices, and 4 averages. The ^{19}F images were also acquired using a RARE sequence with parameters TR/TE = 1500/4.7 ms, RARE factor 8, matrix 64×46, FOV 38×30 mm^2, slice thickness 1 mm, 18 slices, and 400 averages. The total number of fluorine atoms per voxel in tumor regions were estimated directly from the *vivo* ^{19}F image hot-spots using the software program Voxel Tracker (Celsense, Pittsburgh, PA),

which also employs image measurements of the external ^{19}F reference capillary signal and noise as inputs, and yields a statistical uncertainty of ^{19}F-count; additional details about this analysis are published elsewhere[33]. For display, ^{19}F images were manually thresholded to remove background noise, and $^{1}H/^{19}F$ renderings were performed in ImageJ by overlaying ^{1}H (grayscale) and ^{19}F (hot-iron, pseudo-color scale) slices. The fluorine images were also resampled in ImageJ to obtain a matrix size of 2048×2048 and converted to 32 bit images to keep the number of pixels constant. Regions of interest (ROI) were segmented around relevant ^{19}F signals (right tumor, left tumor and noise) on slices, and ROI voxel intensities were displayed as histograms.

4.2.15. Ex Vivo Microimaging of Tumors

Two days after intratumoral injection, animals were sacrificed by CO_2 inhalation and tumors were excised with the surrounding skin tissue. Tumors were fixed in 4% paraformaldehyde overnight, rinsed in PBS, and transferred to a 10 mm NMR tube (Wilman Labglass, Vineland, NJ) containing a 2% agarose solution (Fisher Scientific, Hampton, NH). Images of the tumors were acquired on a Bruker 400 MHz NanoBay NMR spectrometer equipped with microimaging accessories and a 10 mm $^{19}F/^{1}H$ microimaging coil. Proton anatomical images were acquired with a three-dimensional (3D) spin-echo sequence using TR/TE = 800/25 ms, matrix 256×128×128, FOV 9.5×9.5×12 mm^3 and 1 average. Fluorine images were acquired with a 3D RARE sequence using TR/TE = 2000/9.7 ms, RARE factor 4, matrix 128×64×64, FOV 9.5×9.5×12 mm^3 and 35 averages. The $^{1}H/^{19}F$ image overlays were performed in ImageJ.

4.2.16. Statistical Analyses

Measurements are presented as mean ± standard deviation. We performed unpaired T-tests with unequal variances to compare *in vivo* groups. Two tailed P-values < 0.05 were considered statistically significant.

4.3. Results

To increase the cellular uptake of PFC nanoemulsion, we chemically modified and attached the TAT peptide to the surfactant to display the hydrophilic and positively charged cell penetrating moiety on the nanoemulsion surface. We tested two general methods (Fig. 4.1) for peptide incorporation into PFC nanoemulsions; these were formed with either polyethylene polypropylene glycol block polymer (Pluronic F68) or phospholipid. For the poloxamer surfactant, we first conjugated TAT with a terminal cysteine (TAT-cys) directly to F68 functionalized with a maleimide group (F68-TAT) (Fig. 4.S1)[34]. However, PFC nanoemulsions formed with F68-TAT incorporated at ≥2% w/w of the F68 surfactant lacked long term stability and emulsions that had <1% F68-TAT resulted in negligible cell uptake (data not shown). A successful approach involved conjugation of Cys-TAT to one of two small fluorous molecule anchors via a short hydrocarbon linker (Fig. 4.1a) bearing a maleimide group that was synthesized from the corresponding alcohols and 6-maleimidocaproic acid using benzotriazol-1-yl-oxytripyrrolidinophosphonium hexafluorophosphate (PyBOP) as a condensation agent. The two anchors consisted of either a perfluoroheptyl (TATA) or a short perfluoroPEG (seven atom backbone) group (TATP),

designated TATA-F68-PFC and TATP-F68-PFC, respectively, with variable percentages by weight (% w/w). Following emulsification of PFC and surfactants, both nanoemulsion formulations yielded an average size particle of 180 nm (Figs. 4.S2a, b) with a polydispersity index (PDI) of ~0.0795-0.095, measured by light scattering methods, and particle size slightly increased by an average of 9% by day 45 post synthesis, but stabilized, and did not separate into fluorous and aqueous phases over three months (Figs. 4.S2c, d).

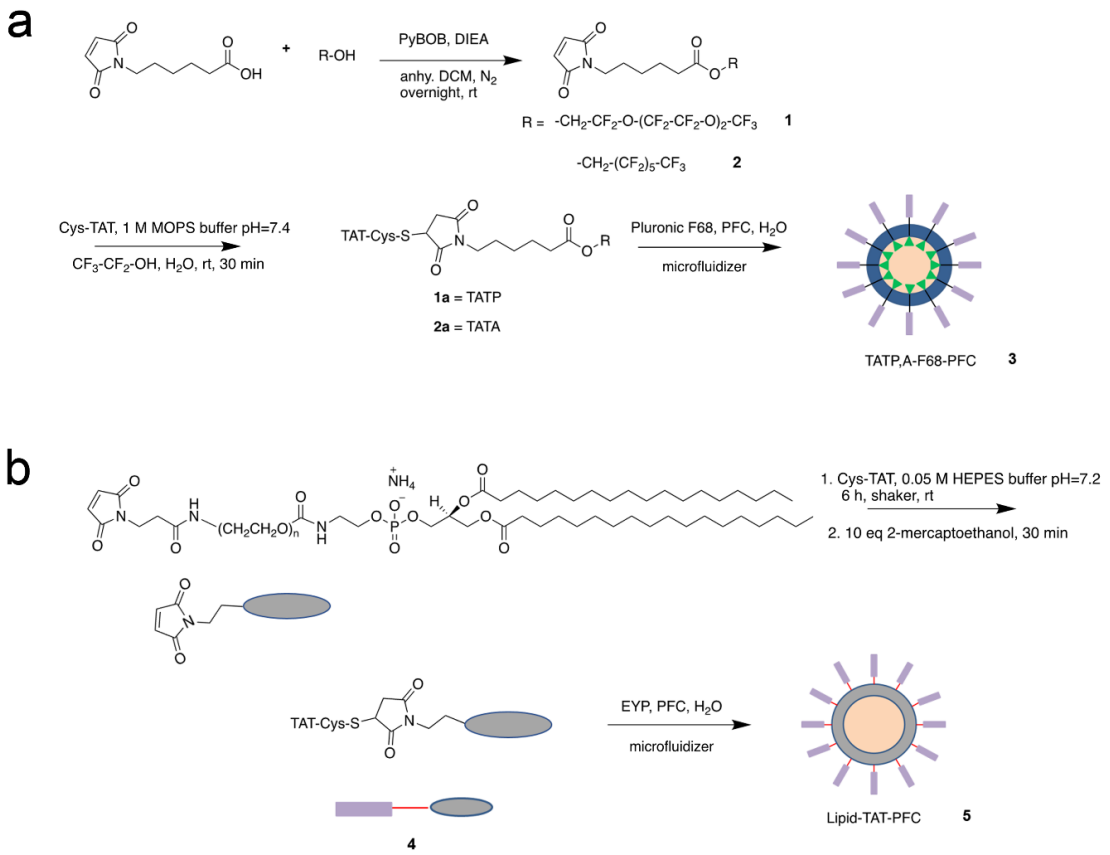

Figure 4.1. Synthesis of TAT functionalized perflurocarbon nanoemulsions. Panel (**a**) displays synthesis of TAT conjugates with fluorous anchors, TATP and TATA and poloxamer surfactant formulated PLC nanoemulsions. Panel (**b**) shows scheme for TAT-phospholipid anchor conjugation for EYP surfactant formulated PFC nanoemulsion.

Incorporation of the TAT anchored co-surfactants into F68 formulated PFC nanoemulsions resulted in significantly enhanced uptake by Jurkat cells following an 18 hour incubation (Fig. 4.2). At low CPP stoichiometry in nanoemulsion (2.5% w/w TAT), 5.33 (±0.71) $\times 10^{11}$ ^{19}F/cell for TATP-F68-PFC and 4.67 (±0.59) $\times 10^{11}$ ^{19}F/cell for TATA-F68-PFC (dose 10 mg/ml in media, Fig. 4.2A) was measured using ^{19}F NMR of cell pellets. For higher nanoemulsion CPP content (10% w/w TATP), cell uptake was increased to 6.82 (±1.92) $\times 10^{11}$ F/cell compared to 2.25 (±0.15) $\times 10^{11}$ ^{19}F/cell for control F68-PFC nanoemulsion; similarly, TATA-F68-PFC nanoemulsion yielded uptake values of 5.26 (±0.86) $\times 10^{11}$ ^{19}F/cell (Fig. 4.2A). Addition of either TATP or TATA did not impair cell viability (Fig. 4.2B) as measured by permeability to Trypan blue. Incubation of Jurkat cells with TATP-F68-PFC or TATA-F68-PFC with increasing concentrations of nanoemulsion in culture displays a canonical sigmoidal uptake pattern (Fig. 4.2C). CAR T cells labeled with TATP-F68-PFC at 15 mg/ml exhibit an average 8.2-fold uptake improvement compared to control F68-PFC-labeled cells (Fig. 4.2E). TATA-harboring nanoemulsions exhibited mild toxicity to cells with a decrease in cell viability to 85.3% at 10 mg/mL and 83% at 20 mg/mL compared to 97.7% for untreated cells (Fig. 4.2D). At the same doses, TATP containing nanoemulsions remained non-toxic to the cells with viability of 92% for 10 mg/mL dose and 91.7% for 20 mg/mL dose (Fig. 4.2D).

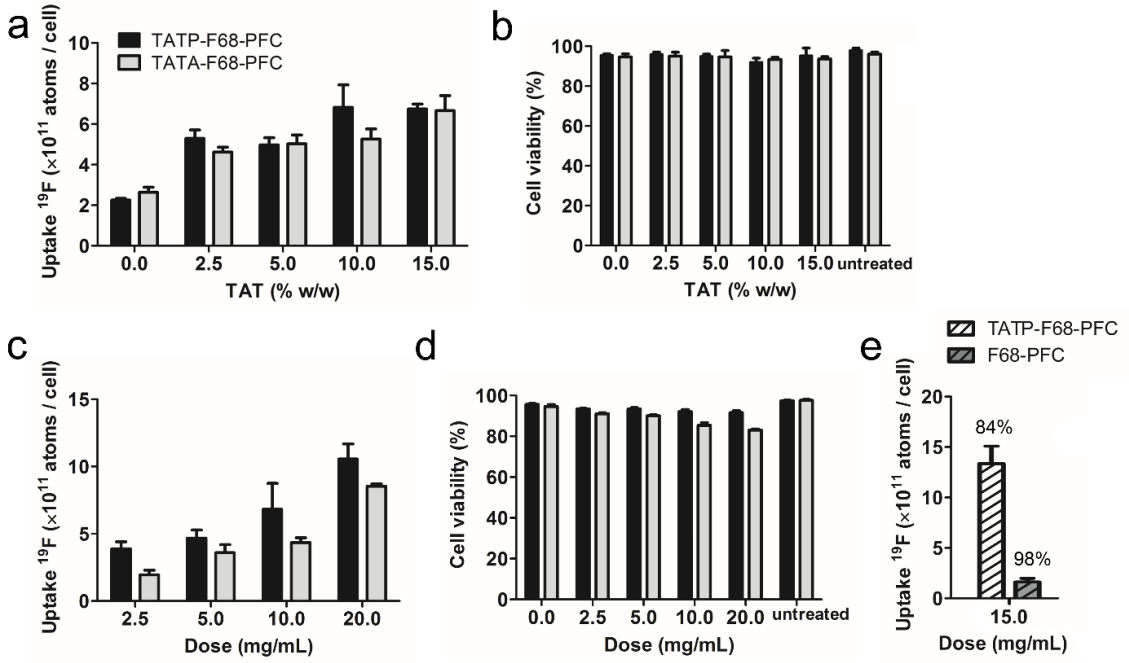

Figure 4.2. Jurkat cell labeling with TATA-F68-PFC and TATP-F68-PFC nanoemulsions. The TAT anchor stoichiometry is optimized by measuring uptake (**a**) and viability (**b**) in Jurkat cells while varying the percent by weight of TAT in pluronic surfactant PFC nanoemulsion, namely TATP-F68-PFC (black bars) and TATA-F68-PFC (grey bars). Cell uptake (**c**) and viability (**d**) for varying dosages (in mg/mL) of 10% w/w TATP-F68-PFC and TATA-F68-PFC after 18 hour incubation are shown. CAR T cells labeled in the same conditions exhibit an average 8.2-fold uptake improvement compared to control F68-PFC-labeled cells at a dose of 15 mg/ml (dashed bars, **e**). Average viability of labeled CAR T cells is displayed above the bar graph. Uptake was measured from ^{19}F NMR spectra of cell pellets, and viability was measured by trypan blue assay and direct cell counts.

Alternative PFC nanoemulsions were also formed with the egg yolk phospholipid (EYP) surfactant, where cys-TAT was conjugated to commercially available 1,2-Distearoyl-sn-glycero-3-phosphoethanolamine-peg2000-maleimide[35] (Fig. 4.1B), and the product **4** was confirmed by Matrix Assisted Laser Desorption/Ionization mass spectrometry. Conjugate **4** was inserted into nanoemulsion either into the crude mix prior to emulsification ("direct insertion") or after emulsification ("post-insertion"). Formed nanoemulsions containing the adduct up to 0.15 mol % (of EYP) averaged 160 nm in size with a PDI~0.2 immediately after emulsification; particle size did not change significantly over >10 weeks

post-production. No differences in size or zeta potential were observed for lipid-based nanoemulsions prepared with or without anchored TAT.

Cell labeling using TAT-modified pegylated phospholipid incorporated into EYP-surfactant nanoemulsions also resulted in greater uptake in Jurkat cells (Fig. 4.3A). Uptake was comparable for nanoemulsions irrespective of the method of incorporation (i.e., direct insertion or post-insertion, Fig. 4.3A). The 'optimal' incubation time was approximately 18 hours for 0.15 mol% phospholipid-TAT-PFC resulting in 1.23 (±0.85) $\times 10^{12}$ ^{19}F/cell. Shorter incubation times of 2 and 4 hours displayed lower uptake of 6.32 (±0.86) $\times 10^{11}$ ^{19}F/cell and 5.15 (±1.06) $\times 10^{11}$ ^{19}F/cell, respectively (Fig. 4.S3A). Following 18 hours of incubation, a modest reduction in cell viability was noticed and measured to be 79 (±5.65) % for phospholipid-TAT-PFC compared to 93.5 (±0.71) % for control nanoemulsion (Fig. 4.S3B). To test dose-dependent uptake, phospholipid-TAT-PFC (0.15 mol % of EYP) nanoemulsion were incubated with Jurkat cells for 18 hours at varying doses of 2.5, 5, 10 and 20 mg/mL. Uptake values followed a sigmoidal increase where cell uptake saturated at a dose of 10-15 mg/mL (Fig. 4.3B), with minimal loss in cell viability even at high doses (Fig. 4.3C).

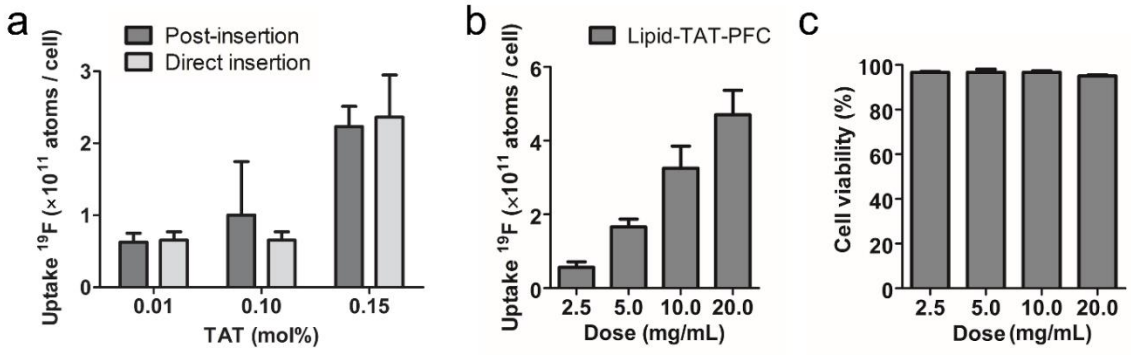

Figure 4.3. Jurkat cell labeling with lipid-TAT-PFC emulsion. The TAT anchor stoichiometry is optimized by measuring uptake (**a**) in cells while varying the percent by molarity of TAT in phospholipid surfactant PFC nanoemulsions using two different methods of preparation including post-insertion (dark grey) and direct insertion (light grey) of TAT conjugate. The cell uptake (**b**) and viability (**c**) with varying dosage of 0.1 mol% lipid-TAT-PFC after 18 hour incubation are presented.

We next investigated cellular localization of TATP- and TATA-F68-PFC nanoemulsions in primary T cells using high-resolution fluorescence and electron microscopy. We synthesized fluorescently labeled co-surfactants **8** and **9** consisting of Cy5 dye attached to the respective fluorous anchors (Fig. 4.S4) for incorporation into TATP-F68-PFC and TATA-F68-PFC nanoemulsions, respectively. Confocal microscopy of CAR T cells incubated with fluorescent nanoemulsions reveal intracellular and partial cell membrane localization of nanoemulsion (Fig. 4.4B) compared to untreated control cells (Fig. 4.4A); cells were co-stained with Hoechst nuclei stain and anti-CD3 fluorescent antibody for cell surface. As a further control, we tested whether the introduction of a surface dye on nanoemulsions enhanced cell uptake or causes overt cytotoxicity (Fig. 4.S5). The uptake of nanoemulsions formulated with dye co-surfactant are comparable to TATP-F68-PFC ($p>0.05$, Fig. 4.S5A), retains cell viability (Fig. 4.S5B), and compounds **8** and **9** do not appear to enhance internalization into live cells (Fig. 4.S6).

To substantiate the intracellular localization of TAT nanoemulsion in CAR T cells, electron microscopy was performed. The TATP-F68-PFC nanoemulsion droplets are present intracellularly and appear as clusters of small (~100-200 nm) punctate regions of hyperintensity in micrographs (Figs. 4.4E, F), along with a few larger PFC deposits (~1 μm) (Figs. 4.4G, H), presumably coalesced droplets, consistent with previous studies[29, 36]. Untreated control cells did not contain these hyperintense features in micrographs (Figs. 4.4C, D). Similar findings were observed for CAR T cells labeled with TATA-F68-naPFC nanoemulsion (Figs. 4.4I-L). Normal cellular, mitochondrial and Golgi body morphologies are observed, consistent with minimal toxicity to labeled CAR T cells (Figs. 4.4E, L)[37].

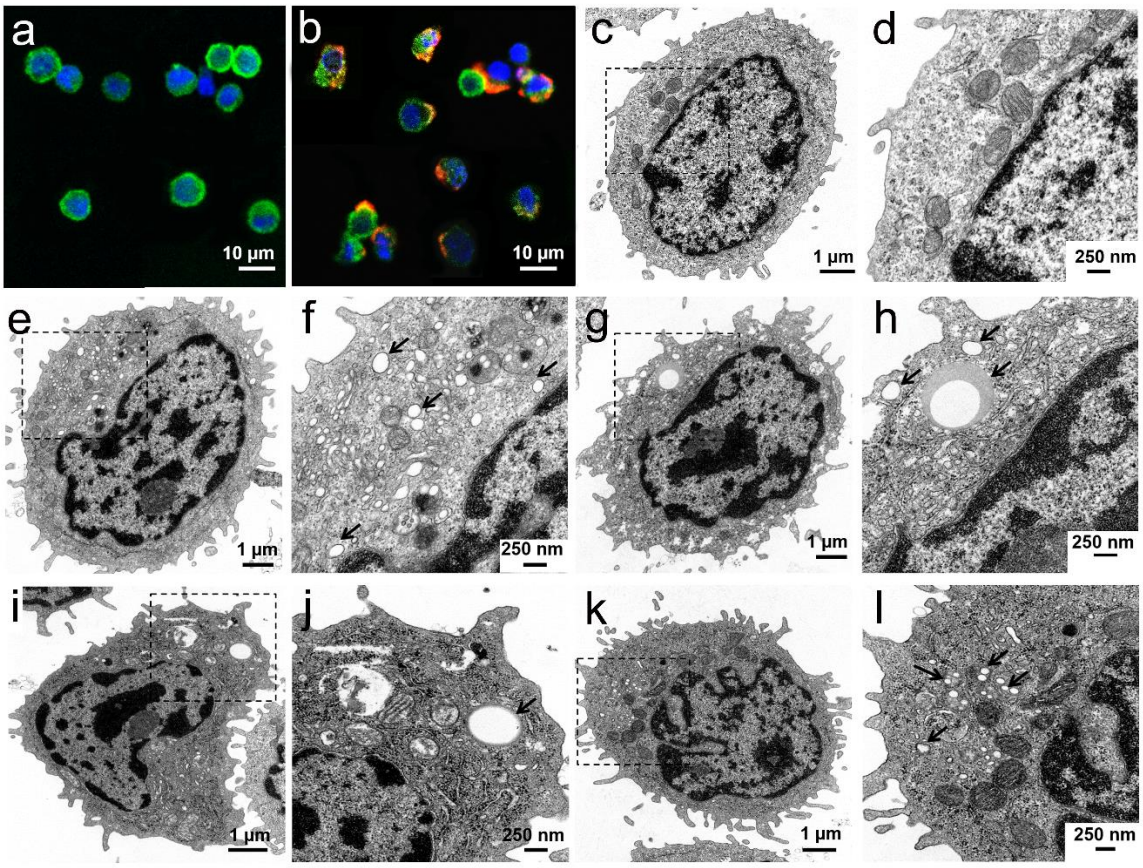

Figure 4.4. Microscopy of CAR T cells labeled with TAT-F68-PFC nanoemulsions. Confocal microscopy images of untreated CAR T cells are displayed in (**a**), and CAR T cells labeled with (15 mg/mL) of Cy5-TATP-F68-PFC nanoemulsions (red) are shown in (**b**). Data show intracellular localization of Cy5-TATP-F68-PFC emulsion, where Hoescht dye (blue) stains nuclei and Alexa488 anti-human CD3 antibody (green) delineates cell membrane. Electron microscopy of untreated CAR T cells is shown in (**c**)**,** magnified in (**d**). CAR T labeled with TATP-F68-PFC (**e-h**) show numerous bright ~100 nm nanoemulsion droplets (**e,** magnified in **f**, arrows) and occasional ~1 µm coalesced droplets (**g,** magnified in **h**, arrows). CAR T cells labeled with TATA-F68-PFC (**i-l**) shows similar emulsion droplets as with TATP-F68-PFC emulsion. Large coalesced droplets (**i**, inset **j**) as well as numerous smaller droplets (**k**, inset **l**) are found in the cytoplasm.

Expression of CD3, CD4 and CD8 CAR T cell surface markers is not altered by uptake of TATA-F68-PFC and TATP-F68-PFC nanoemulsions via flow cytometry (Fig. 4.5). Furthermore, CAR T cell killing function against glioma cells remains intact following labeling with TATP-F68-PFC nanoemulsion (Fig. 4.S7).

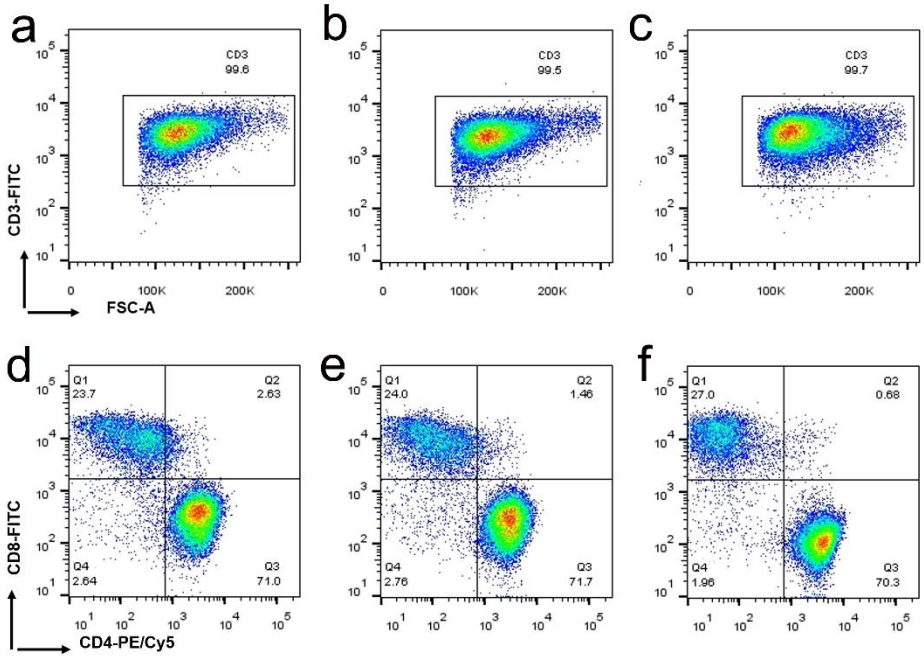

Figure 4.5. Phenotype of CAR T cells labeled with TAT-F68-PFC nanoemulsions. Scatter plots confirm pure population of CAR T cells (CD3) (**a-c**). CD3 expression is unaltered after labeling with TATP-F68-PFC (**a**) or TATA-F68-PFC (**b**) nanoemulsions compared to unlabeled cells (**c**)**.** Flow analysis for expression of CD4/CD8 shows a ~ 90/10 ratio of CD4+ to CD8+ positive cells (**d-f**). CAR T cells labeled with TATP-F68-PFC (**d**) or TATA-F68-PFC (**e**) *ex vivo* exhibit comparable phenotype to unlabeled cells (**f**). FSC-A indicates forward scatter, FITC stands for fluorescein isothiocyanate, and PE/Cy5 stands for phycoerythrin-cyanine 5.

To demonstrate the utility of TAT PFC nanoemulsion for *in vivo* MRI, we investigated ^{19}F signal detection from CAR T cells implanted into a rodent model. Mice bearing bilateral flank glioma tumors were injected intra-tumorally with CAR T cells (1×10^7 cells) labeled with either TATP-F68-PFC or F68-PFC (control) nanoemulsion. Figures 4.6A,

B display spin-density weighted ^{19}F images (pseudo-color) of injected cells, along with T_2-weighted ^{1}H images (grayscale) showing tumors in flanks. Qualitative analysis of MRI slices revealed greater number of high intensity pixels for TAT-F68-PFC-labeled CAR T cells compared to F68-PFC-labeled CAR T cells and noise (Fig. 4.6C). With aid of the calibrated ^{19}F reference in the image field of view, quantification of the three-dimensional ^{19}F images was performed (Fig. 4.6D); the right and left tumors display 17.9 (±2.1) $\times 10^{18}$ and 2.1 (±0.2) $\times 10^{18}$ ^{19}F atoms per tumor, respectively, revealing a significant ($p<0.01$) 8.5-fold sensitivity improvement in detection of CAR T cells labeled with TAT PFC nanoemulsion. This sensitivity increase is predicted, based on uptake analysis by ^{19}F NMR of pelleted cells prior to injection, showing ~8.2-fold increase in average fluorine content per cell for TATP-F68-PFC versus control nanoemulsion. Of note, the ^{19}F/cell measured after labeling was observed to be greater for CAR T cells compared to the Jurkat cell line, ~8.2-fold and ~5-fold (Fig. 4.2C, E), respectively, when both are labeled with TATP-F68-PFC nanoemulsion. Tumors were resected after imaging to verify intratumoral delivery of CAR T cells via extremely high-resolution *ex vivo* MRI (Figs. 4.6E, F, 4.S8).

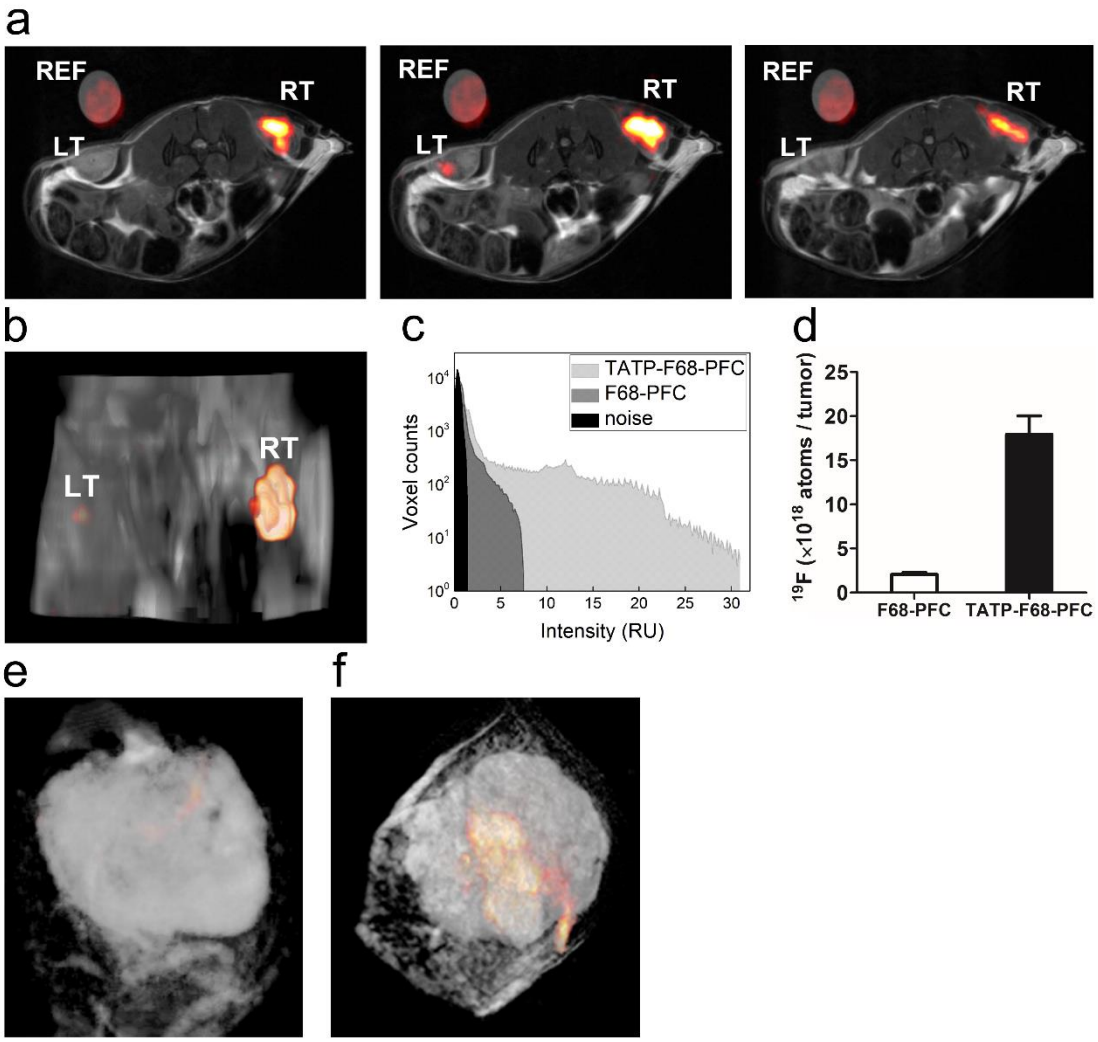

Figure 4.6. ***In vivo*** **^{19}F MRI signal enhancement in TATP-F68-PFC labeled human CAR T cells.** Panel (**a**) displays composite ^{19}F (hot-iron pseudo-color) and ^{1}H (grayscale) contiguous slices of a mouse with bilateral gliomas in the flanks, where the left and right tumor (LT, RT) each received 1×10^{7} CAR T cells labeled with either F68-PFC (control) or TATP-F68-PFC nanoemulsions, respectively. An external capillary reference (REF) is also shown in the field of view consisting of 1:20 dilution of F68-PFC in agarose. Panel (**b**) displays a three-dimensional rendering of the MRI data shown in (**a**). A histogram of the ^{19}F signal-to-noise ratio for each image voxel in the tumors is displayed in (**c**) and shows sensitivity improvement of the TATP-containing nanoemulsion compared to control. Comparison of apparent ^{19}F atoms per tumor, as measured *in vivo* for N = 4 mice, is displayed in (**d**) showing ~8 fold sensitivity enhancement ($p<0.001$) for TAT-F68-PFC nanoemulsions compared to control. To verify intratumoral delivery of CAR T cells, two days after CAR T cell injection, tumors were excised and fixed for extremely high-resolution MRI. Panels (**e**, **f**) show composite ^{19}F/^{1}H three-dimensional rendering of intratumoral CAR T cells labeled with control and TAT-F68-PFC nanoemulsions, respectively, and shows successful delivery.

4.4. Discussion

Fluorine-19 MRI methods have shown promise for the detection of cell therapy products post-transfer[15-20, 38, 39], inflammatory infiltrates[23, 40-42] and molecular targets[43] *in vivo* in preclinical models. Moreover, first-generation ^{19}F probes based on PFC nanoemulsions have been used in a pilot clinical trial[14], with additional trials planned[44]. Overall, the utility of ^{19}F MRI could be expanded by increasing the sensitivity of ^{19}F probes via molecular design. Towards this goal, we aim to increase the cell adhesion and resulting endocytosis of PFC nanoemulsions by non-phagocytic cells, especially engineered lymphocytes with therapeutic potential. We synthesized three different surfactant-anchored cell penetrating TAT peptides using small molecules that either mimic the common surfactants used in emulsion formulations, namely phospholipids and poloxamers, or the fluorous environment of the nanoemulsion droplet. We compared the efficacy of poloxamer and phospholipid based surfactants doped with TAT-conjugates and investigated nanoemulsion formation, droplet size, stability, cell uptake and viability *ex vivo*. Overall, nanoemulsions harboring TAT peptides led to a 4- to 8-fold cell loading improvement in T cells compared to the corresponding unmodified nanoemulsions. The droplet size, charge and initial cell safety was generally unaffected by the presence of TAT, presumably due to the low TAT to surfactant ratio in the nanoemulsions.

Phospholipid surfactants are often chosen to mimic the membranes of live cells and impart biocompatibility.[45, 46] Nonetheless, phospholipid-formulated nanoemulsions are prone to instability under storage conditions due to oxidation-mediated changes to the lipid[47], and lipid oxidation by-products may lead to cytotoxicity upon cell contact[48]. Indeed, a recent study has shown that formulations of lipid-surfactant paramagnetic nanoemulsions

that incorporate iron(III) bound to a fluorous diketonate (FDK) are prone to fatty acyl chain oxidative damage[49, 50]. Additionally, the formulation of phospholipid-based nanoemulsions requires a time consuming multi-step chemical process. For these reasons, we investigated the novel TAT conjugates for use with synthetic polymeric co-surfactants such as poloxamers (*e.g.*, F68) in detail.

Direct conjugation of TAT to the pluronic F68 (TAT-F68) as a co-surfactant resulted in nanoemulsion instability (data not shown), thus instead we conjugated TAT to short linear fluorous molecules via a short aliphatic hydrocarbon linker. The nanoemulsions prepared with TATP (**1a**) or TATA (**2a**) were stable for several months at 4 ^{o}C (Fig. S2).

As anticipated, increasing the percentage of TAT on the surface of the nanoemulsions enhanced cell uptake. However, levels >20 % w/w of TAT to pluronic surfactant resulted in increased cell-cell adhesion with formation of large cell clumps during labeling *in vitro*, thus a lower percent of TAT was used for further studies.

To validate internalization of the TAT nanoemulsions into CAR T cells, we prepared a comparable probe modified by the addition of a Cy5 fluorescent conjugate. The addition of this moiety did not alter the overall ^{19}F uptake levels in T cells. Fluorescence microscopy of labeled cells shows that nanoemulsion droplets are present at the cell membrane and in the cytosol, perhaps in endosomal compartments and in various stages of internalization and cellular processing in early to late endosomes[51]. It has been noted that the TAT peptide can translocate nanoparticles to the nucleus[52, 53], however, in our imaging studies we did not find nuclear localization of the TAT nanoemulsion probe. We note that TATP-F68-PFC-labeled cells can optionally be washed with a diluted trypsin solution to assist with removal of surface-adhered TAT emulsion. Nonetheless, presumably given sufficient time for

incubation, complete endocytosis of any membrane-bound TAT nanoemulsion should occur. Definitive evidence for internalized nanoemulsions in small (~100-200 nm) to large vesicles (~1 μm) was provided by electron microscopy. We speculate that small vesicles eventually coalesce into larger ones to minimize their hydrophobic surface area in contact with the aqueous cytosol, as cells have no mechanism for metabolizing PFCs[54, 55].

While the exact mechanism of TAT- and other CPP-mediated internalization into cells remains unknown[56], a substantial number of studies have been carried out to demonstrate its ability to drag a payload into the cytosol. CPPs' ability to translocate molecules of various sizes from small molecules[57], proteins[58], nucleic acids and liposomes[59], many of which have been studied *in vivo*[60], makes their use for nanoemulsions attractive, with adjustments in the amount of TAT required based on the cargo to be delivered[56]. In addition to the pre-clinical successes with TAT peptides[61-64], four compounds conjugated to TAT are currently being tested in the clinic[65] for conditions such as myocardial infarction[66], pain[67], hearing loss[68], and inflammation[69]; preliminary results of phase I clinical trials indicate that TAT peptides exhibit acceptable safety profiles.

Our *in vivo* model shows that CAR T cells carrying TAT functionalized emulsions give increased ^{19}F MRI signal when injected into a tumor. Intratumoral immune cell delivery has successfully shown anti-tumor effects in mice[70-72] and has been considered as an approach for patients[73] as it may minimize toxicity from cytokine release syndrome upon treatment with high doses of T cells. For example, Phase 1 trials are ongoing to test the efficacy of intratumoral delivery in humans with ErbB targeted T4+ T cells in recurrent head and neck cancer[74]. In another example, dendritic cells were isolated from patients and

injected intratumorally to induce an immune response[75]. Localized intrathecal delivery of natural killer cells to treat medulloblastoma in pediatric patients is also under investigation[76].

Overall, we have shown that incorporating the TAT cell penetrating peptide in PFC nanoemulsions significantly enhances cell uptake by lymphocytes and subsequently increased their detectability *in vivo* using ^{19}F MRI. These same agents should be useful for tagging other weakly phagocytic cells such as stem and progenitor cells. Moreover, the peptide-PFC nanoemulsion synthesis scheme presented is generalizable for a multitude of *ex vivo* and *in vivo* targeted ^{19}F MRI probes and offers new avenues for cellular-molecular imaging.

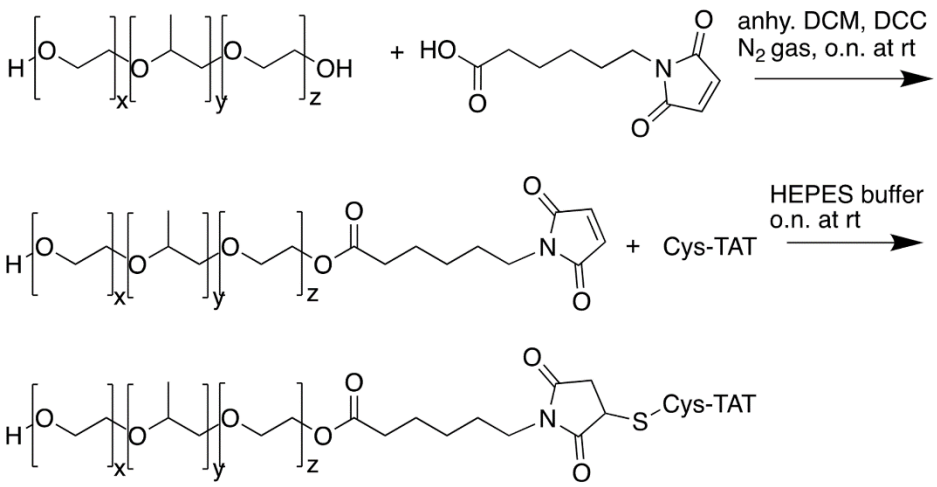

10 F68-TAT

Figure 4.S1. Synthesis scheme of F68-TAT co-surfactant. F68 is functionalized with a maleimide group to enable addition of the TAT peptide with a terminal cysteine (Cys-TAT).

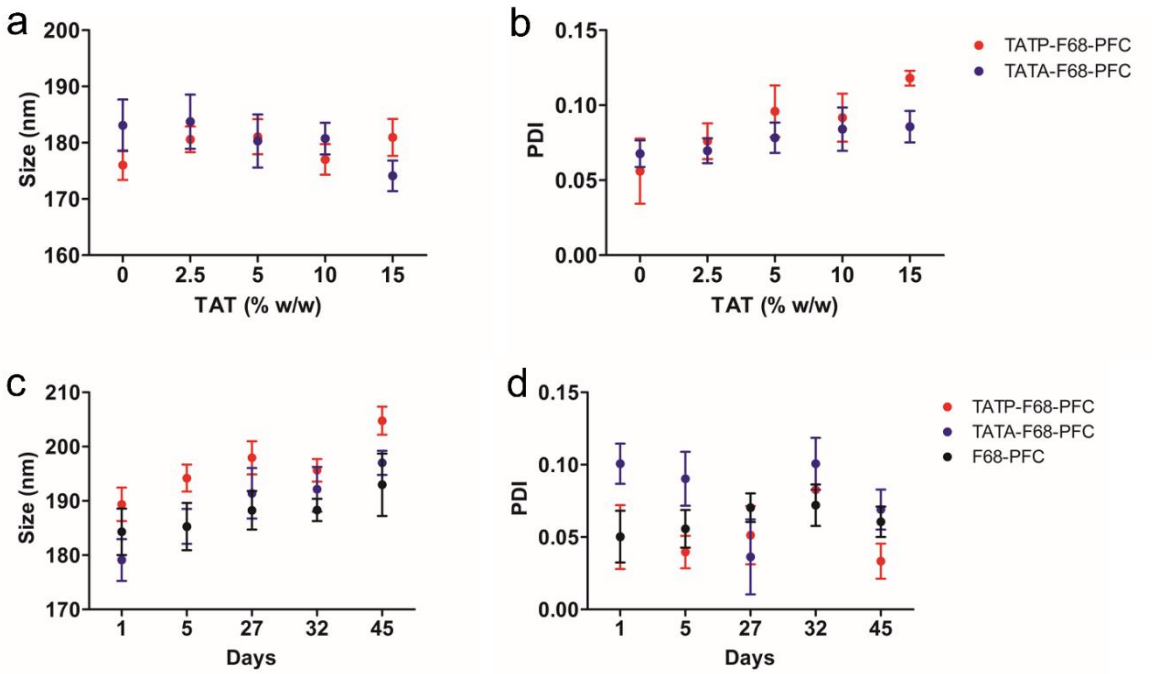

Figure 4.S2. Size stability of TAT-F68-PFC nanoemulsions. The effect of % TAT incorporation on size (**a**) and polydispersity index (PDI, **b**) of nanoemulsions is shown. The nanoemulsion size (**c**) and PDI (**d**) of nanoemulsions over time while stored at 4 ^{o}C is displayed.

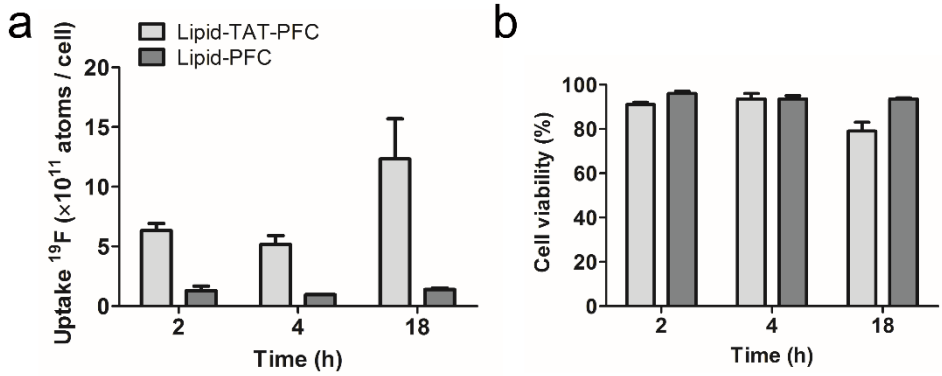

Figure 4.S3. Optimization of lipid-TAT-PFC incubation time in Jurkat cells. Incubation times of 2, 4 and 18 hours are tested as shown in (**a**), and the highest uptake is observed at 18 hours. Jurkat cell viability is not altered by labeling for different durations (**b**).

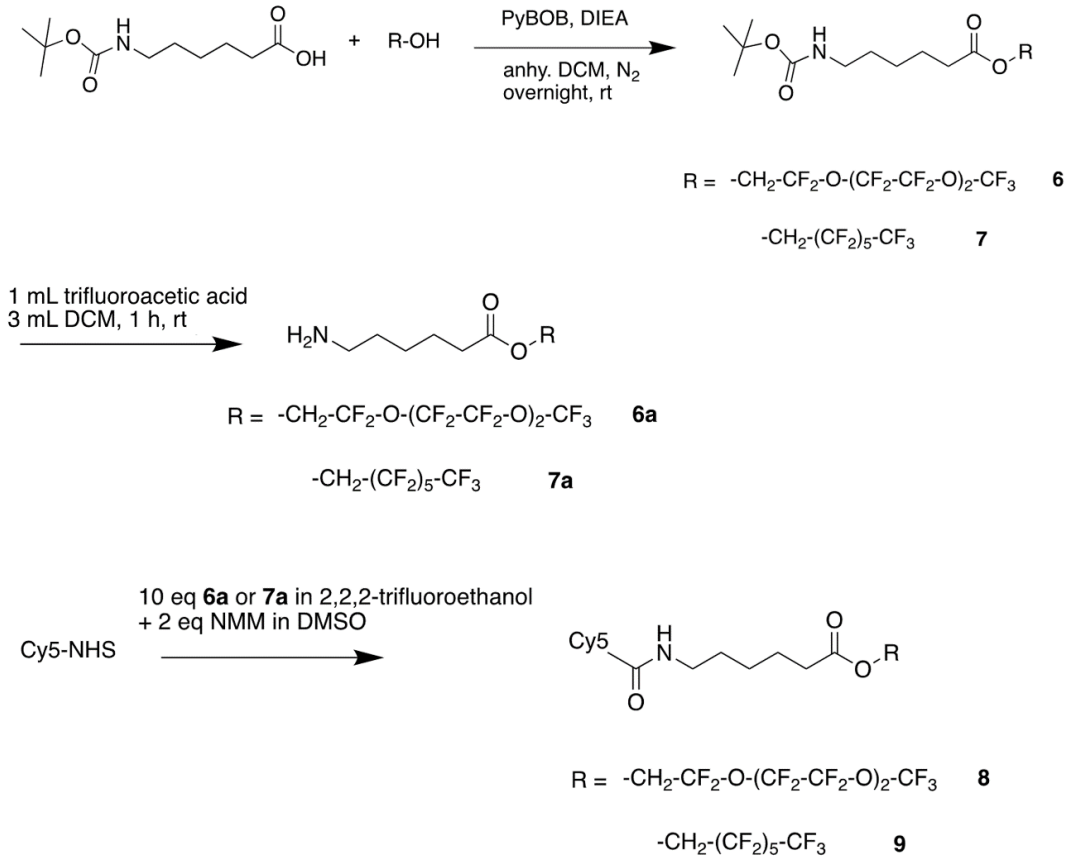

Figure 4.S4. Cy5-TATA,P-F68-PFC synthesis scheme. Scheme shows synthesis of fluorescently labeled co-surfactants **8** and **9** consisting of Cy5 dye attached to the respective fluorous anchors **6** and **7** for incorporation into TATP-F68-PFC and TATA-F68-PFC nanoemulsions, respectively.

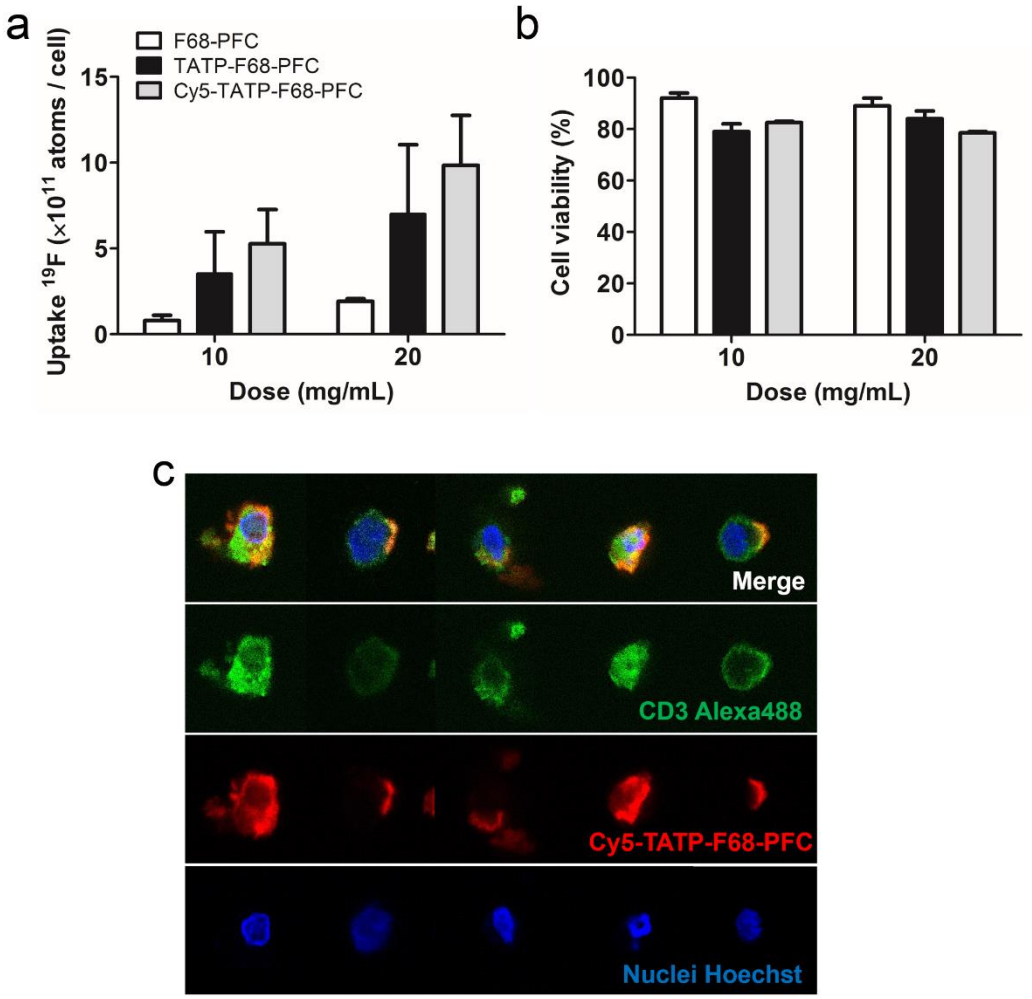

Figure 4.S5. Localization impact of incorporation of fluorescent dye into surfactant layer during nanoemulsion preparation. Panel (**a**) displays ^{19}F uptake for cells treated with nanoemulsions prepared with and without anchored Cy5 at 10 mg/mL and 20 mg/mL doses; no significant differences are observed. Additionally, CAR T cell viability is not affected as shown in (**b**). Panel (**c**) shows intracellular localization of the nanoemulsion (Cy5 in red) in CAR T cells via confocal microscopy. Hoescht dye (nuclei, blue) and Alexa488 dye (cell membrane, green) is used to delineate cell structures.

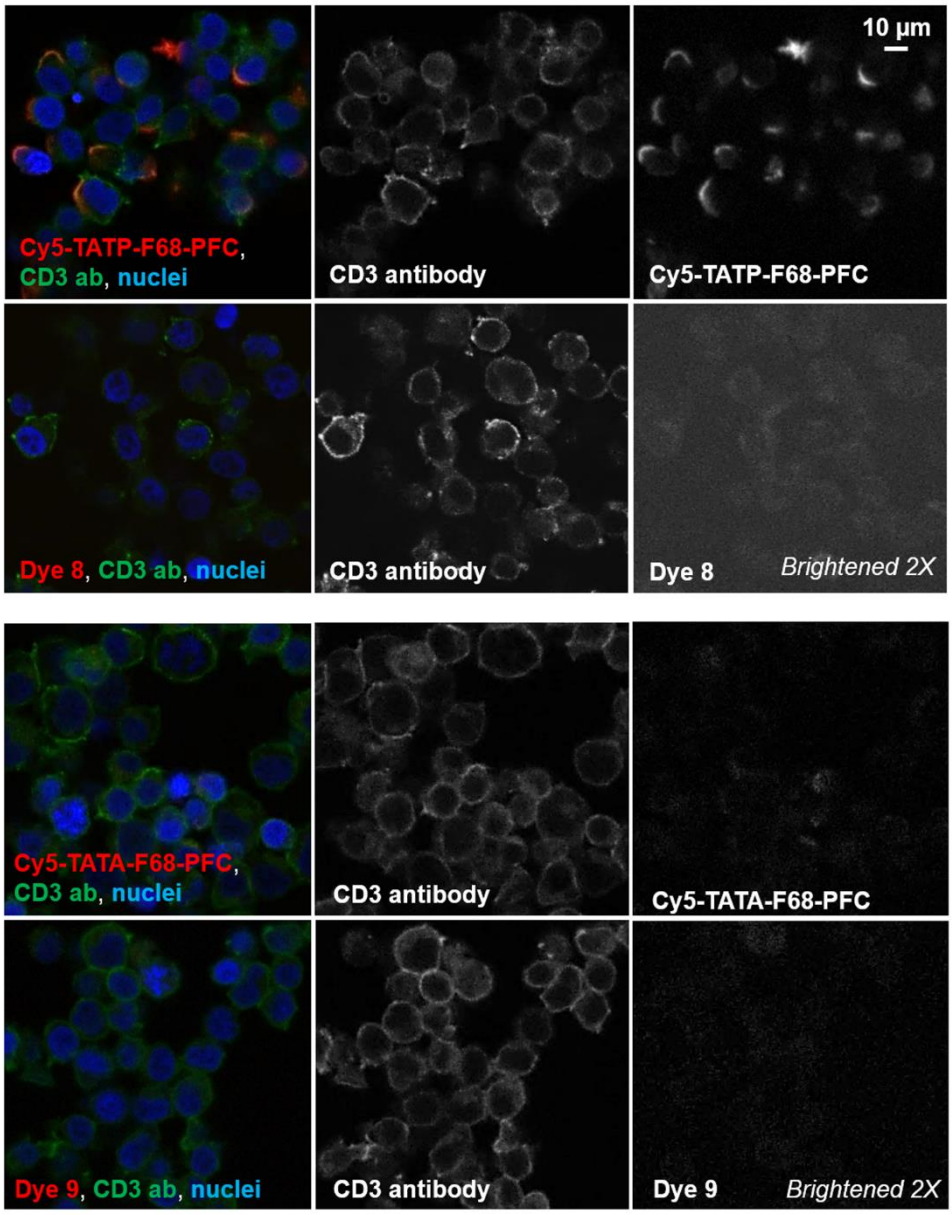

Figure 4.S6. Fluorescent dye conjugate nanoemulsions without TAT do not get internalized into CAR T cells. Panels show that dye compounds **8** and **9** do not induce non-specific internalization into live cells. Hoescht dye (nuclei, blue) and Alexa488 dye (cell membrane, green) are used to delineate the cells.

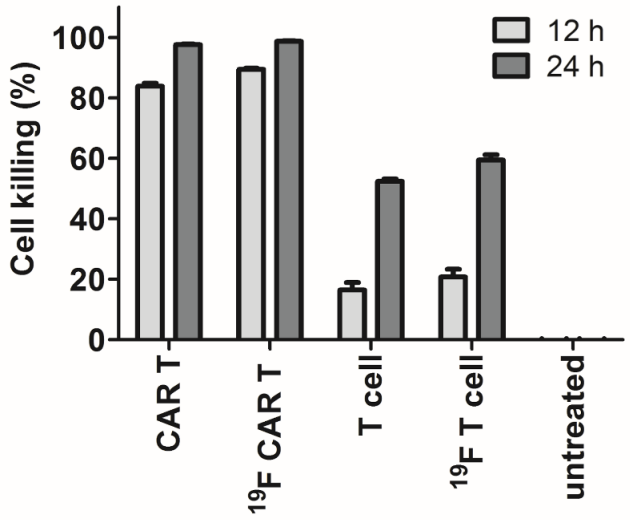

Figure 4.S7. CAR T cell killing assay *in vitro*. Co-incubation of human U87-EGFRvIII-Luc glioma cells with TATP-F68-PFC-labeled or unlabeled CAR T cells, or untransduced T cells results in significant cell death at 12 and 24 h. CAR T cells exhibit significant tumor killing ability (~ 98%) compared to untransduced T cells (~ 60%). Killing efficacy is unaltered by nanoemulsion labeling of the cells.

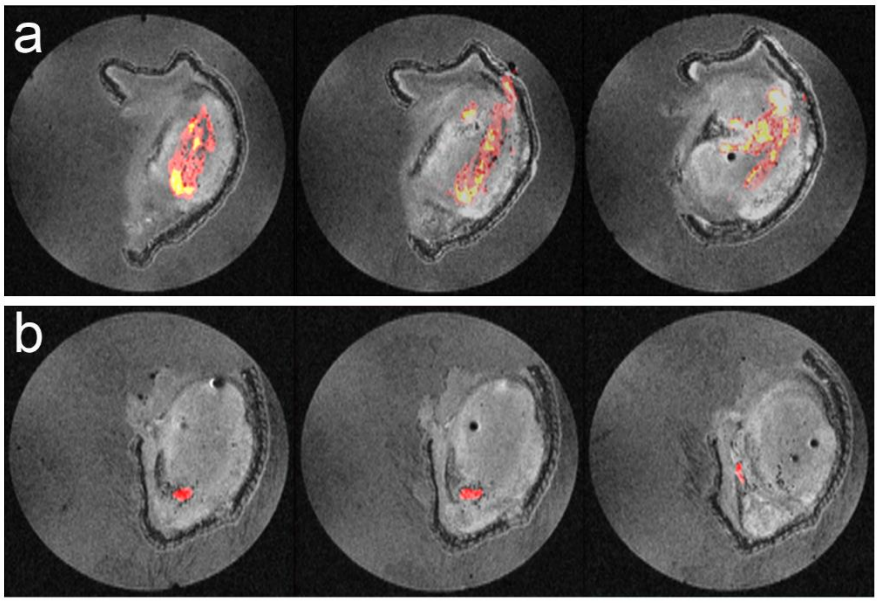

Figure 4.S8. *Ex vivo* 3D microimaging of excised glioma tumors harboring PFC labeled CAR T cells. Contiguous images show overlays of ^{19}F (pseudo-color) and ^{1}H (grayscale) slices of right tumor receiving an intratumoral injection of 10^7 TATP-F68-PFC labeled CAR T cells (**a**), and the left tumor with the same number of F68-PFC labeled CAR T cells (**b**).

Acknowledgements

Chapter 4, in full, contains text submitted for publication of the material. Hingorani D*, Chapelin F*, Stares E, Adams E, Okada H, Ahrens E.T. Cell Penetrating Peptide Functionalized Perfluorocarbon Nanoemulsions for Targeted Cell labeling and Enhanced Fluorine-19 MRI Detection *Authors contributed equally. The authors acknowledge technical support from Ms Hongyan Xu. The dissertation author was the primary investigator and author of this paper.

References

1. Kircher, M.F., Gambhir, S.S. & Grimm, J. Noninvasive cell-tracking methods. *Nature reviews Clinical oncology* **8**, 677 (2011).

2. Jha, P., Golovko, D., Bains, S., Hostetter, D., Meier, R., Wendland, M.F. & Daldrup-Link, H.E. Monitoring of natural killer cell immunotherapy using noninvasive imaging modalities. *Cancer research* **70**, 6109-6113 (2010).

3. June, C.H., O'Connor, R.S., Kawalekar, O.U., Ghassemi, S. & Milone, M.C. CAR T cell immunotherapy for human cancer. *Science* **359**, 1361-1365 (2018).

4. Townsend, M.H., Shrestha, G., Robison, R.A. & O'Neill, K.L. The expansion of targetable biomarkers for CAR T cell therapy. *J Exp Clin Cancer Res* **37**, 163 (2018).

5. Bonifant, C.L., Jackson, H.J., Brentjens, R.J. & Curran, K.J. Toxicity and management in CAR T-cell therapy. *Molecular Therapy-Oncolytics* **3** (2016).

6. Chang, Z.L. & Chen, Y.Y. CARs: synthetic immunoreceptors for cancer therapy and beyond. *Trends in molecular medicine* **23**, 430-450 (2017).

7. Hartmann, J., Schüßler-Lenz, M., Bondanza, A. & Buchholz, C.J. Clinical development of CAR T cells—challenges and opportunities in translating innovative treatment concepts. *EMBO molecular medicine*, e201607485 (2017).

8. Tarantal, A.F., Lee, C.C.I., Kukis, D.L. & Cherry, S.R. Radiolabeling human peripheral blood stem cells for positron emission tomography (PET) imaging in young rhesus monkeys. *PloS one* **8**, e77148 (2013).

9. Wolfs, E., Struys, T., Notelaers, T., Roberts, S.J., Sohni, A., Bormans, G., Van Laere, K., Luyten, F.P., Gheysens, O. & Lambrichts, I. 18F-FDG labeling of mesenchymal stem cells and multipotent adult progenitor cells for PET imaging: effects on ultrastructure and differentiation capacity. *Journal of Nuclear Medicine*, jnumed-112 (2013).

10. Wang, X., Rosol, M., Ge, S., Peterson, D., McNamara, G., Pollack, H., Kohn, D.B., Nelson, M.D. & Crooks, G.M. Dynamic tracking of human hematopoietic stem cell engraftment using in vivo bioluminescence imaging. *Blood* **102**, 3478-3482 (2003).

11. Xiong, T., Zhang, Z., Liu, B.-F., Zeng, S., Chen, Y., Chu, J. & Luo, Q. In vivo optical imaging of human adenoid cystic carcinoma cell metastasis. *Oral oncology* **41**, 709-715 (2005).

12. Giepmans, B.N.G., Adams, S.R., Ellisman, M.H. & Tsien, R.Y. The fluorescent toolbox for assessing protein location and function. *science* **312**, 217-224 (2006).

13. Ahrens, E.T. & Bulte, J.W. Tracking immune cells in vivo using magnetic resonance imaging. *Nature reviews. Immunology* **13**, 755-763 (2013).

14. Ahrens, E.T., Helfer, B.M., O'Hanlon, C.F. & Schirda, C. Clinical cell therapy imaging using a perfluorocarbon tracer and fluorine-19 MRI. *Magnetic resonance in medicine* **72**, 1696-1701 (2014).

15. Bouchlaka, M.N., Ludwig, K.D., Gordon, J.W., Kutz, M.P., Bednarz, B.P., Fain, S.B. & Capitini, C.M. (19)F-MRI for monitoring human NK cells in vivo. *Oncoimmunology* **5**, e1143996 (2016).

16. Fink, C., Gaudet, J.M., Fox, M.S., Bhatt, S., Viswanathan, S., Smith, M., Chin, J., Foster, P.J. & Dekaban, G.A. (19)F-perfluorocarbon-labeled human peripheral blood mononuclear cells can be detected in vivo using clinical MRI parameters in a therapeutic cell setting. *Scientific reports* **8**, 590 (2018).

17. Janjic, J.M. & Ahrens, E.T. Fluorine-containing nanoemulsions for MRI cell tracking. *Wiley interdisciplinary reviews. Nanomedicine and nanobiotechnology* **1**, 492-501 (2009).

18. Ku, M.C., Edes, I., Bendix, I., Pohlmann, A., Waiczies, H., Prozorovski, T., Gunther, M., Martin, C., Pages, G., Wolf, S.A., Kettenmann, H., Uckert, W., Niendorf, T. & Waiczies, S. ERK1 as a Therapeutic Target for Dendritic Cell Vaccination against High-Grade Gliomas. *Molecular cancer therapeutics* **15**, 1975-1987 (2016).

19. Somanchi, S.S., Kennis, B.A., Gopalakrishnan, V., Lee, D.A. & Bankson, J.A. In Vivo (19)F-Magnetic Resonance Imaging of Adoptively Transferred NK Cells. *Methods in molecular biology* **1441**, 317-332 (2016).

20. Srinivas, M., Turner, M.S., Janjic, J.M., Morel, P.A., Laidlaw, D.H. & Ahrens, E.T. In vivo cytometry of antigen-specific t cells using 19F MRI. *Magnetic resonance in medicine* **62**, 747-753 (2009).

21. Waiczies, H., Lepore, S., Janitzek, N., Hagen, U., Seifert, F., Ittermann, B., Purfurst, B., Pezzutto, A., Paul, F., Niendorf, T. & Waiczies, S. Perfluorocarbon Particle Size Influences Magnetic Resonance Signal and Immunological Properties of Dendritic Cells. *PLoS ONE* **6** (2011).

22. Xander Staal, O.K., Mangala Srinivas in Fluorine in Life Sciences: Pharmaceuticals, Medicinal Diagnostics, and Agrochemicals. (ed. F.R.L. Günter Haufe) (2019).

23. Khurana, A., Chapelin, F., Xu, H., Acevedo, J.R., Molinolo, A., Nguyen, Q. & Ahrens, E.T. Visualization of macrophage recruitment in head and neck carcinoma model using fluorine-19 magnetic resonance imaging. *Magnetic resonance in medicine* **79**, 1972-1980 (2018).

24. Ruiz-Cabello, J., Barnett, B.P., Bottomley, P.A. & Bulte, J.W.M. Fluorine (19F) MRS and MRI in biomedicine. *NMR in Biomedicine* **24**, 114-129 (2011).

25. Lim, W.A. & June, C.H. The Principles of Engineering Immune Cells to Treat Cancer. *Cell* **168**, 724-740 (2017).

26. Lindgren, M., Hällbrink, M., Prochiantz, A. & Langel, Ü. Cell-penetrating peptides. *Trends in pharmacological sciences* **21**, 99-103 (2000).

27. Vives, E., Brodin, P. & Lebleu, B. A truncated HIV-1 Tat protein basic domain rapidly translocates through the plasma membrane and accumulates in the cell nucleus. *Journal of Biological Chemistry* **272**, 16010-16017 (1997).

28. Jacoby, C., Temme, S., Mayenfels, F., Benoit, N., Krafft, M.P., Schubert, R., Schrader, J. & Flogel, U. Probing different perfluorocarbons for in vivo inflammation imaging by 19F MRI: image reconstruction, biological half-lives and sensitivity. *NMR Biomed* **27**, 261-271 (2014).

29. Ahrens, E.T., Flores, R., Xu, H. & Morel, P.A. In vivo imaging platform for tracking immunotherapeutic cells. *Nature biotechnology* **23**, 983-987 (2005).

30. Johnson, L.A., Scholler, J., Ohkuri, T., Kosaka, A., Patel, P.R., McGettigan, S.E., Nace, A.K., Dentchev, T., Thekkat, P. & Loew, A. Rational development and characterization of humanized anti–EGFR variant III chimeric antigen receptor T cells for glioblastoma. *Science translational medicine* **7**, 275ra222-275ra222 (2015).

31. Chapelin, F., Gao, S., Okada, H., Weber, T.G., Messer, K. & Ahrens, E.T. Fluorine-19 nuclear magnetic resonance of chimeric antigen receptor T cell biodistribution in murine cancer model. *Scientific reports* **7**, 17748 (2017).

32. Ohno, M., Ohkuri, T., Kosaka, A., Tanahashi, K., June, C.H., Natsume, A. & Okada, H. Expression of miR-17-92 enhances anti-tumor activity of T-cells transduced with the anti-EGFRvIII chimeric antigen receptor in mice bearing human GBM xenografts. *J Immunother Cancer* **1**, 21 (2013).

33. Srinivas, M., Morel, P.A., Ernst, L.A., Laidlaw, D.H. & Ahrens, E.T. Fluorine-19 MRI for visualization and quantification of cell migration in a diabetes model. *Magnetic resonance in medicine* **58**, 725-734 (2007).

34. Howard, M.D., Hood, E.D., Greineder, C.F., Alferiev, I.S., Chorny, M. & Muzykantov, V. Targeting to endothelial cells augments the protective effect of novel dual bioactive antioxidant/anti-inflammatory nanoparticles. *Molecular pharmaceutics* **11**, 2262-2270 (2014).

35. Hu, S., Wang, T., Pei, X., Cai, H., Chen, J., Zhang, X., Wan, Q. & Wang, J. Synergistic Enhancement of Antitumor Efficacy by PEGylated Multi-walled Carbon Nanotubes Modified with Cell-Penetrating Peptide TAT. *Nanoscale Res Lett* **11**, 452 (2016).

36. Hitchens, T.K., Liu, L., Foley, L.M., Simplaceanu, V., Ahrens, E.T. & Ho, C. Combining perfluorocarbon and superparamagnetic iron-oxide cell labeling for improved and expanded applications of cellular MRI. *Magnetic resonance in medicine* **73**, 367-375 (2015).

37. van Eeden, S.F., Klut Me Fau - Leal, M.A., Leal Ma Fau - Alexander, J., Alexander J Fau - Zonis, Z., Zonis Z Fau - Skippen, P. & Skippen, P. Partial liquid ventilation with perfluorocarbon in acute lung injury: light and transmission electron microscopy studies.

38. Chapelin, F., Gao, S., Okada, H., Weber, T.G., Messer, K. & Ahrens, E.T. Fluorine-19 nuclear magnetic resonance of chimeric antigen receptor T cell biodistribution in murine cancer model. *Scientific Reports* **7** (2017).

39. Gonzales, C., Yoshihara, H.A., Dilek, N., Leignadier, J., Irving, M., Mieville, P., Helm, L., Michielin, O. & Schwitter, J. In-Vivo Detection and Tracking of T Cells in Various Organs in a Melanoma Tumor Model by 19F-Fluorine MRS/MRI. *PLoS One* **11**, e0164557 (2016).

40. Ahrens, E.T., Young, W.B., Xu, H. & Pusateri, L.K. Rapid quantification of inflammation in tissue samples using perfluorocarbon emulsion and fluorine-19 nuclear magnetic resonance. *Biotechniques* **50**, 229-234 (2011).

41. Kadayakkara, D.K., Ranganathan, S., Young, W.B. & Ahrens, E.T. Assaying macrophage activity in a murine model of inflammatory bowel disease using fluorine-19 MRI. *Lab Invest* **92**, 636-645 (2012).

42. Zhong, J., Narsinh, K., Morel, P.A., Xu, H. & Ahrens, E.T. In Vivo Quantification of Inflammation in Experimental Autoimmune Encephalomyelitis Rats Using

Fluorine-19 Magnetic Resonance Imaging Reveals Immune Cell Recruitment outside the Nervous System. *PLoS One* **10**, e0140238 (2015).

43. Temme, S., Grapentin, C., Quast, C., Jacoby, C., Grandoch, M., Ding, Z., Owenier, C., Mayenfels, F., Fischer, J.W., Schubert, R., Schrader, J. & Flogel, U. Noninvasive Imaging of Early Venous Thrombosis by 19F Magnetic Resonance Imaging With Targeted Perfluorocarbon Nanoemulsions. *Circulation* **131**, 1405-1414 (2015).

44. Bulte, J.W.M. & Daldrup-Link, H.E. Clinical Tracking of Cell Transfer and Cell Transplantation: Trials and Tribulations. *Radiology* **289**, 604-615 (2018).

45. Grapentin, C.M., Friederike; Barnert, Sabine; A Süss, Regine; Schubert, Rolf; Temme, Sebastian; Jacoby, Christoph; Schrader, Juergen; Flögel, Ulrich (2015).

46. Temme, S., Baran, P., Bouvain, P., Grapentin, C., Kramer, W., Knebel, B., Al-Hasani, H., Moll, J.M., Floss, D., Schrader, J., Schubert, R., Flogel, U. & Scheller, J. Synthetic Cargo Internalization Receptor System for Nanoparticle Tracking of Individual Cell Populations by Fluorine Magnetic Resonance Imaging. *ACS Nano* **12**, 11178-11192 (2018).

47. Girotti, A.W. Mechanisms of lipid peroxidation. *Journal of free radicals in biology & medicine* **1**, 87-95 (1985).

48. Schaich, K.M. Metals and lipid oxidation. Contemporary issues. *Lipids* **27**, 209-218 (1992).

49. Kislukhin, A.A., Xu, H., Adams, S.R., Narsinh, K.H., Tsien, R.Y. & Ahrens, E.T. Paramagnetic fluorinated nanoemulsions for sensitive cellular fluorine-19 magnetic resonance imaging. *Nature materials* **15**, 662 (2016).

50. Rho, J.S., E; Adams, S.R; Zhu, W; Ahrens, E.T (2019).

51. Fretz, M., Jin, J., Conibere, R., Penning, N.A., Al-Taei, S., Storm, G., Futaki, S., Takeuchi, T., Nakase, I. & Jones, A.T. Effects of Na+/H+ exchanger inhibitors on subcellular localisation of endocytic organelles and intracellular dynamics of protein transduction domains HIV–TAT peptide and octaarginine. *Journal of controlled release* **116**, 247-254 (2006).

52. Vives, E., Brodin P Fau - Lebleu, B. & Lebleu, B. A truncated HIV-1 Tat protein basic domain rapidly translocates through the plasma membrane and accumulates in the cell nucleus.

53. de la Fuente, J.M. & Berry, C.C. Tat peptide as an efficient molecule to translocate gold nanoparticles into the cell nucleus.

54. Krafft, M.P. Fluorocarbons and fluorinated amphiphiles in drug delivery and biomedical research. *Adv Drug Deliv Rev* **47**, 209-228 (2001).

55. Krafft, M.P. & Riess, J.G. Perfluorocarbons: Life sciences and biomedical uses - Dedicated to the memory of Professor Guy Ourisson, a true RENAISSANCE man. *J Polym Sci Pol Chem* **45**, 1185-1198 (2007).

56. Brooks, H., Lebleu, B. & Vivès, E. Tat peptide-mediated cellular delivery: back to basics. *Advanced drug delivery reviews* **57**, 559-577 (2005).

57. Mazel, M., Clair, P., Rousselle, C., Vidal, P., Scherrmann, J.-M., Mathieu, D. & Temsamani, J. Doxorubicin-peptide conjugates overcome multidrug resistance. *Anti-cancer drugs* **12**, 107-116 (2001).

58. Fawell, S., Seery, J., Daikh, Y., Moore, C., Chen, L.L., Pepinsky, B. & Barsoum, J. Tat-mediated delivery of heterologous proteins into cells. *Proceedings of the National Academy of Sciences* **91**, 664-668 (1994).

59. Torchilin, V.P., Levchenko, T.S., Rammohan, R., Volodina, N., Papahadjopoulos-Sternberg, B. & D'Souza, G.G.M. Cell transfection in vitro and in vivo with nontoxic TAT peptide-liposome–DNA complexes. *Proceedings of the National Academy of Sciences* **100**, 1972-1977 (2003).

60. Foged, C. & Nielsen, H.M. Cell-penetrating peptides for drug delivery across membrane barriers. *Expert opinion on drug delivery* **5**, 105-117 (2008).

61. Boisguerin, P., Redt-Clouet, C., Franck-Miclo, A., Licheheb, S., Nargeot, J., Barrère-Lemaire, S. & Lebleu, B. Systemic delivery of BH4 anti-apoptotic peptide using CPPs prevents cardiac ischemia–reperfusion injuries in vivo. *Journal of controlled release* **156**, 146-153 (2011).

62. Borsello, T., Clarke, P.G.H., Hirt, L., Vercelli, A., Repici, M., Schorderet, D.F., Bogousslavsky, J. & Bonny, C. A peptide inhibitor of c-Jun N-terminal kinase protects against excitotoxicity and cerebral ischemia. *Nature medicine* **9**, 1180 (2003).

63. Michiue, H., Eguchi, A., Scadeng, M. & Dowdy, S.F. Induction of in vivo synthetic lethal RNAi responses to treat glioblastoma. *Cancer biology & therapy* **8**, 2304-2311 (2009).

64. Yang, D., Sun, Y.-Y., Lin, X., Baumann, J.M., Dunn, R.S., Lindquist, D.M. & Kuan, C.-Y. Intranasal delivery of cell-penetrating anti-NF-κB peptides (Tat-NBD) alleviates infection-sensitized hypoxic–ischemic brain injury. *Experimental neurology* **247**, 447-455 (2013).

65. Direct Inhibition of delta-Protein Kinase, C.E.t.L.T.I.S.i.A.M.I.I., Bates, E., Bode, C., Costa, M., Gibson, C.M., Granger, C., Green, C., Grimes, K., Harrington, R., Huber, K., Kleiman, N., Mochly-Rosen, D., Roe, M., Sadowski, Z., Solomon, S. & Widimsky, P. Intracoronary KAI-9803 as an adjunct to primary percutaneous coronary intervention for acute ST-segment elevation myocardial infarction. *Circulation* **117**, 886-896 (2008).

66. Cousins, M.J., Pickthorn, K., Huang, S., Critchley, L. & Bell, G. The safety and efficacy of KAI-1678- an inhibitor of epsilon protein kinase C (epsilonPKC)-versus lidocaine and placebo for the treatment of postherpetic neuralgia: a crossover study design. *Pain Med* **14**, 533-540 (2013).

67. Suckfuell, M., Lisowska, G., Domka, W., Kabacinska, A., Morawski, K., Bodlaj, R., Klimak, P., Kostrica, R. & Meyer, T. Efficacy and safety of AM-111 in the treatment of acute sensorineural hearing loss: a double-blind, randomized, placebo-controlled phase II study. *Otology & neurotology* **35**, 1317-1326 (2014).

68. Suckfuell, M., Lisowska, G., Domka, W., Kabacinska, A., Morawski, K., Bodlaj, R., Klimak, P., Kostrica, R. & Meyer, T. Efficacy and safety of AM-111 in the treatment of acute sensorineural hearing loss: a double-blind, randomized, placebo-controlled phase II study. *Otol Neurotol* **35**, 1317-1326 (2014).

69. Deloche, C., Lopez-Lazaro, L., Mouz, S., Perino, J., Abadie, C. & Combette, J.M. XG-102 administered to healthy male volunteers as a single intravenous infusion: a randomized, double-blind, placebo-controlled, dose-escalating study. *Pharmacology research & perspectives* **2**, e00020 (2014).

70. Tatsumi, T., Huang, J., Gooding, W.E., Gambotto, A., Robbins, P.D., Vujanovic, N.L., Alber, S.M., Watkins, S.C., Okada, H. & Storkus, W.J. Intratumoral delivery of dendritic cells engineered to secrete both interleukin (IL)-12 and IL-18 effectively treats local and distant disease in association with broadly reactive Tc1-type immunity. *Cancer research* **63**, 6378-6386 (2003).

71. Kennis, B.A., Michel, K.A., Brugmann, W.B., Laureano, A., Tao, R.H., Somanchi, S.S., Einstein, S.A., Bravo-Alegria, J.B., Maegawa, S., Wahba, A., Kiany, S., Gordon, N., Silla, L., Schellingerhout, D., Khatua, S., Zaky, W., Sandberg, D., Cooper, L., Lee, D.A., Bankson, J.A. & Gopalakrishnan, V. Monitoring of intracerebellarly-administered natural killer cells with fluorine-19 MRI. *J Neurooncol* **142**, 395-407 (2019).

72. Melero, I., Duarte, M., Ruiz, J., Sangro, B., Galofre, J., Mazzolini, G., Bustos, M., Qian, C. & Prieto, J. Intratumoral injection of bone-marrow derived dendritic cells engineered to produce interleukin-12 induces complete regression of established murine transplantable colon adenocarcinomas. *Gene Ther* **6**, 1779-1784 (1999).

73. Ngwa, W., Irabor, O.C., Schoenfeld, J.D., Hesser, J., Demaria, S. & Formenti, S.C. Using immunotherapy to boost the abscopal effect. *Nature Reviews Cancer* (2018).

74. van Schalkwyk, M.C.I., Papa, S.E., Jeannon, J.-P., Urbano, T.G., Spicer, J.F. & Maher, J. Design of a phase I clinical trial to evaluate intratumoral delivery of ErbB-targeted chimeric antigen receptor T-cells in locally advanced or recurrent head and neck cancer. *Human Gene Therapy Clinical Development* **24**, 134-142 (2013).

75. Triozzi, P.L., Khurram, R., Aldrich, W.A., Walker, M.J., Kim, J.A. & Jaynes, S. Intratumoral injection of dendritic cells derived in vitro in patients with metastatic cancer. *Cancer* **89**, 2646-2654 (2000).

76. https://clinicaltrials.gov/ct2/show/NCT02271711 (accessed 04/30-19)

Chapter 5: Magnetic resonance imaging monitoring of *in vivo* intracellular oximetry response to chimeric antigen receptor T cell immunotherapy against glioma

5.1. Introduction

Cancer is one of the leading causes of death worldwide. Despite unprecedented investments, cancer therapy research remains arduous and prevalent clinical benefit remains unfulfilled. Growing evidence suggests that the major obstacle for cancer therapy is the tumor microenvironment. Tumor mechanisms of immunosuppression generate chronic inflammation and hypoxia in its vicinity and results in increased tumor angiogenesis, recurrence, and malignant progression[1, 2].

In the recent years, cancer therapy efforts have been shared between efficient and targeted tumor cell killing and hypoxia reduction[2, 3]. Adoptive cell therapy has emerged as the fourth pillar of cancer therapy, offering specific eradication of hematological cancers. Therapeutic cell engineering is now tackling with solid tumors, proving more challenging. Roadblocks include tumor-induced immunosuppression, ineffective trafficking, poor tumor penetration and persistence. Importantly, these characteristics may be predictive of therapeutic outcome. Successful infiltration of therapeutic cells in tumors and subsequent specific cytotoxic activity *in vivo* is expected to induce tumor cell apoptosis. We hypothesize that cancer cell pO_2 increase is an indirect consequence of apoptotic processes and that imaging could provide real time readout of the effectiveness of emerging immunotherapeutic strategies[4].

Perfluorocarbons (PFC) exhibit weak molecular cohesion, enabling gas dissolution[5-7]. This intrinsic property was exploited in the 1990's[8-10] to emulsify PFC into biocompatible and injectable blood substitutes and breathing liquids[11, 12]. Gas dissolved in fluorinated

emulsions is not bound to the carrier but can be exchanged with the local environment[13]. Dissolution of paramagnetic oxygen in PFC lowers the ^{19}F spin-lattice relaxation time (T_1)[12, 14]. T_1 varies linearly with the absolute partial pressure of oxygen[15] (pO_2) and can be calculated from a calibration curve.

Perfluoro-15-crown-5-ether (PCE) is a macrocyclic structure resulting in only one resonance frequency at -92.5 ppm; conferring greater sensitivity and straightforward quantification over other perfluorocarbons with complex spectra. PCE oil can be emulsified into well-defined, stable nanoemulsions by means of emulsifiers[11], specifically pluronic surfactants[16, 17]. Such nanoemulsions are effective in labeling adherent or suspended cells by simple addition to the culture media. Therefore, intracellular oxygen tension of PCE-labeled cells can be calculated after *in vivo* administration.

In early studies, perfluorocarbon emulsion intravenous injection, followed by fluorine magnetic resonance imaging (MRI), enabled vasculature imaging[18-20] and tissue oximetry measurement *in vivo*[21-24]. This method is nonetheless imperfect, since contrast distribution throughout tissues of interest remains uneven. Kadayakkara *et al*. labeled glioma cells with PCE emulsion prior to implantation and showed persistent tumor oxygenation increase after chemotherapy treatment[25]. Zhong *et al.* showed that as few as tens of thousands of cytotoxic T cells infiltrating CNS tumors could cause a significant spike in tumor pO_2[26]. However, correlation between increased tumor oxygenation and apoptotic processes has not been established to date.

Noninvasive monitoring of tumor pO_2 levels during treatment can provide a preclinical surrogate biomarker for the effectiveness of emerging immunotherapeutic strategies and can be used to optimize therapeutic course and dosage[4]. We tested the

hypothesis that a measurable increase in tumor pO_2 is commensurate with CAR T cell apoptotic processes in a mouse model of sub-cutaneous glioblastoma (U87-EGFRvIII-Luc) treated with human CAR T cells. Using ^{19}F MRI/MRS, we measured the pO_2 time-course in flank glioma cells that were intracellularly labeled with PCE nanoemulsions and treated with intravenously-infused CAR T cells.

5.2. Materials and methods

5.2.1. PCE formulation

The perfluorocarbon emulsion was gravimetrically prepared from perfluoro-15-crown-5 ether (PCE, Exfluor, Round Rock, TX) and pluronic F68 to obtain a 5 weight percent F68 emulsion. This ratio has been shown to yield optimal droplet size and polydispersity index (PdI)[27]. In short, 1.25 g of PCE was added to 625 µl of 100 mg/ml F68 solution in a 10 ml glass vial (Wheaton, Millville, NJ) and vortexed 10 s. Water (5.45 ml) was added and the solution was subsequently vortexed (10 s) and ultrasonicated (Omni Ruptor 250 W, 30% power, 2 minutes, Omni International). The emulsion was then aspirated with a 10 ml syringe and underwent 4 passages on a microfluidizer (Microfluidics) equipped with a cooling coil and operating at 20K psi. The emulsion was immediately sterile filtered on a 0.2 µm polyethersulfone membrane (PES, Millex, Ireland) into a sterile glass vial. A 7 µl aliquot was kept aside and diluted in water and transferred to a cuvette for dynamic light scattering (DLS, Zetasizer Nano Z, Malvern, UK) measurement. Droplet size and polydispersity index were acquired in triplicates.

Emulsion concentration was determined by diluting 30 µl of emulsion in 270 µl of 0.1 % sodium trifluoroacetate (TFA, Sigma Aldrich) in D_2O (Acros Organics, Geel,

Belgium) into a 5 mm NMR tube (Wilman Labglass, Vineland, NJ). NMR quantification was performed on a 400 MHz (9.4 Tesla) Bruker AVANCE III HD-NanoBay spectrometer (Bruker, Inc., Billerica, MA) with: 17 μs pulse, 32,000 FID points, 100 ppm spectral width, 32 averages, and a recycle delay of 15 s. On the acquired ^{19}F NMR spectra, the TFA reference peak registers at -76 ppm and PCE at -92.5 ppm. The ^{19}F content of the nanoemulsion is determined by calculating the ratio of the PCE peak integrated area to the reference integral multiplied by the number of fluorine atoms in the TFA aliquot.

5.2.2. Human T cells and CAR transduction

Primary human T cells were enriched by Ficoll (Histopaque 1077, Sigma Aldrich, St Louis, MO) gradient density centrifugation and Magnetic Assisted Cell Sorting (MACS, Miltenyi Biotech Inc., Auburn, CA) from anonymous donor human blood (San Diego Blood Bank, San Diego, CA). T cells were then activated with dynabeads human T-activator CD3/CD28 (Gibco, Waltham, MA) and allowed to expand for 2 days in Roswell Park Memorial Institute media (RPMI, Gibco) supplemented with 10% FBS and 100 units/ml of recombinant human interleukin 2 (IL-2, Peprotech, Rocky Hill, NJ). For transduction, we employed a vector for CAR specific to EGFR-vIII as described by Johnson *et al*.[28]. Detailed protocol for CAR virus production and human T cell transduction is available elsewhere[29]. Briefly, plasmids psPAX2, pMD2.G and pELNS-3C10CD28–41BBz were used for virus production and 30 μl of virus yield with 3 μg/ml of Polybrene transfection agent (EMD Millipore, Billerica, MA) was applied to T cells overnight.

5.2.3. Glioblastoma cells

A human glioblastoma multiform (U87-EGFRvIII-Luc) cell line overexpressing the epidermal growth receptor variant III and the luciferase gene was kindly provided by Dr. Okada (UCSF) and maintained in T75 flasks (Sigma) in RPMI medium (Gibco), supplemented with 10% FBS.

5.2.4. Ex vivo cell labeling

For PCE labeling experiments, U87-EGFRvIII-Luc were plated at 90% confluence (triplicates of 1×10^6 cells in 1 ml in 6 well plate) and incubated overnight with different concentrations ranging from 2.5 mg/ml to 20 mg/ml of PCE emulsion as described elsewhere[25]. The absence of viability impairment due to intracellular PCE was confirmed by Trypan Blue exclusion assay. The cells were washed 3 times in PBS before NMR measurement of uptake or inoculation into the animal.

To measure the average PCE uptake, cells were counted, pelleted and resuspended in 150 μl lysis buffer (0.5% triton X in PBS) and transferred to a 5 mm NMR tube. Also, 50 μl of 0.1% TFA in D_2O was added to each tube and vortexed. NMR measurement and quantification was performed as described above. The mean ^{19}F/cell was calculated from the ^{19}F content divided by the cell count in the sample.

5.2.5. Flow cytometry assays

Transduction efficacy of the T cells was confirmed by flow cytometry with a biotin-SP-AffiniPure F(ab')2 fragment-specific goat anti-mouse antibody (Jackson Immuno

Research Laboratories, West Grove, PA) and a streptavidin-PE secondary (BD Pharmingen, San Diego, CA). For *in vivo* experiments, a population of at least 70% CAR positive T cells was used.

5.2.6. Murine model of subcutaneous glioblastoma

Animal protocols were approved by the University of California San Diego Institutional Animal Care and Use Committee (IACUC). For *in vivo* experiments, an optimal concentration of 20 mg/ml PCE was added overnight to U87-EGFRvIII-Luc or T cell media. Female (N=15) SCID 6-8 weeks old mice (Jackson Laboratories, Bar Harbor, ME) received subcutaneous unilateral flank tumor injection comprised of 5×10^6 PCE-labeled glioma cells in buffered 50% matrigel (Corning, Tewksbury, MA). Five days post-tumor inoculation (day 0 time point), mice were divided in three groups. Group 1 (N=5) received 2×10^7 CAR T cells injected intravenously (IV) in PBS. Group 2 (N=5) mice received the same number of naïve T cells IV. A second control group (Group 3) remained untreated (N=5).

5.2.7. In vivo Bioluminescence imaging (BLI)

Longitudinal BLI was performed at day 0, 1, 3, 7 and 10 using an IVIS Spectrum system (PerkinElmer, Waltham, MA). D-luciferin (Intrace Medical, Switzerland) was administered intraperitoneally, at a dose of 150 mg/kg 10 minutes prior to imaging. Anesthesia was induced with 2% isoflurane in an anesthesia box, and animals were then transferred to the IVIS chamber. Field of view was adjusted to allow imaging of five animals at once. Regions of interest (ROI) were defined as a circle encompassing the luminescent

signal from each tumor and the total flux (photons/s) was calculated using Living Image Software (PerkinElmer).

5.2.8. MRI

Animal preparation

MRI was performed on same days as BLI. Mice were anesthetized with 2% isoflurane in pure oxygen (1 L/min), transferred to the MRI bed and maintained on 1-1.5% isoflurane. Mice were positioned prone on an MRI bed with legs extended caudally. Animal vitals were monitored with an encoder receiver transmitter module (ERT Model 1030, SA Instruments, Inc., Stony Brook, NY) via a pneumatic pillow sensor for respiration and a rectal thermistor probe for temperature. Pulse oximetry was monitored with a MouseSTAT Jr. oximeter (Kent Scientific). An inbuilt warm water circuit in the MRI bed and a small animal heater (#770100, SA Instruments, Inc.) were used to maintain body temperature at 37 °C. A reference tube with PCE nanoemulsion (1:20) diluted in 2% agarose was taped beside the animal in the image field of view (FOV). MRI measurements were performed with an 11.7 T Bruker BioSpec preclinical scanner (Bruker, Billerica, MA) with a dual-tuned $^{1}H/^{19}F$ birdcage volume coil (Bruker).

Anatomical and spectroscopy sequences for tumor pO_2

The ^{19}F images were acquired using a RARE (Rapid Acquisition with Relaxation Enhancement) sequence with parameters TR/TE=400/23 ms, RARE factor 4, matrix 64×64, FOV 28×28 mm^2, slice thickness 1 mm, and 6 slices. The ^{1}H anatomical images were also

acquired using the RARE sequence with TR/TE=1400/7.8 ms, RARE factor 2, matrix 256×256, FOV 30×30 mm^2, slice thickness 1 mm, and 12 slices.

The ^{19}F R_1 values were measured using a point resolved spectroscopy (PRESS) sequence, by defining a voxel encompassing the entire tumor mass (8×8×8 mm^3). Twelve TR values were used to measure the R_1 relaxation rate, ranging between 0.1 and 6 s (total acquisition time ~30 min).

Data analysis

^{19}F images were manually thresholded for visualization purposes to remove background noise and rendered in pseudo-color using ImageJ software[30]. Anatomically-corresponding ^{1}H images remained unaltered and were super-imposed to the fluorine images with ImageJ. The tumor longitudinal fluorine signal was calculated based on the signal of a standard external reference using the Voxel Tracker software (Celsense, Pittsburgh, PA). The R_1 of each individual tumor was calculated by integrating the ^{19}F peak acquired at different TR values, and the resulting values were fit using a three-parameter single exponential equation in MNova 6.0.2 software (Mestrelab, Spain). The mean pO_2 of the tumor cells was then calculated using an established calibration curve[25, 26].

5.2.9. Histological correlation

At the experimental endpoint, animals were euthanized by CO_2 inhalation and tumors were excised, embedded in optimal cutting temperature (OCT) compound (Sakura Finetek USA, Inc., Torrance, CA) and stored at -80 °C. All tissues were cryosectioned (CM1950, Leica Microsystems Inc., Buffalo Grove, IL) at 10 μm thickness. Sections were fixed with

4% paraformaldehyde, stained for T cells using FITC anti-human CD3 (UCHT1, 1:500 dilution, Biolegend), apoptotic cells using TMR red TUNEL (Roche) and nuclei using Hoechst dye (#33342, 1:500 dilution, Thermo Fisher Scientific) and then mounted. Fluorescence images were acquired on an Axiovert 40 CFL microscope (Zeiss, Thornwood, NY) using a ×5 objective. Confocal images were acquired on a Leica SP5 2 confocal system with a Leica DM 6000 CFS microscope and a ×63 immersion objective.

For direct cell counts in tumor, we used sections (two per tumor) stained against CD3 or TUNEL from three tumors of animals sacrificed at Day 3 post T cell infusion. We counted T cells and apoptotic cells in six high power fields per slice (×63 magnification, 72 high power fields total).

5.2.10. Statistical Analyses

All measurements are presented as mean ± standard error. Acceptance criteria for R_1 measurement accuracy was defined as fit $R^2>0.995$ and R_1 standard error <0.05. A one-way ANOVA along with unpaired T-tests with unequal variances were performed to compare groups as a whole and by pairs respectively for bioluminescence, tumor volume and pO_2 measurements. For ANOVAs, we used the Bonferroni correction for multiple comparisons, thereby controlling the family-wise error rate at 5%. P-values less than 0.05 were considered statistically significant. ANOVA results are expressed as an F-statistic and its associated degrees of freedom and P-value.

For tumor pO_2 measurements, we also used linear mixed effects (LME) models to investigate differences in R_1 between mice treated with CAR T cells and the two control groups, *i.e.*, mice treated with untransduced T cells and untreated mice. A separate model

was fitted for the CAR T cells group versus the untransduced T cell group and for the CAR T cell group versus the untreated mice group, respectively. Fixed effects in the model included a treatment effect, a day effect (considering days as a categorical variable), and their interaction. Mouse identification was incorporated as a random effect, in order to model correlation among measurements on different days within the same mouse. For each LME model, we estimated the change from Day 0 for the treatment effect, with its corresponding 95% Wald confidence interval for each of Day 1, Day 3, Day 7 and Day 10. Finally, we used a Bonferroni adjustment for the four multiple comparisons for each model. We used these adjusted 95% confidence intervals to explore statistical significance.

Average ^{19}F MRI signal in tumors was correlated with the bioluminescence signal using a Pearson's correlation coefficient test. Apoptotic cell counts were correlated to T cell counts with the same test.

5.3. Results

5.3.1. Glioma cell labeling with PCE emulsion

Optimal PCE formulation comprised 5% F68, resulting in average droplet size of 176±4 nm and PdI of 0.098±0.02. U87-EGFRvIII-Luc cell incubation with different concentrations of PCE emulsion showed maximal uptake for 20 mg/ml (Fig. 5.1a) without viability impairment (Fig. 5.1b). Prior to implantation, U87-EGFRvIII-Luc cells were labeled overnight *ex vivo* with PCE to ~7×10^{12} atoms/cell, as measured via ^{19}F NMR.

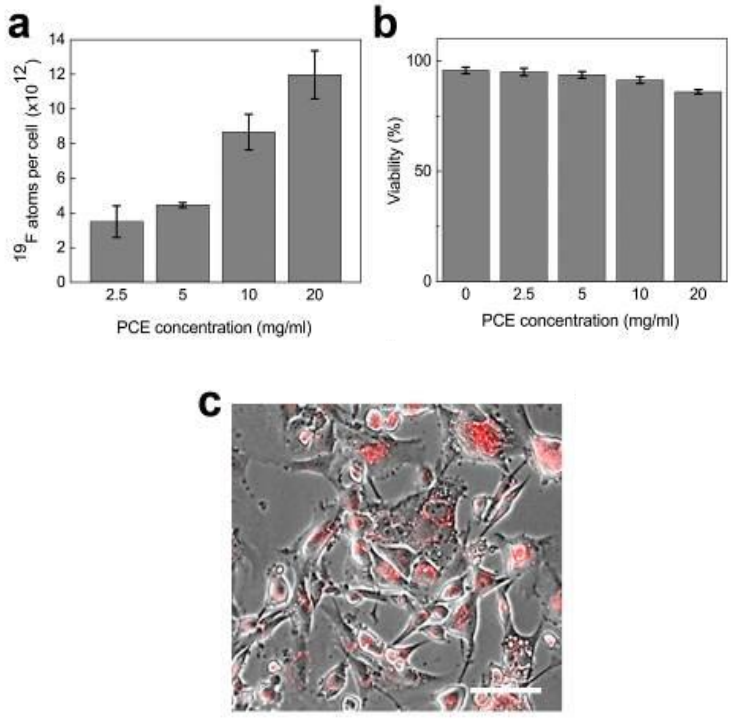

Figure 5.1: Glioma cell labeling with PCE emulsion. U87-EGFRvIII-Luc glioma cells are labeled overnight in full media with different PCE emulsion concentrations and average uptake (**a**) is measured by ^{19}F NMR. Within this range, negligible viability (**b**) impairment is observed. Data is presented as mean ± standard deviation of three independent replicates. U87-EGFRvIII-GFP glioma cells labeled overnight with a dual-mode fluorescent PFC exhibit punctate red fluorescent signal in their cytoplasm, as confirmed by brightfield (**c**) imaging. Scale bar represents 50 μm.

5.3.2. In vivo MRI and MRS of glioma pO_2

Five days after tumor implantation, baseline imaging (D0) was acquired prior to cell therapy infusion. ^{1}H axial image shows the presence of a solid tumor in the right flank of mice (Fig 5.2, top left). ^{19}F image reveals a single bright hotspot encompassing the whole tumor (Fig. 5.2, top right). Overlay of both images yields a ^{1}H/^{19}F composite that enables back-ground-free longitudinal imaging of tumor outline and clearance of PCE signal over time (Fig 5.2). Average SNR at Day 0 is ~10.

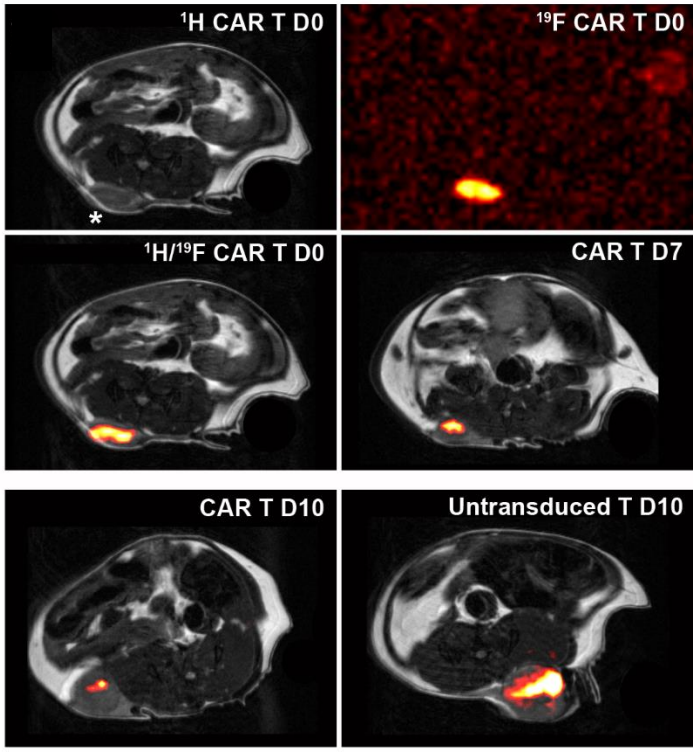

Figure 5.2: *In vivo* ^{19}F/^{1}H MRI of human glioma showing labeled tumor cells at different time points. Top left panel shows ^{1}H axial image the mouse abdomen with flank tumor (*). PCE-labeled glioma cells appear as a bright hotspot on ^{19}F images, delineating the tumor (top right panel, unthresholded). Both slices can be overlaid to yield a ^{1}H/^{19}F composite image (^{1}H/^{19}F CAR T Day 0). Representative longitudinal overlays of CAR T cell treated mouse show modestly growing tumor and decrease in ^{19}F signal as a result of cytotoxic efficacy of CAR therapy (Day 7, 10 panels). In comparison, mice receiving untransduced T cells exhibit persistent fluorine signal at Day 10 and larger tumor volume.

Localized, ^{19}F spectroscopy using the PRESS pulse sequence and a single voxel encompassing a tumor was used to measure R_1 values used to calculate pO_2. The R_1 measurements for each group are displayed as boxplots in Fig. 5.3a. The LME statistical model demonstrates a significant difference in R_1 between CAR T cell treated and untransduced T cell treated mice (treatment effect: 0.23, adjusted 95% CI: 0.01, 0.45) and untreated mice (treatment effect: 0.26, adjusted 95% CI: 0.05, 0.47) on Day 3 with respect to Day 0. This corresponds to a transient spike in tumor pO_2 three days after CAR T cell

infusion (R_1=0.99±0.12 s^{-1}, pO_2=134±25 mmHg) compared to untransduced T cells (pO_2=61±20 mmHg) and control (pO_2=40±9 mmHg, p = 0.026, Fig. 5.3a,b). There is no significant pO_2 change in the control groups at Day 3 (p=0.35). The average T_1 ($1/R_1$) recovery curve three days post-treatment (Fig. 5.3c) shows evident T_1 shortening in the CAR T cell treated group compared to controls.

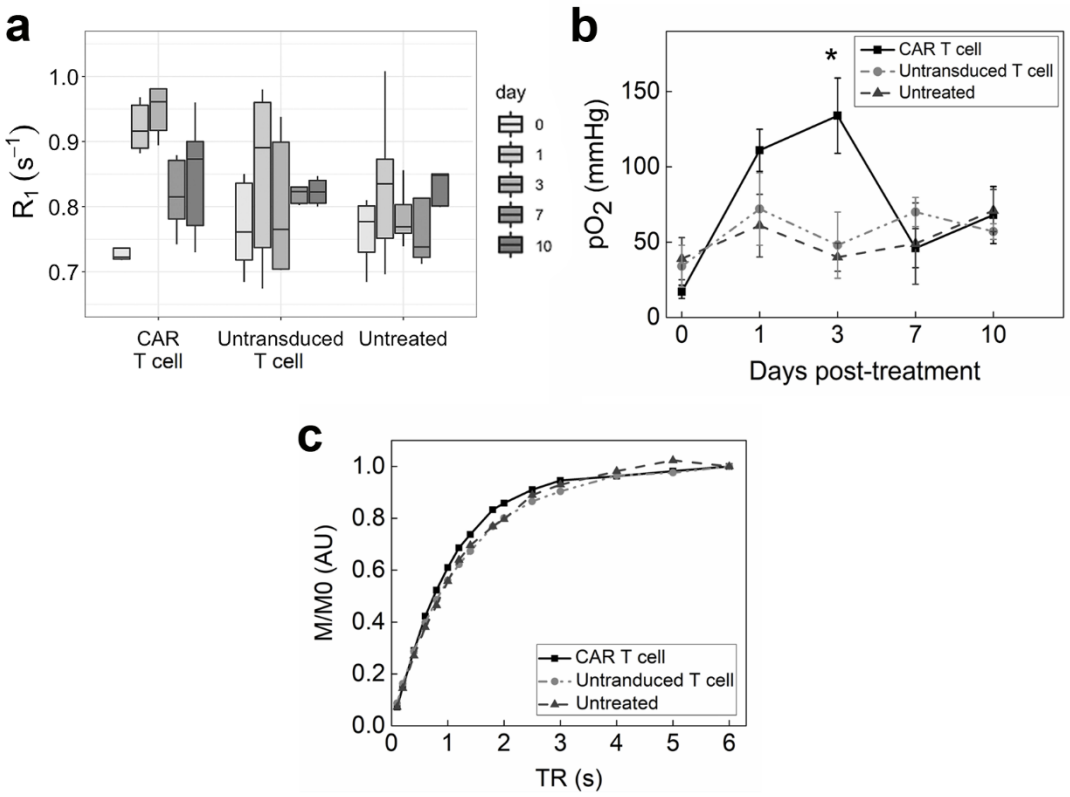

Figure 5.3: *In vivo* R_1 and pO_2 changes of glioma tumor after CAR T cell therapy. Panel (**a**) shows boxplots of raw data for each experimental group on days 0, 1, 3, 7, and 10. The upper line, middle line and bottom line of each box indicates the 75th, 50th and 25th percentile, respectively. The ends of the lines outside of the box show the maximum and the minimum value of the data on that day, for that group. Panel (**b**) shows corresponding longitudinal tumor pO_2 measurements following delivery of CAR T cells, untransduced T cells or untreated controls. A significant increase in tumor pO_2 in CAR T cell-treated animals is observed at day 3 post-infusion (*, p = 0.022). Panel (**c**) depicts average T_1 ($1/R_1$) recovery for all groups at day 3 post-treatment.

These data suggest specific CAR T cell homing to the tumor tissue, presumably initiating a target killing cascade, and altering intracellular pO_2. Histological analyses of tumor tissue at Day 3 confirms intracellular localization of PFC droplets and supports the assumption that pO_2 value measured is that of cancer cells (Figure 5.4), consistent with prior observations[25]. By day 7, tumor oxygenation returned to baseline in the CAR T cell Group (Fig. 5.3b).

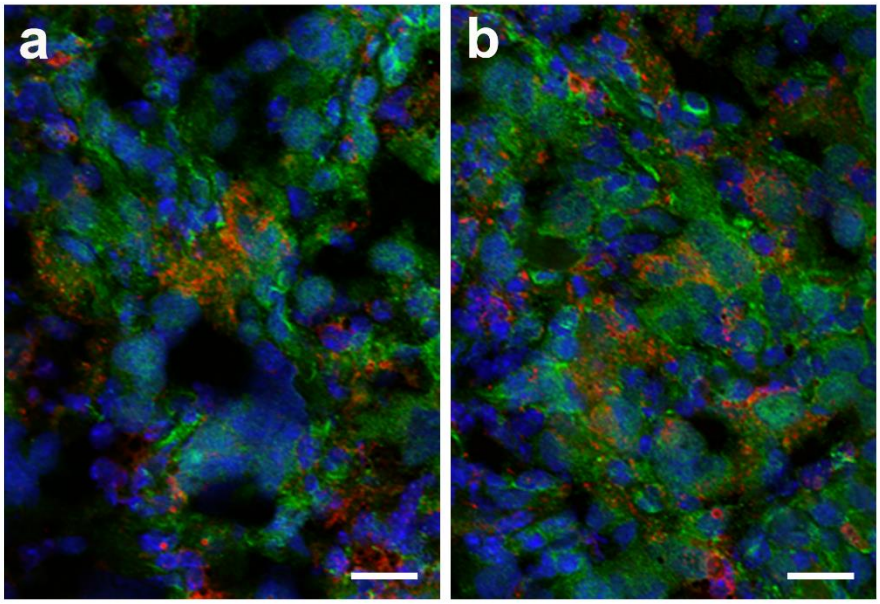

Figure 5.4: Confirmation of intracellular localization of PCE nanoemulsion. Confocal microscopy of tumor sections three days after CAR T cell treatment confirms intracellular localization of PCE (red) emulsion in tumor cells expressing GFP (green). Nuclei are stained with Hoescht (blue). Representative images of the tumor periphery (**a**) and tumor center (**b**) are shown. Magnification is 63× and scale bar = 25 μm.

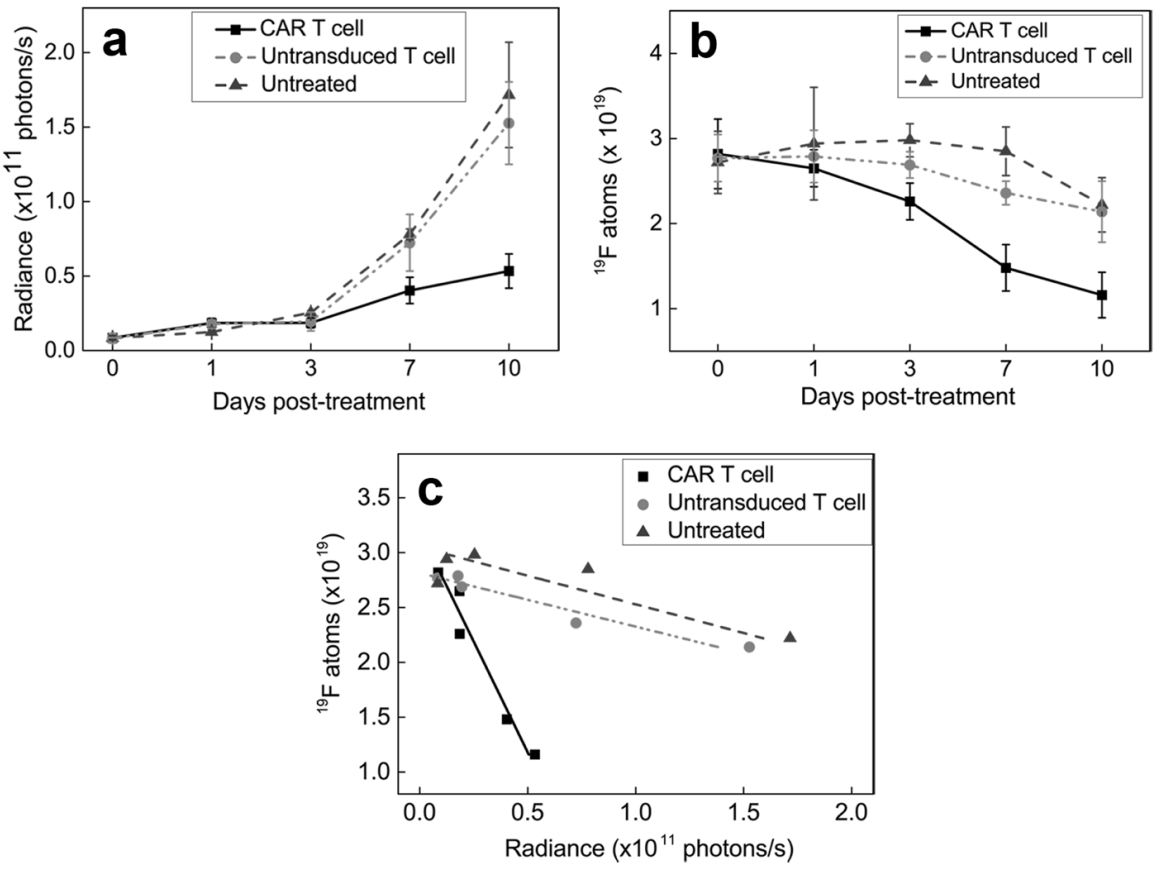

Figure 5.5: Tumor and fluorine atom reduction after CAR T cell therapy. Bioluminescence intensity (**a**) shows twice lower radiance in CAR-treated animals compared to controls at day 7 (*, p = 0.01). By day 10, the radiance gap widens, representing significant tumor growth reduction in the CAR-treated group (*, p= 0.01). Total fluorine content in the tumors was also evaluated longitudinally (**b**) in all three groups. Control groups did not exhibit significant ^{19}F signal loss over ten days, whereas CAR T treated group ^{19}F signal decreased by ~60% in the same period (p=0.0012). Comparison of total fluorine atoms to bioluminescence signal in tumors (**c**) showed strong negative correlation (Pearson's R: -0.85<R<-0.98) in all groups, suggesting that total fluorine signal is an indicator of therapeutic efficacy.

Longitudinal bioluminescence measurements show significant tumor growth reduction 7 days post CAR treatment with an average radiance of $4*10^{10}$ photons/sec, which is half the amount measured for both naïve T-cell treated and untreated groups (p=0.012, Fig. 5.4a).

Absolute fluorine content in the two control groups does not change significantly over 10 days (p=0.1 and 0.2, Fig. 5.5b), whereas the CAR T cell treated tumors exhibit significant fluorine signal loss (~ 60% signal loss, p=0.0012, Fig. 5.5b). Signal loss between groups is significant as early as day 3 (p=0.03, Fig. 5.5b). There is a strong negative correlation between absolute fluorine content in tumor and tumor radiance in all groups (Pearson's R: -0.85<R<-0.98, Fig. 5.5c). The PFC droplets are neither broken-down or exocytosed by the cell[31]. Signal loss is therefore attributable to cancer cell death and scavenging of cell contents by macrophages and subsequent uptake in the liver. A fluorine signal decrease is thus an additional indicator of therapy efficacy, inversely proportional to tumor growth.

5.3.3. Histological correlation

Histopathological staining of tumors three days post-therapeutic cell infusion confirms the presence of numerous CAR T cells in the tumor, and to a lesser extent, untransduced T cells (Fig. 5.6a). TUNEL staining reveals numerous apoptotic cells in the vicinity of CAR T cells but few to no apoptotic cells are seen in untransduced T cell treated tumors. Quantitatively, more than twice the number of CAR T cells infiltrate the tumor compared to untransduced T cells (p=0.0002, Fig. 5.6b). CAR T cell treated tumor sections exhibit numerous apoptotic tumor cells whereas few apoptotic cells are found in untransduced T cell treated tumors, consistent with the magnetic resonance spectroscopy results (p=0.0001, Fig. 5.6c). The number of CAR T cells present correlates to the number of apoptotic cells per field (R=0.67) whereas untransduced T cells do not (R= -0.31, Fig. 5.6d). This indicates that CAR T cells exhibit specific cytotoxic activity towards cancer cells

in vivo. Untransduced T cells, despite reaching the tumor site, do not induce detectable cancer cell apoptosis.

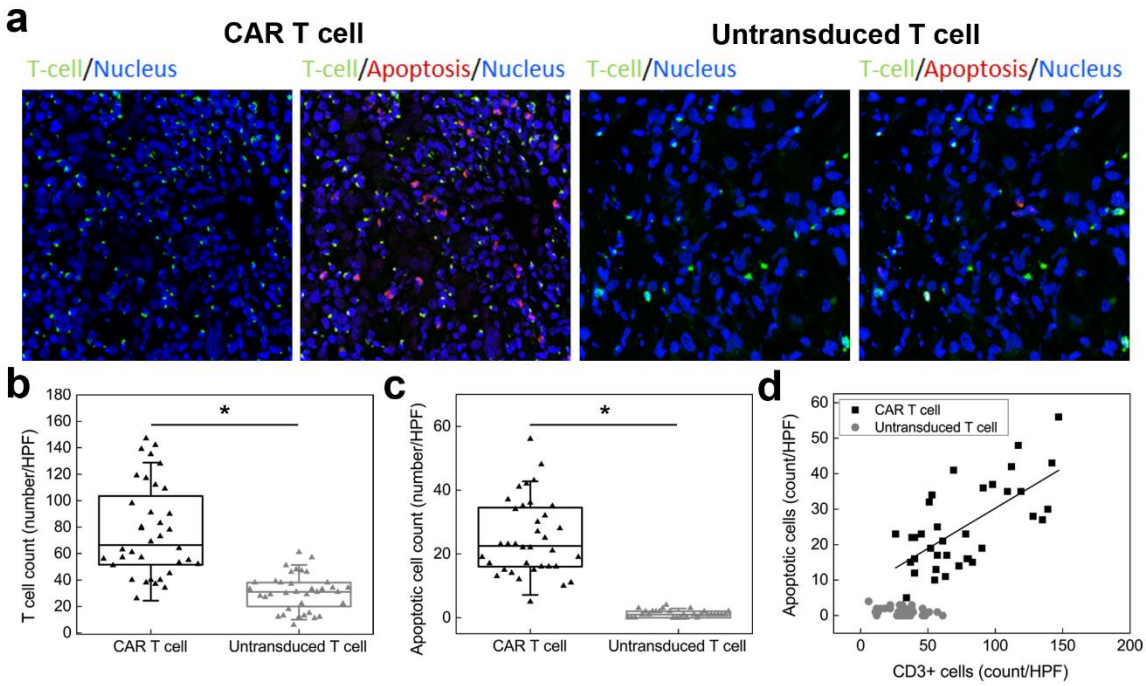

Figure 5.6: Histological correlation of T cell infiltration in tumor and resulting cell death. Confocal microscopy (×64, **a**) of tumor tissues shows prominent CAR T cell infiltrates (green) at day 2 after infusion in the proximity of apoptotic cells (red) as evidenced by positive TUNEL stain. Untransduced T cell-treated tumor exhibit sparser T cells and apoptotic signals. High power field (HPF) quantitation of T cell numbers (**b**) showed twice as many CAR T cells per HPF on average compared to untransduced T cells (p=0.0002). Numerous apoptotic cells (**c**) are found in CAR T cell treated tumors, contrary to untransduced T cell treated tumors (p=0.0001) The number of CAR T cells present correlated (**d**) to the number of apoptotic cells per field (R=0.67) whereas untransduced T cells did not (R= -0.31).

5.4. Discussion

In this study, we show that ^{19}F MRI enables real time quantitative measurement of tumor cell death in response to CAR T cell therapy and associated intracellular tumor pO_2

changes. Peak pO_2 was observed three days post-infusion and suggests significant CAR T cell infiltration and targeted tumor cell killing, compared to untransduced T cells. Loss of fluorine signal in the tumor, indicative of cancer cell death, correlated to bioluminescence measurements. In addition, CAR T cell numbers in the tumor at day 3 correlated to cancer cell apoptosis, whereas untransduced T cells did not generate significant apoptosis.

Established methods of oxygenation measurement, such as electrodes or fiber-optic sensors[32, 33] require invasive insertion of probes in tumors, resulting in tissue and vascular damage, inflammation, and partial tumor volume readout. Application of non-invasive MRI methods for imaging of tumor oxygenation is desirable as it eliminates tissue injury and measurement errors[34]. In addition, MRI does not involve radioactive isotopes. One can indirectly measure blood oxygen level by measuring differences between hemoglobin and paramagnetic deoxyhemoglobin (shortens the spin-spin relaxation time T_2 of surrounding protons). Blood oxygen level dependent (BOLD) MRI is qualitative with regards to pO_2 determination, since BOLD changes reflect vasculature oxygenation and not intracellular partial pressure. In addition, poorly vascularized tumors may not show a BOLD effect. Dynamic contrast-enhanced (DCE) MRI relies on tumor perfusion to gage hypoxic tumors. DCE MRI has been shown to correlate to Eppendorf probe measurements[35] but not to hypoxia (pimonidazole) staining or PET probes in few cancer types[36-38].

Perfluorocarbon nanoemulsions dissolve oxygen resulting in a linear increase in the ^{19}F spin-lattice relaxation rate (R_1) with increasing pO_2. PFC-labeling of tumor cells prior injection enables uniform label distribution within the tumor and circumvents biases resulting from local or systemic injection of tracer agent. Accurate pO_2 determination also entails control of the subject's temperature and blood oxygenation level. In our experiments,

temperature of the animals was kept at 37 °C throughout the measurements. Both isoflurane and injectable anesthesia doses were adjusted to maintain blood oxygen saturation of ~99%.

The pO_2 measurements presented are in accordance with previously reported results of tumor oxygenation changes in response to chemotherapy[25, 26] and cytotoxic T-cells[26]. Using similar methods, Kadayakkara *et al.*[25] reported rat glioma cells basal pO_2 of ~45 mmHg. Treatment with chemotherapeutic agent resulted in sustained pO_2 increase to ~165 mmHg over 72 hours. Zhong *et al.*[26] used a mouse model of glioma treated with Pmel-1 cytotoxic T cells and showed transient pO_2 increase (~94 mmHg) two days post-infusion.

Similarly to Zhong *et al.*, pO_2 increase in the CAR T cell treated group was short-lived, suggesting insufficient therapeutic cell homing to the tumor and possible CAR T cell exhaustion or tumor immunosuppression[39]; all being perceived as important bottlenecks in successful adoptive cell therapy. The persistence of ^{19}F signal in the core of CAR-treated tumors is also an indicator of low immune cell infiltration. Conversely, reduced ^{19}F signal in the periphery of CAR-treated tumors suggests active cytotoxic activity of CAR T cells and PFC scavenging by local macrophages, followed by PFC clearance to liver tissue. Therefore, remaining PFC-containing tumor cells may predominantly be located in the hypoxic core and contribute to the decreased pO_2 readout (Fig. 5.4). We also observed significant fluorine signal loss in CAR T cell-treated tumors, whereas control groups did not show significant reduction. These results correlated to bioluminescence measurements. Therefore, fluorine MRI, combined with MRS measurement is an effective method to image therapeutic efficacy.

A notable limitation of this technique is that it is only applicable to preclinical models in its current form. Nonetheless, this method is not restricted to tumor models and could be

extended to more cell types, including immune cells and stem cells to monitor oxygen changes in tissue engineering and other disease models. In addition, this method yields bulk tumor pO_2 number, although tumor aggressiveness and therapy efficacy assessments would benefit from discrete information. Improvements in MRI sensitivity and data sampling methods could enable pO_2 map delineation. Considerable effort is underway to implement fast imaging methods[40-42].

Strategies to increase tumor penetration and oxygenation are paramount in contemporary cancer research. Overall, we show that ^{19}F MRI enables temporal measurements of tumor cell oxygen tension in response to CAR T cell therapy. These data support the view that ^{19}F pO_2 MRI and MRS can serve as a biomarker for cell-mediated apoptosis in preclinical tumor models and provide insight into the modes of action of engineered T cell immunotherapy against cancer.

Acknowledgements

Chapter 5, in full is currently being prepared for submission for publication of the material. Chapelin F, Zhu W, Chen R, Lister D, Stares E, Messer K, Okada H, Ahrens E.T. Magnetic resonance imaging monitoring of *in vivo* intracellular oximetry response to chimeric antigen receptor T cell immunotherapy against glioma. The dissertation author was the primary investigator and author of this paper.

References

1. Tatum, J.L., Kelloff, G.J., Gillies, R.J., Arbeit, J.M., Brown, J.M., Chao, K.S., Chapman, J.D., Eckelman, W.C., Fyles, A.W., Giaccia, A.J., Hill, R.P., Koch, C.J., Krishna, M.C., Krohn, K.A., Lewis, J.S., Mason, R.P., Melillo, G., Padhani, A.R., Powis, G., Rajendran, J.G., Reba, R., Robinson, S.P., Semenza, G.L., Swartz, H.M., Vaupel, P., Yang, D., Croft, B., Hoffman, J., Liu, G., Stone, H. & Sullivan, D. Hypoxia: importance in tumor biology, noninvasive measurement by imaging, and value of its measurement in the management of cancer therapy. *Int J Radiat Biol* **82**, 699-757 (2006).

2. Teicher, B.A. A systems approach to cancer therapy. (Antioncogenics + standard cytotoxics-->mechanism(s) of interaction). *Cancer Metastasis Rev* **15**, 247-272 (1996).

3. Jain, R.K. Normalization of tumor vasculature: an emerging concept in antiangiogenic therapy. *Science* **307**, 58-62 (2005).

4. Matsuo, M., Matsumoto, S., Mitchell, J.B., Krishna, M.C. & Camphausen, K. Magnetic resonance imaging of the tumor microenvironment in radiotherapy: perfusion, hypoxia, and metabolism. *Semin Radiat Oncol* **24**, 210-217 (2014).

5. Riess, J.G. Understanding the fundamentals of perfluorocarbons and perfluorocarbon emulsions relevant to in vivo oxygen delivery. *Artificial cells, blood substitutes, and immobilization biotechnology* **33**, 47-63 (2005).

6. Hamza, M.A., Serratrice, G., Stebe, M.J. & Delpuech, J.J. Fluorocarbons as Oxygen Carriers .2. An Nmr-Study of Partially or Totally Fluorinated Alkanes and Alkenes. *J Magn Reson* **42**, 227-241 (1981).

7. Hamza, M.A., Serratrice, G., Stebe, M.J. & Delpuech, J.J. Solute-Solvent Interactions in Perfluorocarbon Solutions of Oxygen - an Nmr-Study. *J Am Chem Soc* **103**, 3733-3738 (1981).

8. Garrelts, J.C. Fluosol: an oxygen-delivery fluid for use in percutaneous transluminal coronary angioplasty. *DICP : the annals of pharmacotherapy* **24**, 1105-1112 (1990).

9. Ilgiavishute Ia, S., Zhukauskas, G., Dapshis, K.L. & Onishchenko, N.A. [The use of perfluorocarbon emulsions for suppression of rejection reaction in kidney allotransplantation]. *Khirurgiia*, 16-18 (1993).

10. Mason, R.P. Noninvasive Physiology - F-19 Nmr of Perfluorocarbons. *Artif Cell Blood Sub* **22**, 1141-1153 (1994).

11. Riess, J.G. Oxygen carriers ("blood substitutes")--raison d'etre, chemistry, and some physiology. *Chemical reviews* **101**, 2797-2920 (2001).

12. Delpuech, J.J., Hamza, M.A., Serratrice, G. & Stebe, M.J. Fluorocarbons as Oxygen Carriers .1. Nmr-Study of Oxygen Solutions in Hexafluorobenzene. *J Chem Phys* **70**, 2680-2687 (1979).

13. LoNostro, P., Choi, S.M., Ku, C.Y. & Chen, S.H. Fluorinated microemulsions: A study of the phase behavior and structure. *J Phys Chem B* **103**, 5347-5352 (1999).

14. Delpuech, J.J., Hamza, M.A. & Serratrice, G. Determination of Oxygen by a Nuclear Magnetic-Resonance Method. *J Magn Reson* **36**, 173-179 (1979).

15. Sotak, C.H., Hees, P.S., Huang, H.N., Hung, M.H., Krespan, C.G. & Raynolds, S. A new perfluorocarbon for use in fluorine-19 magnetic resonance imaging and spectroscopy. *Magnetic Resonance in Medicine* **29**, 188-195 (1993).

16. Janjic, J.M., Srinivas, M., Kadayakkara, D.K.K. & Ahrens, E.T. Self-delivering nanoemulsions for dual fluorine-19 MRI and fluorescence detection. *J Am Chem Soc* **130**, 2832-2841 (2008).

17. Sharts, C.M., Reese, H.R., Ginsberg, K.A., Multer, F.K., Nielson, M.D., Greenburg, A.G., Peskin, G.W. & Long, D.M. Solubility of Oxygen in Aqueous Fluorocarbon Emulsions. *J Fluorine Chem* **11**, 637-641 (1978).

18. Fishman, J.E., Joseph, P.M., Floyd, T.F., Mukherji, B. & Sloviter, H.A. Oxygen-sensitive 19F NMR imaging of the vascular system in vivo. *Magn Reson Imaging* **5**, 279-285 (1987).

19. Duong, T.Q., Iadecola, C. & Kim, S.G. Effect of hyperoxia, hypercapnia, and hypoxia on cerebral interstitial oxygen tension and cerebral blood flow. *Magn Reson Med* **45**, 61-70 (2001).

20. Duong, T.Q. & Kim, S.G. In vivo MR measurements of regional arterial and venous blood volume fractions in intact rat brain. *Magn Reson Med* **43**, 393-402 (2000).

21. Dardzinski, B.J. & Sotak, C.H. Rapid tissue oxygen tension mapping using 19F inversion-recovery echo-planar imaging of perfluoro-15-crown-5-ether. *Magn Reson Med* **32**, 88-97 (1994).

22. Hees, P.S. & Sotak, C.H. Assessment of changes in murine tumor oxygenation in response to nicotinamide using 19F NMR relaxometry of a perfluorocarbon emulsion. *Magn Reson Med* **29**, 303-310 (1993).

23. van der Sanden, B.P., Heerschap, A., Simonetti, A.W., Rijken, P.F., Peters, H.P., Stuben, G. & van der Kogel, A.J. Characterization and validation of noninvasive oxygen tension measurements in human glioma xenografts by 19F-MR relaxometry. *Int J Radiat Oncol Biol Phys* **44**, 649-658 (1999).

24. Shukla, H.P., Mason, R.P., Bansal, N. & Antich, P.P. Regional myocardial oxygen tension: 19F MRI of sequestered perfluorocarbon. *Magn Reson Med* **35**, 827-833 (1996).

25. Kadayakkara, D.K., Janjic, J.M., Pusateri, L.K., Young, W.B. & Ahrens, E.T. In vivo observation of intracellular oximetry in perfluorocarbon-labeled glioma cells and chemotherapeutic response in the CNS using fluorine-19 MRI. *Magn Reson Med* **64**, 1252-1259 (2010).

26. Zhong, J., Sakaki, M., Okada, H. & Ahrens, E.T. In vivo intracellular oxygen dynamics in murine brain glioma and immunotherapeutic response of cytotoxic T cells observed by fluorine-19 magnetic resonance imaging. *PloS one* **8**, e59479 (2013).

27. Janjic, J.M. & Ahrens, E.T. Fluorine-containing nanoemulsions for MRI cell tracking. *Wiley interdisciplinary reviews. Nanomedicine and nanobiotechnology* **1**, 492-501 (2009).

28. Johnson, L.A., Scholler, J., Ohkuri, T., Kosaka, A., Patel, P.R., McGettigan, S.E., Nace, A.K., Dentchev, T., Thekkat, P., Loew, A., Boesteanu, A.C., Cogdill, A.P., Chen, T., Fraietta, J.A., Kloss, C.C., Posey, A.D., Jr., Engels, B., Singh, R., Ezell, T., Idamakanti, N., Ramones, M.H., Li, N., Zhou, L., Plesa, G., Seykora, J.T., Okada, H., June, C.H., Brogdon, J.L. & Maus, M.V. Rational development and characterization of humanized anti-EGFR variant III chimeric antigen receptor T cells for glioblastoma. *Science translational medicine* **7**, 275ra222 (2015).

29. Chapelin, F., Gao, S., Okada, H., Weber, T.G., Messer, K. & Ahrens, E.T. Fluorine-19 nuclear magnetic resonance of chimeric antigen receptor T cell biodistribution in murine cancer model. *Scientific Reports* **7**, 17748 (2017).

30. Schneider, C.A., Rasband, W.S. & Eliceiri, K.W. NIH Image to ImageJ: 25 years of image analysis. *Nature methods* **9**, 671-675 (2012).

31. Ahrens, E.T., Flores, R., Xu, H. & Morel, P.A. In vivo imaging platform for tracking immunotherapeutic cells. *Nat Biotechnol* **23**, 983-987 (2005).

32. Braun, R.D., Lanzen, J.L., Snyder, S.A. & Dewhirst, M.W. Comparison of tumor and normal tissue oxygen tension measurements using OxyLite or microelectrodes in rodents. *Am J Physiol Heart Circ Physiol* **280**, H2533-2544 (2001).

33. Seddon, B.M., Honess, D.J., Vojnovic, B., Tozer, G.M. & Workman, P. Measurement of tumor oxygenation: in vivo comparison of a luminescence fiber-optic sensor and a polarographic electrode in the p22 tumor. *Radiat Res* **155**, 837-846 (2001).

34. O'Hara, J.A., Hou, H., Demidenko, E., Springett, R.J., Khan, N. & Swartz, H.M. Simultaneous measurement of rat brain cortex PtO2 using EPR oximetry and a

fluorescence fiber-optic sensor during normoxia and hyperoxia. *Physiol Meas* **26**, 203-213 (2005).

35. Cooper, R.A., Carrington, B.M., Loncaster, J.A., Todd, S.M., Davidson, S.E., Logue, J.P., Luthra, A.D., Jones, A.P., Stratford, I., Hunter, R.D. & West, C.M. Tumour oxygenation levels correlate with dynamic contrast-enhanced magnetic resonance imaging parameters in carcinoma of the cervix. *Radiother Oncol* **57**, 53-59 (2000).

36. Hoskin, P.J., Carnell, D.M., Taylor, N.J., Smith, R.E., Stirling, J.J., Daley, F.M., Saunders, M.I., Bentzen, S.M., Collins, D.J., d'Arcy, J.A. & Padhani, A.P. Hypoxia in prostate cancer: correlation of BOLD-MRI with pimonidazole immunohistochemistry-initial observations. *Int J Radiat Oncol Biol Phys* **68**, 1065-1071 (2007).

37. Newbold, K., Castellano, I., Charles-Edwards, E., Mears, D., Sohaib, A., Leach, M., Rhys-Evans, P., Clarke, P., Fisher, C., Harrington, K. & Nutting, C. An exploratory study into the role of dynamic contrast-enhanced magnetic resonance imaging or perfusion computed tomography for detection of intratumoral hypoxia in head-and-neck cancer. *Int J Radiat Oncol Biol Phys* **74**, 29-37 (2009).

38. Swanson, K.R., Chakraborty, G., Wang, C.H., Rockne, R., Harpold, H.L., Muzi, M., Adamsen, T.C., Krohn, K.A. & Spence, A.M. Complementary but distinct roles for MRI and 18F-fluoromisonidazole PET in the assessment of human glioblastomas. *J Nucl Med* **50**, 36-44 (2009).

39. Fesnak, A.D., June, C.H. & Levine, B.L. Engineered T cells: the promise and challenges of cancer immunotherapy. *Nat Rev Cancer* **16**, 566-581 (2016).

40. Hunjan, S., Zhao, D., Constantinescu, A., Hahn, E.W., Antich, P.P. & Mason, R.P. Tumor oximetry: demonstration of an enhanced dynamic mapping procedure using fluorine-19 echo planar magnetic resonance imaging in the Dunning prostate R3327-AT1 rat tumor. *Int J Radiat Oncol Biol Phys* **49**, 1097-1108 (2001).

41. Jordan, B.F., Cron, G.O. & Gallez, B. Rapid monitoring of oxygenation by 19F magnetic resonance imaging: Simultaneous comparison with fluorescence quenching. *Magn Reson Med* **61**, 634-638 (2009).

42. Zhong, J., Mills, P.H., Hitchens, T.K. & Ahrens, E.T. Accelerated fluorine-19 MRI cell tracking using compressed sensing. *Magn Reson Med* **69**, 1683-1690 (2013).

Chapter 6: Conclusions

6.1. Summary of research

^{19}F MRI is a promising tool for imaging of cellular therapeutics and holds great potential for clinical applications. The work in this thesis aimed to further develop fluorine imaging platforms to aid in assessment of T cell therapy biodistribution, persistence and efficacy.

6.1.1. ^{19}F NMR of CAR T cell biodistribution in murine cancer model

As a first step, we used commercially available perfluorocarbon nanoemulsion to intracellularly label human T cells and CAR T cells. We confirmed that such label was internalized by means of fluorescence and electron microscopy. We also demonstrated that PFC label does not alter T cell viability, division rate and phenotype (defined by CD3/CD4/CD8 expression) for at least 14 days post-labeling. *In vitro* co-culture assays showed that cytotoxic activity of CAR T cells against glioma cells remained comparable in PFC-labeled cells compared to unlabeled cells.

When infused into a murine cancer model, CAR T cell systemic infusion induced significant tumor growth decline compared to untransduced T cell and untreated controls. ^{19}F NMR measurement enabled T cell biodistribution quantification in intact tissues with sensitivity limits of detection of order 10^3 T cells per sample. Tissue panel spectra analysis demonstrated significantly higher CAR T cell homing to tumors and spleen compared to untransduced T cells. In addition, CAR T cell persistence surpassed that of naïve T cells.

Histology high power field counts strongly correlated to the average NMR fluorine signal measured in tumors.

These findings implement ^{19}F NMR cytometry as a rapid and quantitative technique to evaluate adoptive cell transfer biodistribution in intact tissues. This technique provides unbiased quantification in samples. Overall, ^{19}F NMR cytometry may accelerate the timeline to evaluate new immunotherapeutic cell candidates by providing a straightforward method to evaluate cell therapy biodistribution and cell fate.

6.1.2. TAT-functionalized PFC nanoemulsion for ^{19}F cell tracking

For clinical relevance, T cell biodistribution needs to be monitored *in vivo* by ^{19}F MRI cytometry. The persistent bottleneck that remains for tracking of transferred T cells is ^{19}F MRI sensitivity. T cells are inherently smaller and less phagocytic than most cell types, limiting the amount of PFC they can hold. To address this, we designed functionalized probes that carry a cell internalizing peptide (TAT) on their surface. We optimized the formulation for maximal MR sensitivity gain and optimal droplet size and stability. Biocompatibility was tested in T cells and labeling protocol was established to preserve cell viability and cytotoxic activity. Addition of TAT as a co-surfactant in PFC emulsions resulted in 8-fold increase in T cell labeling efficiency.

Signal enhancement *in vivo* was obtained by delivering CAR T cells pre-labeled with TAT-conjugated PFC emulsions or control PFC emulsions intratumorally in mice bearing bilateral flank tumors. Signal detected from TAT-labeled CAR T cells two hours post-injection was eight times higher than that of contralateral tumor injected with PFC-labeled CAR T cells, rendering MRI signal unambiguous. The correlation between fluorine atoms

measured in tumors and number of injected cells confirms accuracy of cell delivery and persistence of the CAR T cells at the tumor site for at least several hours post injection.

This new probe may enable longitudinal imaging of the fate of T cells *in vivo* and enable treatment optimization from real-time readout. Additional incorporation of metal ions within the core of PFC emulsions may open up tremendous future opportunities for the MRI cell tracking field and enable accelerated MRI acquisitions and the detection of sparser cell populations *in vivo*.

6.1.3. In vivo monitoring of tumor pO_2 in response to CAR T cell immunotherapy

PFC nanoemulsions may assist in indirect detection of adoptive cell therapy cytotoxicity against cancer cells. Tumor cells can be labeled similarly to T cells with perfluoro-crown-ether (PCE) probes *in vitro* before injection into the animal model. The spin-lattice relaxation rate (R_1) of PCE is linearly proportional to the oxygen concentration in its close proximity, allowing for tissue oxygenation sensing. We explored the temporal dynamics of tumor intracellular pO_2 in our murine glioma model.

We showed that ^{19}F MRI enables real-time quantitative measurement of tumor cell death in response to CAR T cell therapy via a pO_2 change. Peak pO_2 was observed 3 days post-infusion and suggests significant CAR T cell infiltration and targeted tumor cell killing, compared to untransduced T cells. Loss of fluorine signal in the tumor, indicative of cancer cell death, correlated to bioluminescence measurements. In addition, CAR T cell numbers in the tumor at day 3 correlated to cancer cell apoptosis, whereas untransduced T cells did not generate significant apoptosis. This indicates that CAR T cells exhibit specific cytotoxic

activity towards cancer cells *in vivo*. Untransduced T cells, despite reaching the tumor site, do not induce detectable cancer cell apoptosis.

Overall, we showed that ^{19}F MRI enables temporal measurements of tumor cell oxygen tension in response to CAR T cell therapy. These data support the view that ^{19}F pO_2 MRI can serve as a surrogate biomarker for cell-mediated apoptosis and provide insights into the modes of action of engineered T cell immunotherapy against cancer.

6.2. Limitations of infusing PFC labeled cells

Generally, with PFC labeled cells having a mitotic phenotype, cell division and subsequent dilution of the intracellular label can potentially limit long-term studies of itinerant cells and decrease the accuracy of cell quantification[1]. There is no evidence for active exocytosis or degradation of the PFC droplets once internalized by viable cells. Death of labeled cells can lead to dispersion of the reagent and thus a loss of ^{19}F signal. Potentially, the PFC droplets can also be transferred to macrophages that have engulfed dead cells. If a large number of macrophages remain in a region of interest, quantification accuracy will suffer. Importantly, the ^{19}F signal diminishes at cell injection sites over time if the cells are apoptotic, and this cell loss is accurately quantifiable in longitudinal scans[2, 3], which is an advantage over prior-art iron-oxide nanoparticle based cell tracking approaches[4, 5]. Ultimately, clearance of PFC agents from the body occurs via uptake by cells of the RES, particularly Kupffer cells of the liver, followed by lung exhalation[6]. In fact, the ^{19}F liver signal, and the effective number of cells represented by this value, can be used as a proxy to calculate the dead cell fraction of the infused cell product[1].

6.3. Future perspectives

Since its introduction in clinical practice in the 1980s, MRI has experienced remarkable growth and development. But implementation of new clinical applications comes with challenges both technical and logistical in nature. Often a key limitation of ^{19}F MRI probes is sensitivity. Unlike conventional ^{1}H MRI, where the probe (water) concentration (>100 Molar ^{1}H) and thus sensitivity is high, ^{19}F MRI is limited by the total amount and distribution of fluorine atoms introduced into the subject's tissue. The limits of detection using ^{19}F-based imaging ranges from ~10^3 to ~10^5 cells per voxel[7]. For a given experiment, results depend on specific details, such as the PFC molecule and nanoemulsion used, the cell type labeled, viability of cell culture and commensurate label uptake, image acquisition methods, magnetic field strength, and the MRI detector configuration[1, 2, 8, 9].

Looking forward, there are multiple, technical avenues for improving cell detection sensitivity that are vigorously being investigated involving new probe design and data acquisition methods[10-12]. One approach that we explored in Chapter 4, is to formulate imaging probes with cell penetrating peptides (CPP) to increase cell delivery. Besides TAT, numerous CPPs with diverse chemical and biological properties are being investigated[13] for drug or DNA delivery. Testing of alternate CPPs may reveal more efficient cell loading.

Another scheme is to exploit the properties of metals to reduce the ^{19}F spin-lattice relaxation time (T_1) and increase ^{19}F detection sensitivity by several folds. Our lab recently developed two distinct fluorous-soluble metal chelate formulations. The first one, referred to as FETRIS, (metallated with ferric tris-diketonate) enabled three-to fivefold sensitivity

enhancement compared to non metallated equivalent[12]. The second metallated nanoemulsion, featuring salicylidene-tris(aminomethyl)ethane chelating agent (SALTAME), achieved a sensitivity enhancement of four-fold on a 3 Tesla magnet.

Moreover, pulse programming offers great opportunity to improve the signal to noise ratio per acquisition time. Techniques such as compressed sensing, involving both acquisition modification and more efficient hardware, have been investigated for the past decade, yielding accelerated scan times up to 8 folds[14]. Development of smarter quantitation algorithms could also reduce post-processing burden. Combination of the three strategies described above; cell penetrating peptides, metal chelates and compressed sensing sequences may improve the sensitivity limits of ^{19}F MRI by an order of magnitude and enable detection of sparse cells *in vivo*.

Another avenue that is heavily investigated is the development of PFCs with different chemical shifts to potentially generate multicolor fluorine MRI images by tagging different cell subtypes. This would allow to visualize different cell therapy interactions and migration *in vivo*. Such application has already been demonstrated for stem cell/progenitor cell tracking *in vivo* [15]. One could imagine labeling macrophages or dendritic cells *in situ* by intravenous injection of a given PFC and transferring CAR T cells or TILs labeled *ex vivo* with a different PFC to visualize their interaction in the lymph nodes or their biodistribution to the tumor. This would enable further understanding of different meeting points and partner interactions and migration patterns *in vivo*.

Finally, an exciting development of ^{19}F MRI would be targeted *in vivo* labeling of cell populations of interest. Numerous PET tracers and a few SPIOs have been investigated to target specific cells or proteins. Only a couple targeted fluorine nanoemulsions have been

developed so far, likely due to the technical challenge it represents. Specific *in vivo* labeling would require specific blood circulation time, relative 'invisibility' towards monocytes and macrophages to avoid non-specific signals and sufficient targeting efficiency to visualize positive signal on MR images. Nonetheless, some effort is being spent on theranostic fluorine emulsions, to enable both imaging of the recipient cells and delivery of specific drugs[16, 17].

6.5. Clinical translation

^{19}F MRI cell detection techniques are just beginning to be employed in clinical trials, and feasibility has been established in a first-in-human clinical study[3]. An autologous DC vaccine was labeled with a PFC nanoemulsion *ex vivo* and re-injected into colorectal cancer patients intradermally. ^{19}F MRI enabled visualization of injected DCs and longitudinal persistence evaluation.

There are numerous checkpoints before one can use ^{19}F MRI cell tracking for cell therapies in the clinic. When engaging cell therapy regulatory agencies, such as the US Food and Drug Administration (FDA), safety is the primary concern. Within the FDA, ^{19}F labeled combination cell products are regulated at the Center for Biologics Evaluation of Biologics Research (CBER). Usage of a nonradioactive PFC, like ^{19}F, is appealing due to its safety profile and presence in several FDA-approved medicines[18], as well as their approved use for contrast-enhanced ultrasound. For cellular therapies, the release criteria for PFC labeled cell batches, which is viewed as a combination product, should match the release criteria

expected for the unlabeled cell product[3], such as total nucleated cell count, cell viability, Gram stain, bacterial contamination and endotoxin quantification.

Post infusion, cell viability and anti-tumor efficacy of PFC labeled cells may also be examined in preclinical studies as part of the investigational new drug (IND) application for the cell therapy product. However, imaging results in rodent models of cellular immunotherapy can have significant limitations and may not well reflect how the cell product will behave in patients. Besides the obvious immunological dissimilarities, particularly with immunodeficient xenograft models, typical total cell number doses infused in ACT trials are vastly higher in human trials compared to mice ($\sim 10^{10}$ versus 10^6, respectively). Dosing on a cell number/kg basis can help predict translation to clinical dosing. However, because tumor size may be of similar order of magnitude in size in rodent and humans, scaling the absolute number of therapeutic cells homing to patients' tumors may be difficult to predict.

As experience with PFC labeling of cell therapy products grows, additional considerations may also be needed, for example, in the clinical batch scale-up of the labeling process[19] in specialized facilities. Furthermore, one could imagine having a cell therapy product expanded at a third-party site with a PFC label incorporated, and then shipped as a refrigerated or cryopreserved pre-labeled cell product; similar workflows are already in place for unlabeled, FDA-approved DC and CAR T cell products for cancer patients. Routine labeling of large cell batches can be engineered into a well-controlled process that can be exportable to multi-site clinical trials. Additional logistical limitations to the development of routine fluorine imaging include the fact that clinical scanners are most often equipped for proton scans only. ^{19}F MRI requires specialized detection coils and hardware

modifications for image acquisition, which are not currently available in most MRI centers, but can be sourced by third parties.

In conclusion, cell labeling with perfluorocarbons is a well-controlled and validated process that has been reproduced by numerous laboratories. The properties of labeled cells, such as labeling levels and intracellular localization of PFC, are predictable based on intrinsic phagocytic tendencies, physical cell size, high-level function in the body, and cell activation status and health during the labeling process. Fluorine MRI enables noninvasive monitoring of *in vivo* survival and behavior of therapeutic cells, as well as their indirect effect on cancer cells. Overall, the use of ^{19}F-based MRI cell detection of cell therapy products *in vivo* is still in the early adaptor phase, but holds promise for overcoming regulatory barriers and advancing a wide range of cell therapy trials for cancer.

Acknowledgments

Chapter 6, in part contains text as it appears in a manuscript published in JITC entitled "Fluorine-19 MRI for detection and quantification of immune cell therapy for cancer" Chapelin F, Capitini C, Ahrens E.T. The dissertation author was the primary investigator and author of this paper.

References

1. Chapelin, F., Gao, S., Okada, H., Weber, T.G., Messer, K. & Ahrens, E.T. Fluorine-19 nuclear magnetic resonance of chimeric antigen receptor T cell biodistribution in murine cancer model. *Scientific Reports* **7** (2017).

2. Ribot, E.J., Gaudet, J.M., Chen, Y., Gilbert, K.M. & Foster, P.J. In vivo MR detection of fluorine-labeled human MSC using the bSSFP sequence. *International journal of nanomedicine* **9**, 1731-1739 (2014).

3. Ahrens, E.T., Helfer, B.M., O'Hanlon, C.F. & Schirda, C. Clinical cell therapy imaging using a perfluorocarbon tracer and fluorine-19 MRI. *Magnetic resonance in medicine* **72**, 1696-1701 (2014).

4. Khurana, A., Chapelin, F., Beck, G., Lenkov, O.D., Donig, J., Nejadnik, H., Messing, S., Derugin, N., Chan, R.C., Gaur, A., Sennino, B., McDonald, D.M., Kempen, P.J., Tikhomirov, G.A., Rao, J. & Daldrup-Link, H.E. Iron administration before stem cell harvest enables MR imaging tracking after transplantation. *Radiology* **269**, 186-197 (2013).

5. Makela, A.V., Gaudet, J.M. & Foster, P.J. Quantifying tumor associated macrophages in breast cancer: a comparison of iron and fluorine-based MRI cell tracking. *Sci Rep* **7**, 42109 (2017).

6. Castro, O., Nesbitt, A.E. & Lyles, D. Effect of a perfluorocarbon emulsion (Fluosol-DA) on reticuloendothelial system clearance function. *American journal of hematology* **16**, 15-21 (1984).

7. Ahrens, E.T. & Bulte, J.W. Tracking immune cells in vivo using magnetic resonance imaging. *Nature reviews. Immunology* **13**, 755-763 (2013).

8. Fink, C., Gaudet, J.M., Fox, M.S., Bhatt, S., Viswanathan, S., Smith, M., Chin, J., Foster, P.J. & Dekaban, G.A. (19)F-perfluorocarbon-labeled human peripheral blood mononuclear cells can be detected in vivo using clinical MRI parameters in a therapeutic cell setting. *Sci Rep* **8**, 590 (2018).

9. Srinivas, M., Boehm-Sturm, P., Figdor, C.G., de Vries, I.J. & Hoehn, M. Labeling cells for in vivo tracking using (19)F MRI. *Biomaterials* **33**, 8830-8840 (2012).

10. Stares, E., Rho, J., Ahrens, E.T., Foster, P., Li, A. & Bartha, R. in Contrast Agents for MRI: Experimental Methods 479-498 (The Royal Society of Chemistry, 2018).

11. Zhong, J., Mills, P.H., Hitchens, T.K. & Ahrens, E.T. Accelerated fluorine-19 MRI cell tracking using compressed sensing. *Magnetic resonance in medicine* **69**, 1683-1690 (2013).

12. Kislukhin, A.A., Xu, H., Adams, S.R., Narsinh, K.H., Tsien, R.Y. & Ahrens, E.T. Paramagnetic fluorinated nanoemulsions for sensitive cellular fluorine-19 magnetic resonance imaging. *Nature materials* **15**, 662-668 (2016).

13. Guidotti, G., Brambilla, L. & Rossi, D. Cell-Penetrating Peptides: From Basic Research to Clinics. *Trends Pharmacol Sci* **38**, 406-424 (2017).

14. Lustig, M., Donoho, D.L., Santos, J.M. & Pauly, J.M. Compressed sensing MRI. *Ieee Signal Proc Mag* **25**, 72-82 (2008).

15. Partlow, K.C., Chen, J., Brant, J.A., Neubauer, A.M., Meyerrose, T.E., Creer, M.H., Nolta, J.A., Caruthers, S.D., Lanza, G.M. & Wickline, S.A. 19F magnetic resonance imaging for stem/progenitor cell tracking with multiple unique perfluorocarbon nanobeacons. *FASEB journal : official publication of the Federation of American Societies for Experimental Biology* **21**, 1647-1654 (2007).

16. Liu, L., Bagia, C. & Janjic, J.M. The First Scale-Up Production of Theranostic Nanoemulsions. *Biores Open Access* **4**, 218-228 (2015).

17. Patel, S.K., Beaino, W., Anderson, C.J. & Janjic, J.M. Theranostic nanoemulsions for macrophage COX-2 inhibition in a murine inflammation model. *Clin Immunol* **160**, 59-70 (2015).

18. Ruiz-Cabello, J., Barnett, B.P., Bottomley, P.A. & Bulte, J.W.M. Fluorine (F-19) MRS and MRI in biomedicine. *Nmr in Biomedicine* **24**, 114-129 (2011).

19. O'Hanlon, C.F., Fedczyna, T., Eaker, S., Shingleton, W.D. & Helfer, B.M. Integrating a 19F MRI Tracer Agent into the Clinical Scale Manufacturing of a T-Cell Immunotherapy. *Contrast Media & Molecular Imaging* (2017).